

AUTOMATIC FORENSIC IDENTIFICATION BASED ON
DENTAL RADIOGRAPHS

By

Hong Chen

A DISSERTATION

Submitted to
Michigan State University
in partial fulfillment of the requirements
for the degree of

DOCTOR OF PHILOSOPHY

Department of Computer Science and Engineering

2007

ABSTRACT

AUTOMATIC FORENSIC IDENTIFICATION BASED ON DENTAL RADIOGRAPHS

By

Hong Chen

The purpose of forensic identification is to determine the identity of unidentified victims. Dental radiographs are often the only means of identifying victims, but manually comparing dental radiographs is inefficient and subject to errors due to fatigue in human experts. This thesis has designed and developed an automatic system for identifying human victims based on dental radiographs. There are three stages in the proposed automatic dental identification system:

1. Feature extraction. Salient features in the dental radiograph are identified, such as the contours of the tooth and the contours of crowns or fillings.
2. Registration. Each tooth is labeled according to its location within the mouth, and missing teeth are detected.
3. Matching. Each unidentified radiograph (post-mortem or PM) is compared to a database of known individuals (ante-mortem or AM).

In the first stage, namely feature extraction, contours of teeth and dental work are extracted from dental radiographs. The radiographs are first segmented into regions such that each region contains only a single tooth. Contours of individual teeth are then extracted from each region of the radiograph using active shape models (ASMs). Dental work such as crowns, fillings, and root canal treatment is composed of radio-opaque material that appears as bright regions in the radiographs. An anisotropic diffusion-based technique is used to enhance the images, and regions of dental work are segmented using image thresholding.

The second step in dental radiograph-based identification is to determine which teeth are (or are not) present in the radiograph. This step is important because the matching

algorithm cannot properly align AM and PM radiographs if they do not contain the same number of teeth. Thus, the second step is to label each tooth in the radiograph based on the human dental atlas, which is a descriptive model of the shapes and relative positions of teeth. A hybrid model involving Support Vector Machines (SVMs) and a Hidden Markov Model (HMM) is developed for representing the dental atlas and classifying individual teeth in dental radiograph images.

The final stage of the proposed automatic identification system is to match dental radiographs of unidentified subjects against dental radiographs of known subjects in the database. The extracted tooth contours are matched for every pair of teeth with the same index in the two radiographs. When both teeth in the pair to be matched contain dental work, then the shapes of dental work are also matched. An overall matching distance for each pair of teeth is computed by combining the matching distances for the tooth contours and for the dental work. Finally, the distances between the unidentified subject and all the subjects in the database are computed based on the distances between all pairs of teeth. The database subjects are then sorted in ascending order of the matching distances and the results are provided to forensic experts.

Due to poor quality of dental radiographs and complexity of the matching problem, fully automatic methods may sometimes produce errors. Monitoring schemes are designed to evaluate the image quality and correctness of the automatic results at each processing stage. User interaction is requested when errors in intermediate processing steps are encountered.

Experiments on retrieving PM radiographs of 29 subjects from a database of radiographs of 33 subjects show an accuracy of 72% for top-1 retrieval and 93% for top-2 retrievals. Experiments on retrieving PM radiographs of 29 subjects from a larger database of relatively poor quality radiographs of 133 subjects show a lower accuracy of 66% for top-1 retrieval and 90% for top-13 retrievals.

To my grandparents and parents

ACKNOWLEDGMENTS

I am grateful to all the people who have helped me during the past 4 years at Michigan State University. First of all, I would like to express my gratitude to my advisor, Dr. Anil K. Jain, for his guidance and support. His devotion to his career, preference for perfection, and relentless chase of novelty have inspired a great deal of my thinking on how to be a professional researcher. I am grateful to my Ph.D. committee, Dr. Joyce Chai, Dr. Sarat C. Dass, and Dr. John J. Weng for their suggestions, comments, and encouragement. I am also grateful to Dr. George C. Stockman for his support and guidance.

I would especially like to thank Dr. Rong Jin for his guidance, which led me into the fantastic world of machine learning and numerical optimization techniques.

I would like to thank all the members in the PRIP lab in the Department of Computer Science and Engineering at MSU for their generous help and inquisitive discussions (in alphabetical order): Yi Chen, Dirk Colbry, Meltem Demirkus, Michael Farmer, Miguel Figueroa-Villanue, Steve Krawczyk, Martin Law, Xiaoguang Lu, Pavan K. Mallapragada, Anoop Namboodiri, Karthik Nandakumar, Unsang Park, Arun A. Ross, Umut Uludag, and YongFang Zhu.

I would like to thank all visiting scholars to the PRIP lab for their guidance, discussion, and friendship, especially Dr. Yunhong Wang, Dr. Francesc J. Ferri, Dr. Aparecido N. Marana, and Dr. Choonwoo Ryu.

Thanks are also due to Adam Pitcher, Starr Portice, Norma Teague, Linda L. Moore, Cathy M. Davison, and Debbie Kruch for their assistance and help. I would also like to thank Kim G. Thompson and Dr. Katy L. Colbry for their help in proofreading my thesis.

I want to express my gratitude to the National Science Foundation (NSF) for supporting this research. I would like to thank Dr. Hany H. Ammar, Dr. Gamal Fahmy, Dr. Mohamed Abdel-Mottaleb and Dr. Robert Howell for providing image data so that the experiments for my research could be conducted.

Finally, and most importantly, I would like to thank my family for their unconditional love and support.

TABLE OF CONTENTS

LIST OF TABLES	ix
LIST OF FIGURES	x
1 Automatic Forensic Identification	1
1.1 Automatic Identification of Humans	1
1.2 Forensic Identification	3
1.3 Procedure of Comparative Dental Identification	4
1.4 Identification of Humans Using Dental Radiographs	7
1.4.1 Introduction to Dental Radiographs.....	7
1.4.2 Dental Radiographs for Identification	9
1.5 Automatic Dental Identification	13
1.5.1 Available Software for Matching Dental Records to Forensic Evidence	13
1.5.2 Dental Radiograph-based Automatic Identification System.....	15
1.5.3 Challenges.....	17
1.6 Summary	22
2 Segmentation and Contour Extraction	24
2.1 Automatic Image Quality Evaluation	25
2.1.1 Detection of Panoramic Images	25
2.1.2 Detection of Intensity Imbalance	26
2.1.3 Blur Detection.....	27
2.2 Radiograph Segmentation.....	27
2.2.1 Automatic Segmentation.....	28
2.2.2 User Interaction.....	33
2.3 Extracting Tooth Contours.....	37
2.3.1 Introduction to Active Shape Models	37
2.3.2 ASM-Based Tooth Contour Extraction	39
2.3.3 Experiments	50
2.4 Segmenting Regions of Dental Work	51
2.4.1 Image Thresholding	53
2.5 Summary	54
3 Registration of Radiographs to Dental Atlas	57
3.1 Introduction.....	58
3.2 SVM / HMM Hybrid Model	59
3.3 Registering a Tooth Sequence to Dental Atlas	62
3.3.1 Representation of Dental Atlas	63
3.3.2 Extraction of Observation Sequences	64
3.4 User Interaction.....	65
3.5 Experimental Results	65
3.6 Summary	67

4	Matching and Retrieval	72
4.1	Radiograph Matching.....	72
4.1.1	Introduction to Shape Matching.....	73
4.1.2	Matching Tooth Contours.....	75
4.1.3	Matching Dental Work Contours.....	80
4.1.4	Fusing the Matching Distances.....	82
4.2	Matching Subjects.....	85
4.3	Experimental Results.....	87
4.4	Summary.....	93
5	Conclusions and Future Directions	108
5.1	Feature Extraction.....	108
5.2	Atlas Registration.....	110
5.3	Matching.....	110
5.4	Future Directions.....	111
	APPENDICES	113
	A Database Description	113
	B Anisotropic Diffusion	115
	BIBLIOGRAPHY	117

LIST OF TABLES

1.1 A Comparison of Evidence Types Used in Victim Identification	4
1.2 A Comparison of WinID and Odonto Search	15
2.1 Results of Automatic Radiograph Segmentation	33
2.2 Success Rate of Automatic Contour Extraction.....	51
2.3 Summary of CPU (2.99 GHz Pentium 4) Time for Extracting Features	56
3.1 Accuracies and Sources of Error in Estimating Tooth Indices	67
4.1 CPU (2.99 GHz Pentium 4) Time for Matching one PM Query Image Set to one AM Database Image Set	103
A.1 List of Types, Numbers and Sources of Images In the Database	114

LIST OF FIGURES

1.1 An example of postmortem dental chart [51].	5
1.2 Three types of dental radiographs. (a) A bitewing radiograph; (b) a periapical radiograph; (c) a panoramic radiograph.	8
1.3 Three types of dental radiograph series. (a) Full mouth series; (b) bitewing series; (c) panoramic series.	10
1.4 A forensic expert examines a dental radiograph film of a tsunami victim in Phuket, Thailand, on Jan. 11, 2005 [3].	12
1.5 Dental radiographs and the corresponding description chart used by WinID system. The crosses indicate the missing teeth, and the filled squares indicate locations of the dental restorations in each tooth.	14
1.6 System diagram of automatic dental identification system.	16
1.7 Fully automatic process of matching one pair of PM and AM images from the same subject.	18
1.8 Automatic matching of one pair of PM and AM images with user interaction.	19
1.9 Antemortem (a) and postmortem (b) radiographs of a difficult identification case for an automatic matching system. The poor image quality poses difficulties for contour extraction. The orthodontics operation in (a) and missing teeth in (b) have significantly altered the dentition appearance over time.	21
1.10 Changes in the imaging angle result in significant deformations in the appearances of corresponding teeth in (a) AM and (b) PM periapical radiograph images.	22
1.11 Some images in the dental radiograph database.	23
2.1 Detection of intensity imbalance. (a) An over-exposed image; (b) an underexposed image; (c) an non-homogeneously exposed image with STDMI= 30.	26
2.2 Detection of blur. (a) A sharp image with MAD = 2.35; (b) A blurred image with MAD = 1.08.	27
2.3 A dental radiograph of a child showing both permanent teeth and primary teeth.	28
2.4 Classification of image types based on number of rows of teeth. (a) and (d) images with two rows of teeth; (b) and (e) images with only lower row of teeth; (c) and (f) images with only upper row of teeth.	30

2.5 Finding knots in the segmentation line.	31
2.6 Some examples of correct segmentation.	32
2.7 Some results of incorrect automatic segmentation. (a) and (b) incorrect location of segmentation line between upper and lower rows of teeth; (c) under segmentation; (d) over segmentation; (e) improper segmentation.	34
2.8 User interaction for correcting of the first type of error: incorrect location of segmentation line between upper and lower rows of teeth. (b) Correction of the incorrect segmentation line between upper and lower teeth in (a) by specifying one point (shown as cross).	35
2.9 User interaction for correcting of the second type of error: under segmentation. (b) Adding an isolation line in (a) by specifying one point (shown as cross).	35
2.10 User interaction for correction of the third type of error: over segmentation. (b) Removing an extra isolation line in (a) by specifying one point (shown as cross).	36
2.11 User interaction for correction of the fourth type of error: improper segmentation. (b) Correction of an improper segmentation by removing the improper segmentation line in (a) by specifying one point (shown as cross in (a)) and adding correct segmentation lines by specifying two points (shown as cross in (b)).	36
2.12 Region of Interest (ROI) for a tooth.	37
2.13 Shape Alignment. (a) correspondence between a prototype shape and a training shape; (b) correspondence between the prototype shape and the rotated training shape; (c) correspondence between the prototype shape and the scaled training shape.	41
2.14 First five modes of the shape model of teeth. The middle shape in each row is the mean shape, while the other four shapes are, from left to right, mean shape plus four eigenvectors multiplied by -2, -1, 1, and 2 times the square root of the corresponding eigenvalues.	43
2.15 Shape extraction procedure.	44
2.16 Initialization of tooth shapes.	46
2.17 Crown nodes and root nodes in the model.	49
2.18 Detection of erroneous tooth contours.	50
2.19 Tooth shapes successfully extracted using ASMs.	52

2.20 Fitting a mixture of Gaussians model to the intensity histogram (b) of an image (a), in which the dental work appears as a bright block.	54
2.21 Extracted dental work contours with and without image enhancement. (a), (b) and (c) Without enhancement. (d), (e) and (f) After enhancement.	55
2.22 Process of extracting tooth contours and dental work contours with human interaction. Automatic method works well for the good quality image (image 1), but needs user interaction for poor quality image (image 2).	56
3.1 Three types of teeth. (a) Molar; (b) (bi)cuspid; (c) incisor.	59
3.2 Dental Atlas of a complete set of adult teeth containing indices and classification labels of the teeth.	64
3.3 SVM/HMM model for the upper row of 16 teeth.	65
3.4 Extraction of tooth contours and generation of an observation sequence, $E = \{e_1, e_2, e_3, e_4, e_5\}$; e_1, e_3 and e_5 correspond to tooth states, and e_2 and e_4 correspond to distance states.	69
3.5 A user interface for manually specifying tooth indices by clicking the corresponding teeth in the dental atlas, which is shown on the right side of the dental radiograph.	70
3.6 Examples of successful registration of the dental atlas to (a) a bitewing image, (b) a periapical image, and (c) an image with a missing tooth. In (c), teeth numbered as 12, 14, and 15 are correctly registered. The missing tooth (number 13) is detected.	70
3.7 Examples of atlas registration errors. (a) The tooth types are correctly classified as molars, but the teeth (with genuine indices 30 and 31) are registered to teeth 31 and 32 in the atlas since teeth 30, 31, and 32 are all molars and the length of the sequence is insufficient for resolving the ambiguity; (b) all the three incisors are classified as (bi)cuspid, thus these teeth (with genuine indices 8, 9, and 10) are registered to teeth 3, 4, and 5 in the atlas; (c) the distance between teeth 3 and 6 seems to support only one missing tooth, so the input sequence is registered to the atlas teeth numbered 1, 2, 3, 5, 6, 7, 8, 9, 10, 12, 13, and 14, while the genuine indices are 1, 2, 3, 6, 7, 8, 9, 10, 11, 13, 14, and 15. The lower row of teeth is, however, correctly registered to the atlas.	71
4.1 Classification of shape matching methods [65].	74
4.2 Polygonal approximation of a tooth contour with different interval arc lengths. (a) Original tooth contour; (b) polygonal approximation of (a) with interval arc length $l = 5$ pixels; (c) polygonal approximation of (a) with interval arc length $l = 10$ pixels; (d) polygonal approximation of (a) with interval arc length $l = 20$ pixels; (e) polygonal approximation of (a) with interval arc length $l = 30$ pixels.	77

4.3 Dental radiographs are 2D projections of 3D structures.	78
4.4 Shape registration process. (a) Continuous tooth contours; (b) discrete tooth contours; (c) initialization by aligning bounding boxes; (d) initialized point correspondence; (e) aligned contours after optimum transformation; (f) correspondence after alignment and outlier detection.	81
4.5 Dental work merging due to a change in the imaging angle. The hole in the circled dental work seen in image (a) is occluded when viewed from the angle shown in (b) even though both the images are of the same tooth; (c) preprocessed image for two teeth in image (a); (d) preprocessed image for two teeth in image (b); (e) result of ‘Exclusive-Or’ operation for the two teeth. Pixels of value ‘1’ are displayed in black, and the pixels of value ‘0’ are displayed in gray.	83
4.6 Distribution of matching distances based on the shape of dental work.	84
4.7 Coupling 4 pairs of neighboring teeth with 6 pairs of neighboring teeth. The matching score between each pair of neighboring teeth is calculated and the average is taken along the arrows. The results are listed in the bottom bar of black and white cells, and the minimum of these values is defined as the matching distance between the two sequences.	87
4.8 Two examples of tooth correspondence. Tooth contours in (a) and (b) are paired up in (c); tooth contours in (d) and (e) are paired up in (f).	88
4.9 Some AMimages (a) and PMimages (b) of a single individual in the database.	89
4.10 Examples of matching. The gray lines represent the tooth shapes in the database and the query images; the black lines represent the query shapes after transformation. Note that in these examples, the matching distance for the genuine AM images is smaller than the matching distance for the imposter AM images.	91
4.11 The top-4 retrievals for 3 different queries. The first image in each column is the query image and the remaining four images are the top-4 retrievals. The genuine AM images are ranked first for these three queries.	92
4.12 Cumulative matching characteristics (CMC) curves for subject retrieval in the database of 33 subjects.	94
4.13 Cumulative matching characteristics (CMC) curves for subject retrieval in the database of 133 subjects.	95
4.14 Subject 10 was not tested for retrieval due to poor image quality. (a) AM radiograph; (b) PM radiographs.	96

4.15 Subject 14 was not tested for retrieval due to eruption of new teeth in AM radiographs. (a) AM radiographs; (b) PM radiographs.	97
4.16 Subject 21 was not tested for retrieval due to eruption of new teeth in AM radiographs. (a) AM radiographs; (b) PM radiographs.	98
4.17 Subject 36 was not tested for retrieval due to poor image quality. (a) AM radiograph; (b) PM radiographs.	99
4.18 Subject 1 was not correctly retrieved from the database due to changes in the dentition caused by loss of teeth. (a) AMradiographs; (b) PMradiographs.	100
4.19 Subject 2 was not correctly retrieved from the database due to incorrect AM tooth contour extraction from the only available panoramic image. (a) AM radiograph; (b) PM radiographs.	101
4.20 Subject 9 was not correctly retrieved from the database due to incorrect AM tooth contour extraction caused by overlapping upper and lower rows of teeth. (a) AM radiographs; (b) PM radiographs.	102
4.21 Subject 16 was not correctly retrieved from the database due to changes in tooth appearances in AM and PM radiographs. (a) AM radiograph; (b) PM radiograph.	103
4.22 Subject 25 was not correctly retrieved from the database due to incorrect AM tooth contour extraction from the panoramic image and the bitewing images where upper and lower rows of teeth overlap. (a) AM radiographs; (b) PM radiographs.	104
4.23 Subject 28 was not correctly retrieved from the database due to incorrect AM tooth contour extraction from the only available panoramic image. (a) AM radiograph; (b) PM radiographs.	105
4.24 Subject 39 was not correctly retrieved from the database due to insufficient number of teeth in the AM image. (a) AM radiograph; (b) PM radiographs.	106
4.25 Subject 42 was not correctly retrieved from the database due to incorrect AM tooth contour extraction from the only available panoramic image. (a) AM radiograph; (b) PM radiographs.	107
5.1 A dental X-ray shows loss of jaw bones caused by periodontal disease.	111

CHAPTER 1

Automatic Forensic Identification

The purpose of forensic identification is to determine the identities of unidentified suspects or victims. The significance of research on automatic methods for forensic identification has been brought to public attention by recent disasters, such as the 9/11 terrorist attack and the 2004 Asian tsunami.

This chapter begins with a brief survey of the methods for automatic human identification, and introduces the dental radiograph-based approach for forensic identification. We also discuss some challenges to automatic identification based on dental records, and briefly introduce the proposed automatic system for identifying humans based on dental radiographs.

1.1 Automatic Identification of Humans

The evidence used for human identification is categorized into three classes: *what you have*, *what you know*, and *what you are* [39]. The first category, *what you have*, includes credit cards, identification documents, etc. *What you know* refers to all kinds of passwords and confidential information, e.g., mother's maiden name. *What you are* includes your anatomical features, also called biometrics, such as your face, DNA, iris, fingerprints, etc. With the growing need for reliable and robust human identification in a variety of applications

(e.g., international border crossing), biometric-based recognition has become an important topic for research in computer vision and pattern recognition.

Biometric features can be categorized into two types: *physical* and *behavioral* [39]. Physical biometric features represent the anatomical makeup of the human body, such as the fingerprint, face, iris, retina scan, ear shape, hand geometry, hand vein, etc. Behavioral biometric features reflect the behavioral traits of an individual, such as voice, gait, signature, key stroke dynamics, etc.

Biometric features are evaluated in terms of *universality*, *uniqueness*, *permanence*, *collectability*, and *acceptability* [39]. Universality means the degree to which a biometric feature is commonly possessed. For instance, faces have a higher universality than key stroke dynamics, since much of the population does not use a keyboard regularly. Uniqueness measures how a biometric feature varies across the population. For instance, the iris has a higher uniqueness than hand geometry. While uniqueness measures the inter-user variability, permanence measures the intra-user variability. Generally, physical biometric features are more permanent than behavioral biometric features, since behavioral biometric features are affected by a person's mental status and environmental factors. Collectability measures how easily a feature can be measured quantitatively. Physical biometric features are usually easier to measure quantitatively than behavioral biometric features. However, some physical biometric features, such as hand vein pattern and retina scans, generally have lower acceptability, because they may reveal a person's health status and this may be regarded as an invasion of privacy.

Biometric technologies are evaluated in terms of their performance and vulnerability to circumvention. Technologies using more unique and permanent biometric features usually have higher performance. Some biometric technologies are more vulnerable to fraud than others. For example, 2D face recognition technologies are easier to spoof than 3D face recognition technologies. Research on anti-spoofing technologies is addressing this issue [44] [53] [24] [21].

1.2 Forensic Identification

There are two main purposes for forensic identification of humans: *suspect identification* and *victim identification*. For suspect identification, evidence such as fingerprints, bite marks, and blood samples are collected at crime scenes. Based on this evidence, the guilt or innocence of the suspects can be confirmed. The goal of victim identification is to determine the identity of victims based on characteristics of the human remains. Based on the number of victims involved, victim identification is categorized into two types: *individual victim identification* and *disaster victim identification*. There is an urgent demand for an automatic disaster victim identification system due to the recent occurrences of massive disasters.

Victim identification can be achieved by matching antemortem (AM) and postmortem (PM) *circumstantial* evidence and *physical* evidence [2]. The circumstantial evidence includes a victim's clothing, jewelry, and pocket contents. If the antemortem description of the same circumstantial evidence can be provided, it may assist in the victim's correct identification. However, circumstantial evidence can easily be attributed to the wrong person, particularly when there are many disaster victims to be identified. Physical evidence is more reliable, and includes *external evidence*, *internal evidence*, *dental evidence*, and *genetic evidence* [2]. External evidence includes gender, estimated age, height, build, color of skin, etc. Specific features, such as scars, moles, tattoos, and abnormalities, are especially useful if they can be matched with antemortem records, and fingerprints are valuable external evidences as well. Internal examination (autopsy) is often necessary for determining the cause of death. An autopsy may also find medical evidence that can assist in identification, such as previous fractures or surgery, missing organs (e.g., appendix, kidney), or implants. Dental evidence (such as fillings or missing teeth) is particularly important, since it can offer sufficient information to positively identify a victim without the need for additional information. The use of dental evidence for human identification is discussed in the next section. Genetic identification involves comparing DNA samples from an indi-

vidual with antemortem DNA, or with DNA samples from the suspected victim’s ancestors or descendants. Genetic identification is especially useful when the bodies of the victims are severely mutilated. Table 1.1 compares the various methods of identifying victims in terms of *accuracy*, *time needed for identification*, *antemortem record availability* (the possibility of obtaining antemortem evidence), *robustness to decomposition (of the body)* and *instrument requirement* (number of instruments needed for matching).

Table 1.1. A Comparison of Evidence Types Used in Victim Identification

Evidence type	Circumstantial	Physical			
		External	Internal	Dental	Genetic
Accuracy	Med.	High	Low	High	High
Time for Identification	Short	Short	Long	Short	Long
Antemortem Record Availability	High	Med.	Low	Med.	High
Robustness to Decomposition	Med.	Low	Low	High	Med.
Instrument Requirement	Low	Med.	High	Med.	High

1.3 Procedure of Comparative Dental Identification

Typically, unidentified human remains are reported to the law enforcement agencies who then initiate a request for dental identification. Often a presumptive or tentative identification is available (e.g., wallet or driving licence found on the body) and this will enable antemortem records to be located. In other instances, using data from the missing persons’ database, the location where the body is found or other physical characteristics and circumstantial evidence may enable a putative identification to be made. Antemortem records are then obtained from the dentist of the suspected missing persons.

The forensic dentist produces the postmortem record by careful charting and writing descriptions of the dental structures and radiographs. An example of dental chart is shown in Figure 1.1. If the antemortem records are available at this time, postmortem radiographs should be imaged to replicate the type and angle of the antemortem records [33]. Radiographs should be marked with a rubber-dam punch to indicate antemortem and postmortem to prevent confusion - one hole for antemortem films and two holes for postmortem

films [1].

B.C. CORONERS' SERVICE
DENTAL IDENTIFICATION FORM



CORONER CASE No. 98-129-0008 DATE: 09 December 1998
 INVESTIGATING CORONER S. Pallavin EXAMINATION SITE Vancouver City Waiver
 LOCATION Port Moody
 CORONERS FORENSIC UNIT CASE # 98-123
 POLICE FILE No. 98-2317 AUTOPSY No. _____
 POLICE AGENCY RMP Port Moody HOSPITAL _____
 POLICE INVESTIGATOR Cst. H. Gillman PATHOLOGIST _____

CIRCUMSTANCES OF EXAMINATION Skeletal remains found on Nov 09, 98 in the gut of Royal Grist, Port Moody, B.C. Taxialite I.D. ... - D.O.B. 01 Aug 19

	A,21	A	A,20	Px	Px	Px	B22	Px	Px	X							
UPPER RIGHT																	
	18	17	16	15	14	13	12	11	31	32	33	34	35	36	37	38	
LOWER RIGHT																	
	48	47	46	45	44	43	42	41	31	32	33	34	35	36	37	38	
	A,5,5	A,5,5	Px	Px	Px	Px	Px	Px	Px	Px	Px	Px	Px	A,5,5		X	

CODE: Shade all restorations on Chart. Outline Prosthetic Appliances. Circle the appropriate descriptions

Fellow Code:	TC. Temporary Crown	EN. Root Treatment	X. Missing
A. Amalgam	GC. Gold Crown	BR. Bridge Work	PX. Posthumously missing
S. Composite	PC. Porcelain Crown	(Bracket & shade)	NR. Not Recovered
G. Gold	PFM. Porcelain / Metal Crown	PP. Partial Denture	
SE. Resin Sealant	SC. Stainless Steel Crown	(Bracket & describe)	
TF. Temporary Filling			

1. Mottled Enamel	8. Erosion	15. Retained Deciduous Teeth	22. Congenitally Absent
2. Enamel Hypoplasia	9. Fractured Enamel	16. Unusual Restorations	23. Extorted roots maxilla
3. Discoloration	10. Rotation	17. Unusual Appliances	24. Buccal restoration compesi
4. Staining	11. Malpositioned Teeth	18. Cyst Formation	
5. Calculus	12. Malocclusion	19. Post	
6. Abrasion	13. Unerupted Teeth	20. Pin	
7. Aisition	14. Supernumerary Teeth	21. Caries	25. _____

Post mortem dental x-ray: Yes/No _____
 Photos: Yes/No _____
 Study Models: Yes/No _____
 Jaws disarticulated: Yes/No _____

Occlusion: Unrecoverable

Remarks: Granular deposits gross, most highmouth uniget, likely to have "peg-shaped" #22. Extorted maxilla #1

Figure 1.1. An example of postmortem dental chart [51].

Once the postmortem record is complete, a comparison between the two records can be carried out. A methodical and systematic comparison is required to examine each tooth and surrounding structures. While dental restorations play a significant role in the identification process, many other oral features such as pathological and morphological characteristics are assessed. Such additional features play an increasingly important role in those individuals with minimal restorations. Because of the progressive decrease in dental cavities, so-called non-restorative cases are likely to become more common [46].

Similarities and discrepancies should be noted during the comparison process [55].

There are two types of discrepancy, those that can be explained and those that cannot. Explainable discrepancies normally relate to the time elapsed between the antemortem and postmortem records. Examples include teeth extracted or restorations placed or enlarged. If a discrepancy is unexplainable, for example a tooth is not present in the antemortem record but is present in the postmortem record then an exclusion must be made.

A range of conclusions can be reached when reporting a dental identification. The American Board of Forensic Odontology recommends that these be limited to the following four conclusions [1]:

- Positive identification: The antemortem and postmortem data match in sufficient detail, with no unexplainable discrepancies, to establish that they are from the same individual.
- Possible identification: the antemortem and postmortem data have consistent features but, because of the quality of either the postmortem remains or the antemortem evidence, it is not possible to establish identity positively.
- Insufficient evidence: The available information is insufficient to form the basis for a conclusion.
- Exclusion: the antemortem and postmortem data are clearly inconsistent.

It is important to note that there is no minimum number of concordant points or features that are required for a positive identification. In many cases a single tooth can be used for identification if it contains sufficiently unique features. On the other hand, a full-mouth series of radiographs may not reveal sufficient detail to render a positive conclusion [1]. The discretion of identification lies with the odontologist who must be prepared to justify the conclusions in court [51].

1.4 Identification of Humans Using Dental Radiographs

Dental radiographs are one of the most valuable pieces of evidence for disaster victim identification. This section begins with an overview of dental radiographs (also known as dental X-rays) and then describes how dental radiographs can be used to identify victims.

1.4.1 Introduction to Dental Radiographs

There are three common types of dental radiographs (dental X-rays): *bitewing*, *periapical*, and *panoramic*. Bitewing X-rays (Figure 1.2(a)) are taken during most routine dental check-ups and are useful for revealing cavities in the teeth. Periapical X-rays show the entire tooth, including the crown, root, and the bone surrounding the root (Figure 1.2(b)). One difference between periapical and bitewing radiographs is the imaging setup. For bitewing radiographs, the film is parallel to the teeth and the X-ray beam is perpendicular to both the teeth and the film. In contrast, periapical radiographs do not require that the film be parallel to the teeth. In some cases, the film and the teeth are deliberately set not to be parallel so that the whole tooth can be imaged on a small radiograph film. Periapical X-rays are useful for diagnosing abscessed teeth and periodontal disease. The third type of X-ray is the panoramic X-ray. As its name suggests, panoramic X-rays give a broad overview of the entire dentition (the development of teeth and their arrangement in the mouth). Panoramic X-rays provide information not only about the teeth, but also about upper and lower jawbones, sinuses, and other hard and soft tissues in the head and neck (Figure 1.2(c)). Panoramic films are entirely extraoral, which means that the film remains outside of the mouth while the X-ray machine shoots the beam through other tissues from the outside. Since it is entirely extraoral, panoramic radiographs work quite well for people who cannot tolerate the placement of films inside their mouths. Another advantage of panoramic film is that it takes very little radiation to expose it. The amount of radiation needed to expose a panoramic X-ray film is about the same as the radiation needed to

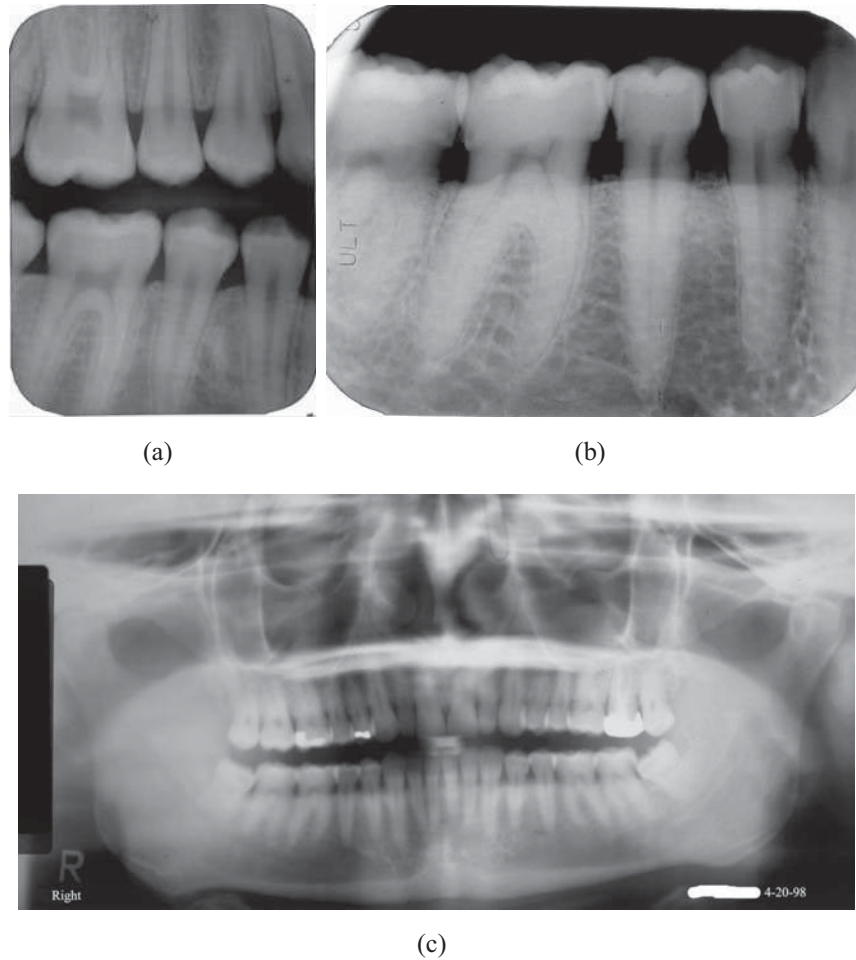


Figure 1.2. Three types of dental radiographs. (a) A bitewing radiograph; (b) a periapical radiograph; (c) a panoramic radiograph.

expose two intraoral films (periapical or bitewing). The disadvantage of panoramic radiographs is that the resolution is lower than for intraoral images, which means the edges and structures in the panoramic images are fuzzy.

For diagnosis and documentation purposes, dentists usually collect three types of dental radiograph series: the *initial full mouth series*, the *yearly bitewing series*, and the *panoramic X-ray film*. Figure 1.3(a) is an example of the initial full mouth series, which combines bitewing and periapical X-rays to show a complete survey of the teeth and bones. It consists of 2 or 4 bitewing films taken at an angle in order to look for decay, and 14 periapical films taken from other angles to show the tips of the roots and the supporting bone.

In the full mouth series, each tooth is seen in multiple films. This redundancy helps dentists create a mental image of the teeth in three dimensional (3D) space. A yearly bitewing series (Figure 1.3(b)) consists of either 2 or 4 bitewing films. A bitewing series is the minimum set of X-rays that most dental offices take to document the internal structure of the teeth and gums. The third type of radiograph series consists of a single panoramic radiograph.

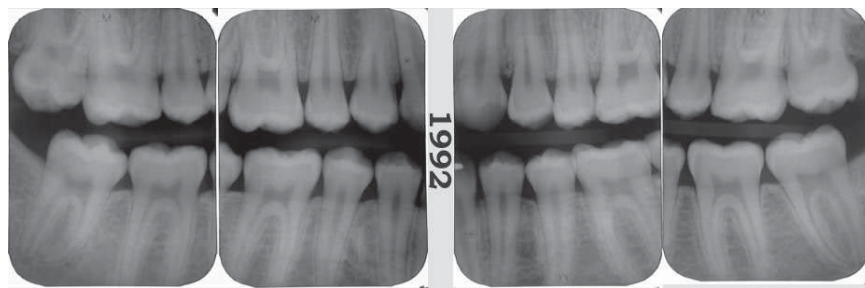
With the development of digital imaging technology, digital X-ray machines are becoming popular in dental clinics. Digital dental radiographs have several advantages [11]: i) compared to traditional radiographs, only half the dosage of radiation is needed for obtaining a dental radiograph of comparable quality; ii) digital dental radiographs do not require time needed for film development, so dentists need to wait for only a few seconds before the acquired image is displayed; iii) dentists can take another image instantly if the acquired image is not of good quality, so in general digital dental radiographs in a patient's record have better image quality than conventional dental radiographs; iv) digital radiographs are easier to store and process, while conventional radiographs need to be digitized for image processing; v) digital dental radiographs are environmentally friendly since they do not generate chemical wastes used in film processing; vi) digital radiographs also have been shown to have some diagnostic advantages for several diseases. Mainly due to their advantages in speed, storage, and image quality, digital dental radiographs will be routinely used for victim identification in the future.

1.4.2 Dental Radiographs for Identification

An individual's dentition includes information about the number of teeth present, the orientation of those teeth, and dental restorations. Each dental restoration is unique because it is designed specifically for that particular tooth. An individual's dentition is defined by a combination of all these characteristics, and the dentition can be used to distinguish one individual from another. The major challenge in the field of forensic dentistry is to determine how unique the features of an individual's dentition are, and whether this information



(a)



(b)



(c)

Figure 1.3. Three types of dental radiograph series. (a) Full mouth series; (b) bitewing series; (c) panoramic series.

is useful for identification purposes. The information about dentition is represented in the form of dental codes and dental radiographs. The dental codes are symbol strings for describing the type of dental restorations, the presence/absence of the teeth, and the number of cusps in the teeth, etc. Many studies have been done to define this characteristic of *uniqueness* in dental codes for identification purposes. Adams concluded from his analysis [8] [9] that when adequate antemortem dental codes are available for comparison, the inherent variability of the human dentition could accurately establish identity with a high degree of confidence. Adams further stated that the dentition is comparable in distinctiveness to the human mitochondrial sequence because of the abundant combinations of missing, filled, or unrestored teeth. Adams also noted that, like mitochondrial haplotypes, certain dental restorations are more common than others. When the dental features or mitochondrial sequences are unique, both techniques have the potential to produce identifications with high statistical certainty. However, both methods suffer when common characteristics (e.g., common dental restorations) are encountered.

One challenge to future efforts in forensic identification based on dental codes is the decline in the number of dental restorations that is attributed to increased awareness of dental hygiene. While general descriptions of dentition can be quite useful for excluding possible identities in cases where a limited number of identities are possible, large scale efforts to identify victims based on dentition are hindered when only dental codes are available. The availability of antemortem dental radiographs in addition to dental codes allows individuals with common dental characteristics to be distinguished from one another based on visual features in the images.

Forensic identification of humans based on dental information requires the availability of antemortem dental records, including dental radiographs, written records, tooth molds and photographs. Antemortem radiographs should be obtained if possible. The antemortem dental radiographs may have been acquired in several situations. Taking dental radiographs is very routine during the dental clinical visits in United States and Britain. Also in the



Figure 1.4. A forensic expert examines a dental radiograph film of a tsunami victim in Phuket, Thailand, on Jan. 11, 2005 [3].

United States and some other countries, newly recruited soldiers are required to have dental examinations that include taking their dental radiographs. The discovery and collection of antemortem records is ordinarily the responsibility of investigative agencies. These agencies might locate records from sources such as hospitals, dental schools, health care providers, dental insurance carriers, public aid insurance administrators, and the FBI National Crime Information Center (NCIC). Other resources include military service, judicial detention, oral surgeons, orthodontists, etc.

Recent disasters have brought the significance of dental identification to the public's attention. For example, in the terrorist attack in the United States on Sept. 11, 2001, many victims were identifiable only from pieces of jaw bones. Dentists were asked to help in identifying the victims using dental records and about 20% of the 973 victims identified in the first year after the 9/11 attack were identified using dental records [47]. A large number of victims of the 2004 Asian tsunami were also identified based on dental information. As reported in [59] and [6], 75% of the tsunami victims in Thailand were identified using dental records, 10% by fingerprints, and just 0.5% using DNA profiling. The remaining victims were identified using a combination of techniques. Figure 1.4 shows a forensic expert identifying a 2004 Asian tsunami victim based on radiographs.

1.5 Automatic Dental Identification

Identifying the 2,749 victims of 9/11 disaster took around 40 months [7], and the number of Asian tsunami victims identified during the first 9 months was only 2,200 (out of an estimated total of 190,000) [6]. The low efficiency rate of current manual dental identification methods makes it imperative that forensic science and computer science researchers work together to develop algorithms to automatically identify disaster victims. There have been a number of attempts to utilize machine intelligence techniques to facilitate the identification of victims. However, none of the existing approaches are based on a fully automatic interpretation of dental radiographs, so a human expert is needed for final victim identification.

This section begins with an overview of existing software for matching dental records to forensic evidence. This section also introduces the proposed system for automating the use of dental radiographs for victim identification and discusses some of the challenges for this proposed system.

1.5.1 Available Software for Matching Dental Records to Forensic Evidence

The most widely used software for matching dental remains to forensic evidence is **WinID** (<http://www.WinID.com>). This matching system uses information entered into the system by dental experts, including a series of dental characteristics regarding restoration and dentition descriptions (shown in Figure 1.5). The system then analyzes the manually input characteristics and generates a ranked list of possible identities based on similarities between the input characteristics and existing database entries [45]. The matching accuracy depends on the presence of dental restoration and abnormalities, which are becoming less prevalent due to increasing awareness of dental hygiene.

Another software package, called **OdontoSearch** (<http://www.jpac.pacom.mil/CIL/entry.htm>), can help determine the frequency of a

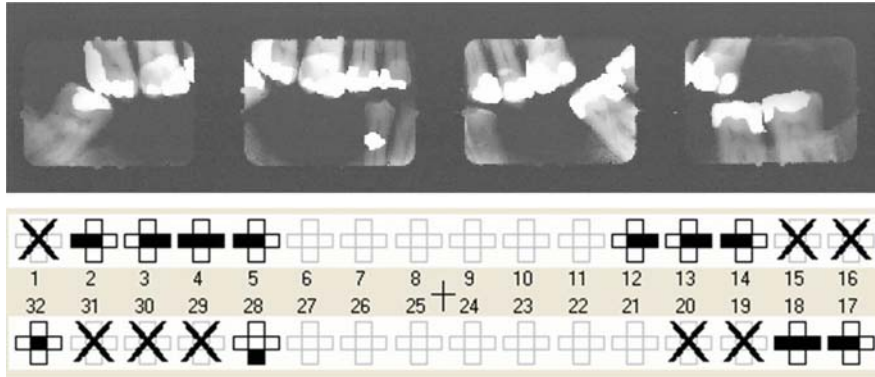


Figure 1.5. Dental radiographs and the corresponding description chart used by WinID system. The crosses indicate the missing teeth, and the filled squares indicate locations of the dental restorations in each tooth.

certain dental pattern in the population. This system utilizes a large sample set that is demographically and temporally distinct. The database contains the coded dental profile information, such as presence or absence of teeth or of restoration. This package reduces some of the subjectivity associated with determining the similarity of dental profiles, and allows forensic odontologists to infer the likelihood of a particular identification. However, the OdontoSearch software cannot be used to search for a victim's identity; it can only determine how common a particular dental profile is within the profile database.

In situations where antemortem radiographs are not available, it is difficult to determine the strength of a match between antemortem and postmortem dental profiles because the dental profile does not provide precise information about the dentition. The criteria for determining the strength of a match between two profiles are vague and subject to the opinion of the expert who analyzes the data. While fewer points of concordance are needed to establish a match between radiographic evidence than what is needed to establish a match between coded records, the exact number of points of concordance needed to establish a match is not universally agreed upon by the forensic odontology community [1]. As stated by Gustafson [35], "it would be unlikely for any two individuals to have identical dental characteristics, but it is quite possible for two people to have similar data on their dental

charts.”

The pros and cons of **WinID** and **OdontoSearch** are compared in table 1.2.

Table 1.2. A Comparison of WinID and OdontoSearch

	Pros	Cons
WinID	Retrieves subjects based on descriptions of dentition	<ul style="list-style-type: none"> ● Features are extracted manually ● Does not work for dentition without dental work
OdontoSearch	Measures reliability of a match	<ul style="list-style-type: none"> ● Cannot be used for subject retrieval ● Features are manually extracted ● Does not work for dentition without dental work

1.5.2 Dental Radiograph-based Automatic Identification System

Existing software for matching dental records to forensic evidence is based on dental description codes entered by human experts. The reduced prevalence of dental restorations limits the usefulness of matching methods based on dental descriptions and encourages continued research on the use of dental radiographs for identification. The goal of the proposed dental identification system is to automate the identification procedure and to explore new features for identification other than dental restorations and abnormalities. Figure 1.6 diagrams the proposed system for automatically identifying human subjects based on dental radiographs.

The first step in automatically identifying human subjects from dental radiographs is to extract features from the radiograph. An image quality evaluation function assesses the quality of the image before it is processed. A warning message is issued to request user interaction during the following steps if the quality of the image is assessed as *poor*. The features extracted for matching purposes are the contours of teeth and the contours of dental work. Before extracting these features, the radiographs are segmented into regions so that each region contains only one tooth. Boundary extraction methods are then applied to each region of the image to extract the contours of each tooth and dental restoration. An active shape model is trained and used for tooth contour extraction. To enhance radiograph images

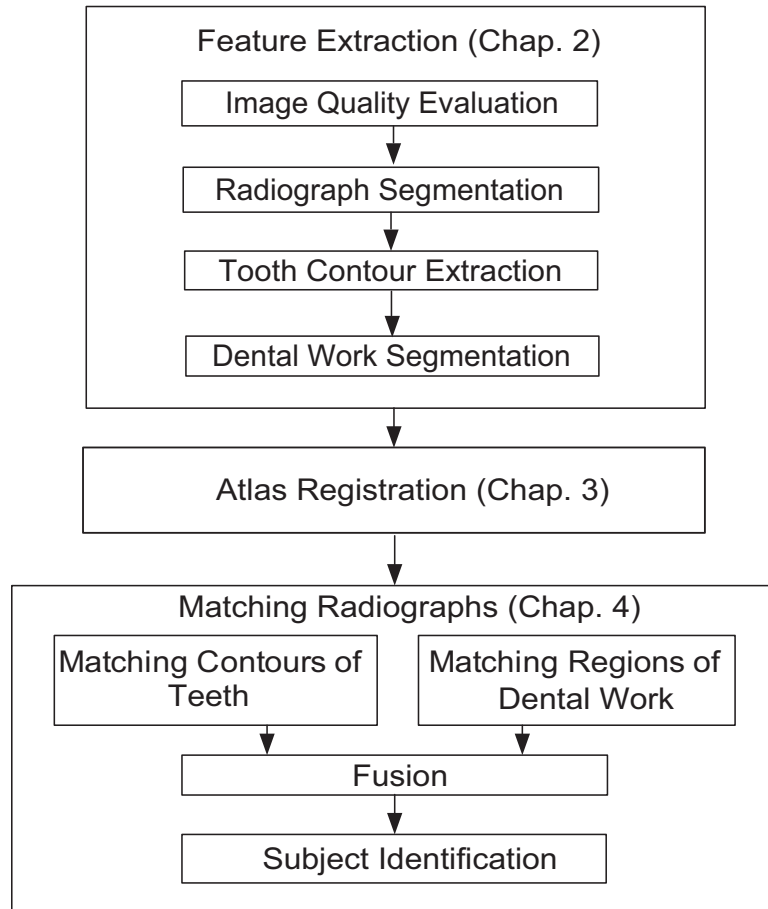


Figure 1.6. System diagram of automatic dental identification system.

and segment regions of dental work (including crowns, fillings, and root canal treatment), anisotropic diffusion is used. A monitoring scheme is developed to monitor the results of radiograph segmentation and tooth contour extraction. User interaction is requested if the results are erroneous. Chapter 2 describes the feature extraction process in more detail.

The second step, described in Chapter 3, is to register the radiographs to the human dental atlas, which is a descriptive model of the shape and relative positions of teeth. This registration step is important because the matching algorithm cannot properly align two sequences of teeth if they do not contain the same number of teeth. Missing teeth can be detected by labeling the existing teeth based on known dental anatomy. The anatomy-based tooth labeling can also accelerate the image matching stage, since a pair of PM-AM

images need not be matched if they do not share the same label. To label the teeth with anatomical indices, the dental radiographs are registered to the human dental atlas, which is a descriptive model of the shapes and relative positions of teeth. We propose a hybrid model involving Support Vector Machines (SVMs) and a Hidden Markov Model (HMM) for representation of the dental atlas and estimation of the tooth indices in dental radiograph images. A monitoring scheme is also developed to assess the results of automatic registration. Questionable registration results are interactively corrected by the system user.

Corresponding teeth from a PM and an AM radiograph are matched in the third stage of the matching system, which is described in Chapter 4. Tooth contours are matched for every pair of corresponding teeth, and if dental work is present in both the teeth, the dental work is also matched. A method is proposed for computing the distances between the given unidentified subject and all the database subjects based on the tooth indices obtained by registering the radiographs to the dental atlas. The database subjects are then sorted in ascending order of the matching distances and the results are presented to forensic experts for final analysis. Just as in other human identification systems, user interaction may be necessary in our system [58] [52].

Figures 1.7 and 1.8 show the process of matching two pairs of AM and PM images without and with user interaction for correcting errors during segmentation, contour extraction, and atlas registration.

1.5.3 Challenges

One major challenge in automatic identification of dental information is the poor image quality of dental radiographs. Whether due to incorrect operation of the X-ray equipment during image acquisition or digitization, to irregular arrangement of teeth, or to degradation of the radiograph films, the contours of teeth often appear to be blurred and the different tissues contrast poorly in many radiographs. These factors make it difficult to automatically extract edge features and tooth boundaries from the radiographs.

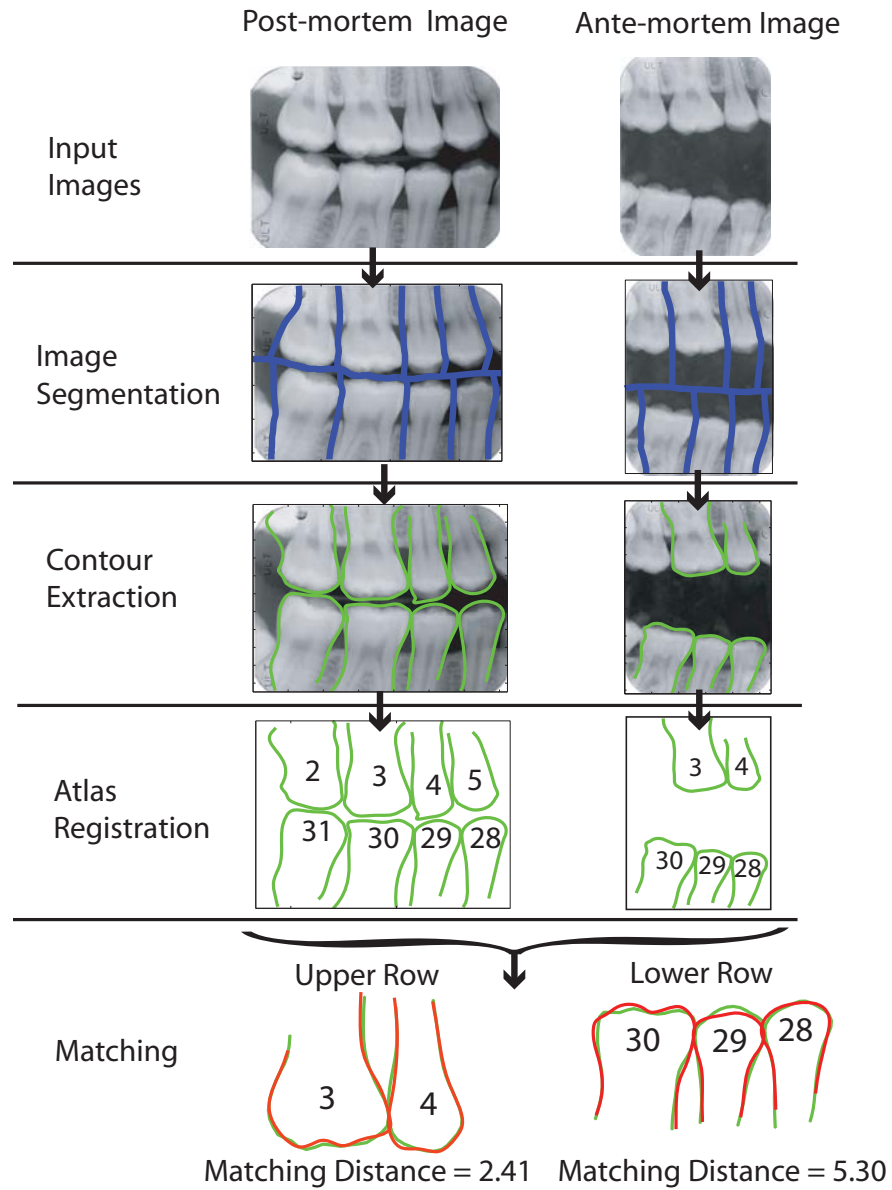


Figure 1.7. Fully automatic process of matching one pair of PM and AM images from the same subject.

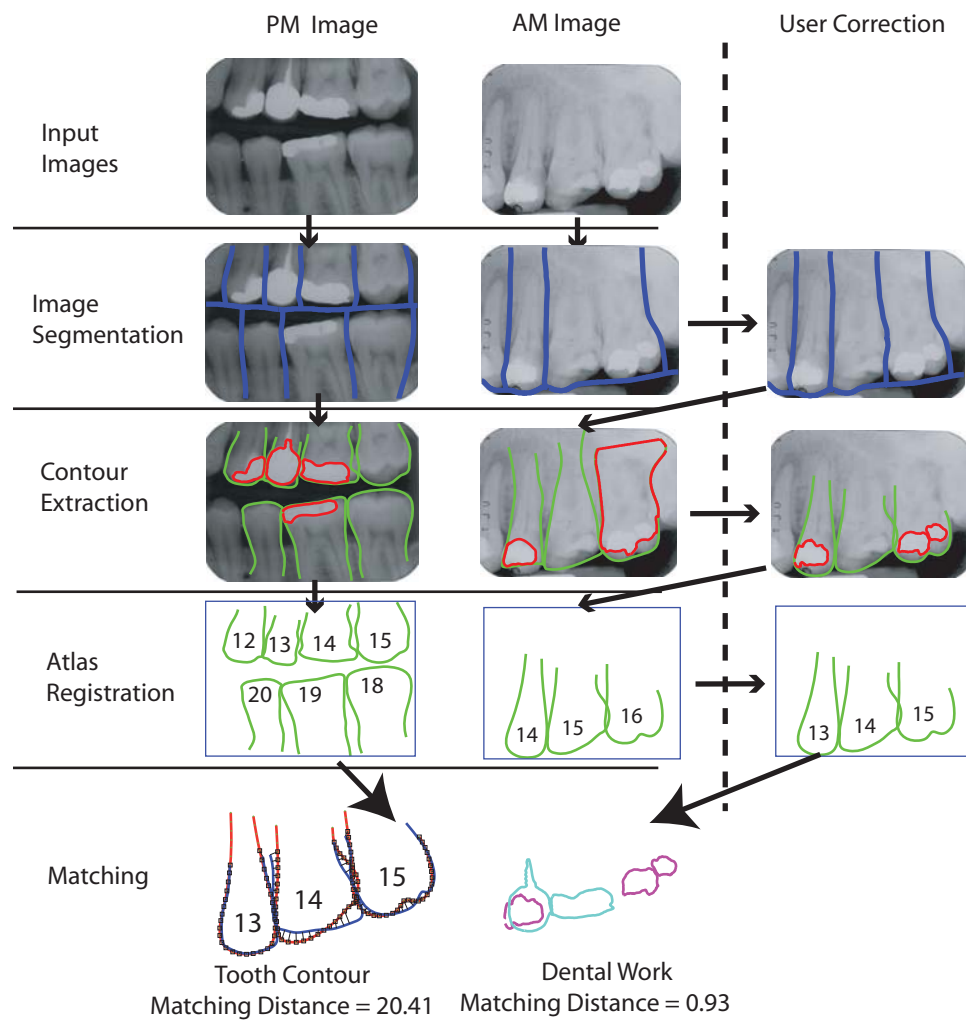
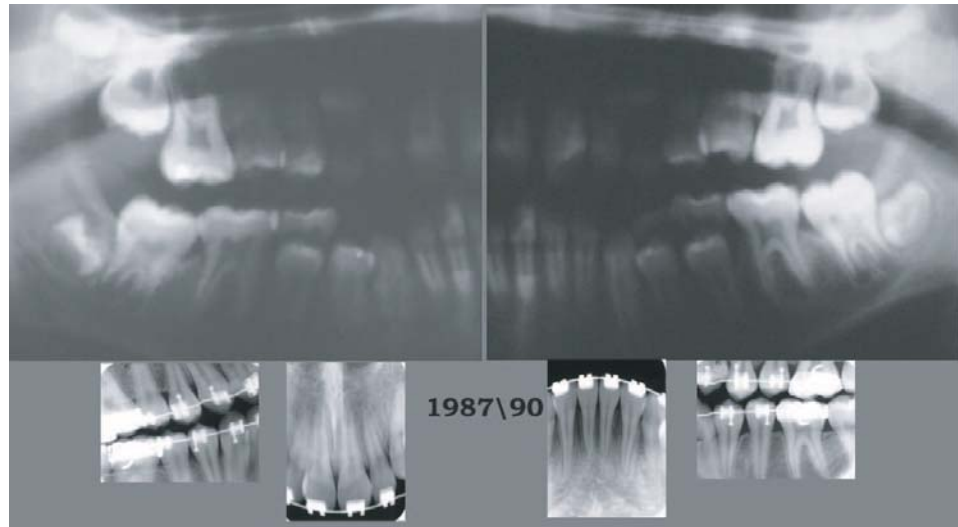


Figure 1.8. Automatic matching of one pair of PM and AM images with user interaction.

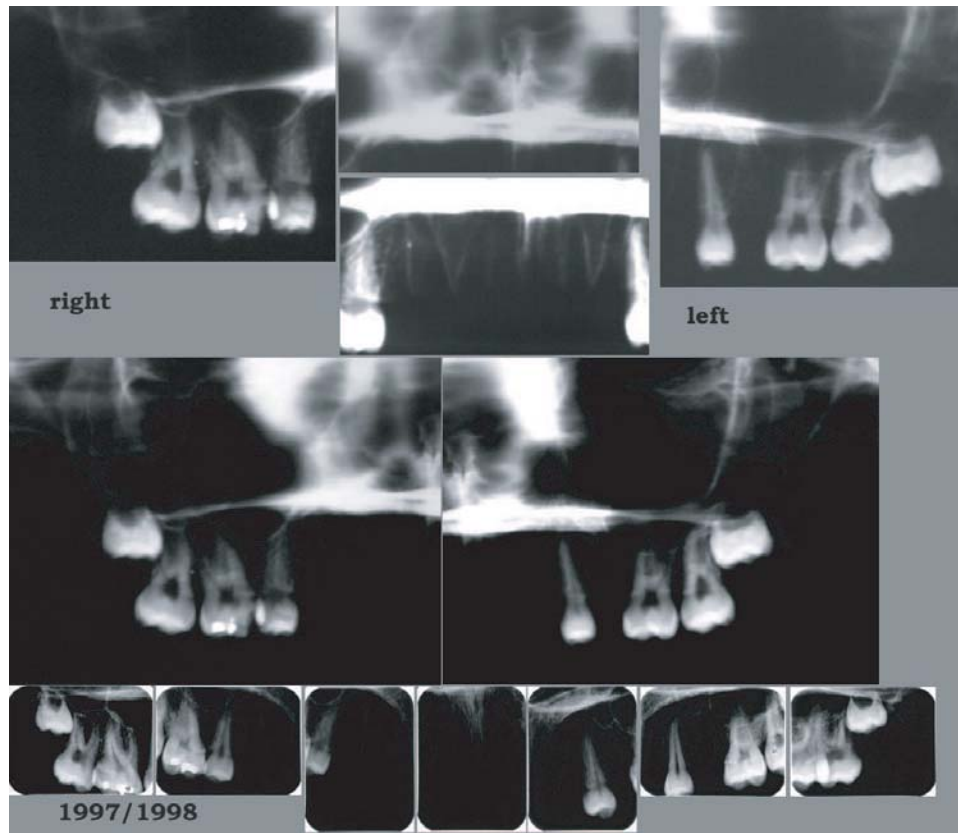
A second challenge is changes in the dentition over time, such as tooth eruption and loss, the emergence, abrasion, falling and replacement of dental restorations, the sliding of neighboring teeth after a tooth is extracted, orthodontic operations, etc. These changes cause inconsistent appearances of teeth in AM and PM radiographs from the same individual and are difficult to model. An example of a difficult identification case is shown in figure 1.9. The quality of the images is poor due to inappropriate exposure, and the orthodontics operation (shown in the AM images) and a number of missing teeth (shown in the PM images) have significantly changed the dentition appearance over time.

A third challenge in automatically identifying humans based on dental information is the changes in the imaging angle. Since dental radiographs are 2D projections of 3D structures, changes in the imaging angle result in complex deformations in the 2D projections that are difficult to model without any information about the 3D dimensions of the teeth. Changes in the imaging angle are smaller for bitewing and panoramic images than for periapical images, because of the fixed setup for acquiring bitewing and panoramic images. Figure 1.10 shows an AM-PM image pair in which the changes in the imaging angle result in significant deformations in the periapical radiograph images.

A fourth challenge is the insufficiency of data in dental radiograph databases. We obtained dental radiographs from three sources. The first source is the FBI's Criminal Justice Information Service (CJIS) division, which is interested in utilizing dental radiographs for identifying Missing and Unidentified Persons (MUPs). The second source is the Washington State Police Department, and the third source is Dr. Howell, a professor in the Department of Oral and Maxillofacial Pathology at West Virginia University. The three data sets are combined into a database containing 33 subjects, each with a number of AM and PM images. If we view upper and lower rows of teeth as separate sequences, there are a total of 360 PM and 316 AM dental sequences, containing a total of 810 PM teeth and 892 AM teeth. Figure 1.11 shows some of the images in the database. A larger database used in the experiments contains 100 unmatched AM subjects, which are composed of 748



(a)



(b)

Figure 1.9. Antemortem (a) and postmortem (b) radiographs of a difficult identification case for an automatic matching system. The poor image quality poses difficulties for contour extraction. The orthodontics operation in (a) and missing teeth in (b) have significantly altered the dentition appearance over time.

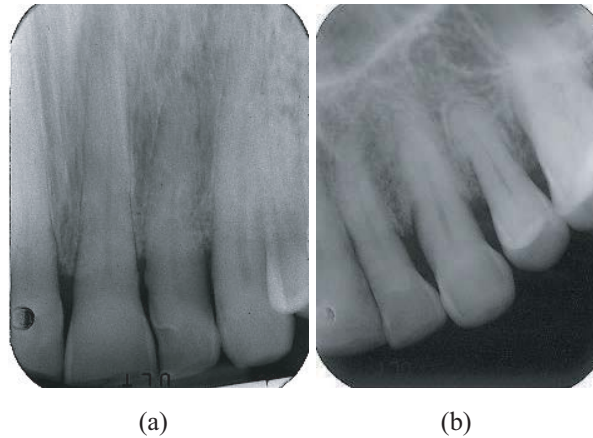


Figure 1.10. Changes in the imaging angle result in significant deformations in the appearances of corresponding teeth in (a) AM and (b) PM periapical radiograph images.

AM sequences and 2,379 AM teeth. The small number of subjects in the database makes it difficult to provide a sufficient number of matched pairs for training and performance evaluation of the system.

1.6 Summary

Human identification using dental radiographs is an important but very challenging research topic. This chapter introduced the background on forensic identification of humans, especially the dental radiograph-based approach. Challenges to automatic processing and matching of dental information were also discussed, and each stage in the proposed automatic identification system was described. The following chapters detail each stage of the proposed automatic system for human identification based on dental information.



Figure 1.11. Some images in the dental radiograph database.

CHAPTER 2

Segmentation and Contour Extraction

This chapter introduces methods for evaluating image quality, segmenting radiographs and extracting features from dental radiographs. Image quality affects the accuracy of automatic algorithms in all the processing stages. To detect images of poor quality, an image-quality evaluation method is designed to identify difficult images and request user interactions after the automatic processing results are produced.

The features extracted from dental radiographs for matching purposes are the contours of teeth and the contours of dental work, such as crowns and fillings. In order to automatically extract these features, the radiographs are first segmented into regions such that each region contains only one tooth. Contours of teeth and dental work are then extracted from each region.

We propose a method for segmenting dental radiographs based on fast marching algorithm [54]. To correct the segmentation errors, an interactive semiautomatic method is also developed. We also propose a method for extracting the contours of teeth using active shape models. Dental work, such as crowns, fillings, and evidence of root canal treatment are composed of radio-opaque materials, like silver, gold, and CaOH. These materials appear as bright regions in radiographs. To identify the dental work contours, an anisotropic diffusion-based technique is used to enhance the radiographs. The regions of dental work

are then segmented using image thresholding.

2.1 Automatic Image Quality Evaluation

Images of poor quality pose difficulties at every stage of feature extraction and matching. In our database, all the radiograph images were scanned from photographic films, which reduces the number of levels of intensity and introduces problems such as over-exposure. Due to the fact that the AM images were usually acquired many years before they were actually scanned and were stored in non-ideal condition, there is also loss of contrast and resolution.

Evaluation of image quality is needed so that for poor quality images, the system user can interactively correct the results obtained automatically. The evaluation of image quality consists of the following steps:

1. Detection of panoramic images;
2. Detection of intensity imbalance;
3. Detection of image blurring.

The details of these steps are given below.

2.1.1 Detection of Panoramic Images

Since panoramic images have more teeth than bitewing and periapical images, when scaled to a certain size, panoramic images have more high frequency components and fewer low frequency components compared to bitewing and periapical images. The detection algorithm is as follows:

1. Image is first scaled so that the longest side of the resulting image is 256 pixels;
2. A Fast Fourier Transform is applied to obtain a 256×256 image in frequency domain, and the magnitude of the components of frequency at $1/(256pixels)$ is computed;
3. If the magnitude of the frequency at $1/(256pixels)$ is less than a threshold value

(3,400,000), the image is a panoramic image. Otherwise, it is a bitewing or periapical image. The threshold value was empirically determined.

Experiments on 206 randomly selected images (51 panoramic images and 155 bitewing and periapical images) showed that only 3 panoramic images and 4 bitewing/periapical images were misclassified using this algorithm.

2.1.2 Detection of Intensity Imbalance

Intensity imbalance means that the images are over-exposed, under-exposed, or partially over-exposed and/or partially under-exposed. The rules for detecting intensity imbalance are as follows:

1. If more than half of all pixels in the image are darker than $1/4th$ of the intensity range (255 in our experiments), the image is under-exposed (Figure 2.1(a));
2. If more than half of all pixels in the image are brighter than $3/4th$ of the intensity range (255 in our experiments), the image is over-exposed (Figure 2.1(b));
3. Segment the image into four equally sized blocks (upper left, upper right, lower left, and lower right). Calculate the mean pixel intensities of the blocks, and calculate the standard deviation of the mean intensities ($STDMI$). If $STDMI$ is larger than 25, the image is not homogeneously exposed (Figure 2.1(c)).

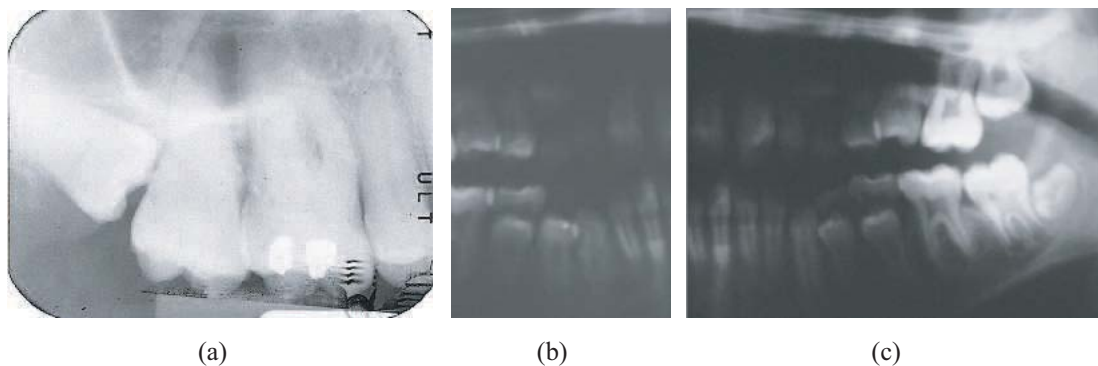


Figure 2.1. Detection of intensity imbalance. (a) An over-exposed image; (b) an under-exposed image; (c) a non-homogeneously exposed image with $STDMI = 30$.

2.1.3 Blur Detection

Due to out-of-focus errors during image acquisition, the image may appear to be blurred, which poses difficulty for feature extraction. To detect the blur, a Gaussian kernel of 5×5 pixels with $\sigma = 0.5$ is convolved with the original image. The Mean of the Absolute Difference (*MAD*) between the original image and the result of convolution is used to detect the blur. If the original image is blurred, the *MAD* value will be small since the convolution does not significantly increase the degree of blur. In practice, images with $MAD < 2$ are categorized as blurred images. Figure 2.2 shows two images, one detected as a sharp image (Figure 2.2 (a)) and the other as a blurred image (Figure 2.2 (b)).

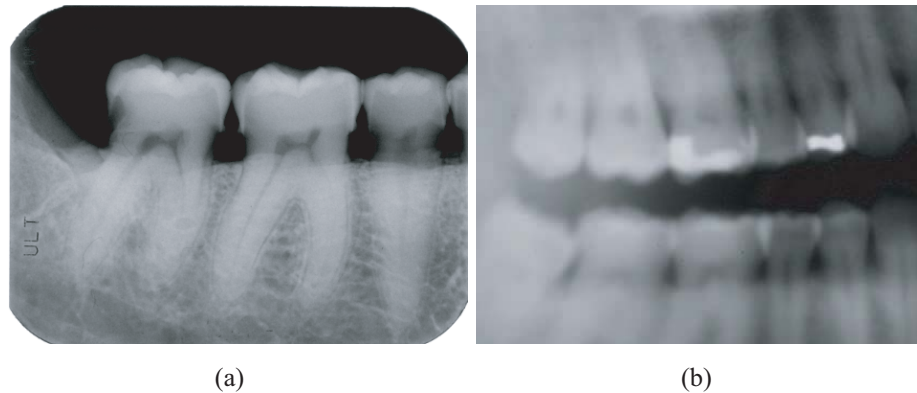


Figure 2.2. Detection of blur. (a) A sharp image with $MAD = 2.35$; (b) A blurred image with $MAD = 1.08$.

2.2 Radiograph Segmentation

The goal of radiograph segmentation is to find the region of interest (ROI) associated with every tooth in the image. For simplicity, we assume there is only one row each of maxillary (upper jaw) and mandibular (lower jaw) teeth in the image. This assumption is usually true, except for children who are at the stage of losing their primary teeth. For them, both the rows of permanent teeth and the rows of primary teeth are present in dental radiographs (Figure 2.3). Once the upper and lower rows of teeth are separated, each tooth needs to



Figure 2.3. A dental radiograph of a child showing both permanent teeth and primary teeth.

be isolated from its neighbors. A method based on fast marching algorithm is proposed to automate the whole segmentation process. In general, radiograph segmentation has three steps:

1. Segmentation of upper and lower rows of teeth;
2. Detection of the presence of upper (lower) rows of teeth;
3. Isolation of neighboring teeth in each row.

The details of each step are given in the remainder of this section.

2.2.1 Automatic Segmentation

Fast marching methods [54] find the shortest path between a set of start points and a set of end points in an image by propagating a wave from the start points. When the wave front touches one of the end points, the shortest path is established by tracking the steepest gradient descent from the touched end point back to the start point. The wave propagation is described by the Eikonal equation [54]:

$$|\nabla T|F(x, y) = 1, \quad (2.1)$$

where T is the wave front, and $F(x, y)$ is the propagation speed. Equation (2.1) can be solved efficiently by using heaps, which allows the solution to be obtained in a reasonable

amount of time.

The speed parameter in the fast marching algorithm depends on the application. In order to detect the paths that segment teeth in radiographs, the propagation speed is set as a function of the pixel values:

$$F(x, y) = ((\max - I(x, y))/(\max - \min))^2 + 0.01, \quad (2.2)$$

where $I(x, y)$ is the gray level value of the pixel at point (x, y) , and \min and \max are the minimum and the maximum intensity values of pixels in the image. The speed configuration sets lower propagation speed for pixels of higher gray values (brighter), and higher propagation speed for pixels of lower gray values (darker). Bright pixels correspond to teeth and darker pixels correspond to soft tissue and air. So, the wave propagates more slowly along the tooth pixels than along the pixels of other tissues.

The line segmenting the upper and lower rows of teeth is detected first. A wave propagates from the left side of the image and ends at the right side of the image. The wave propagates faster in the area between the upper and lower rows of teeth because it has lower gray values than the tooth pixels. Thus, the fastest path must pass through the area that separates the two rows of teeth. The fastest path is the line (denoted as sv) segmenting the upper and lower rows of teeth.

The presence of upper and lower rows of teeth is detected by using the position of the separating line, sv . Denote the y coordinates of points in the segmentation line sv as sv_y , and the height of the image as H (see Figure 2.4). The following classification rules are used to determine which rows of teeth are present in the image:

- if $\min sv_y \geq \frac{1}{6}H$ and $\max sv_y \leq \frac{5}{6}H$, then there must be **two rows** of teeth in the image; otherwise,
- if $\min sv_y < \frac{1}{6}H$, then there should be only the **lower row** of teeth in the image; otherwise,

- if $\max sv_y > \frac{5}{6}H$, then there should be only the **upper row** of teeth in the image.

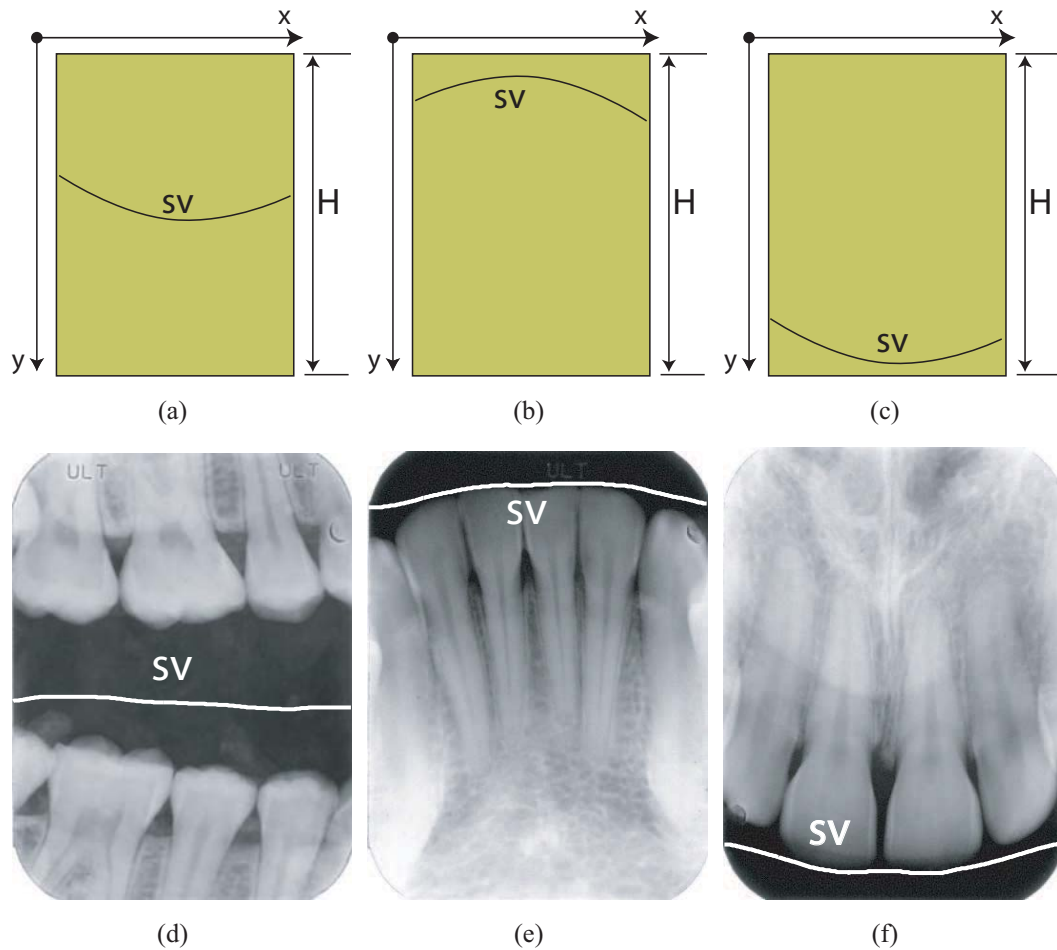


Figure 2.4. Classification of image types based on number of rows of teeth. (a) and (d) images with two rows of teeth; (b) and (e) images with only lower row of teeth; (c) and (f) images with only upper row of teeth.

Once the upper and lower rows of teeth are segmented, the neighboring teeth in each row are isolated using the fast marching method, which finds the separating lines that originate at the segmentation line sv and propagate either to the top or bottom of the image through gaps between the teeth. The gray values of the pixels in the regions between the teeth are also lower than the gray values of the tooth pixels, so the speed parameter is set the same way as in Equation (2.2). There are two steps for isolating teeth in the upper row:

- 1) **Finding knots in the segmentation line sv .** Denote the points where the lines

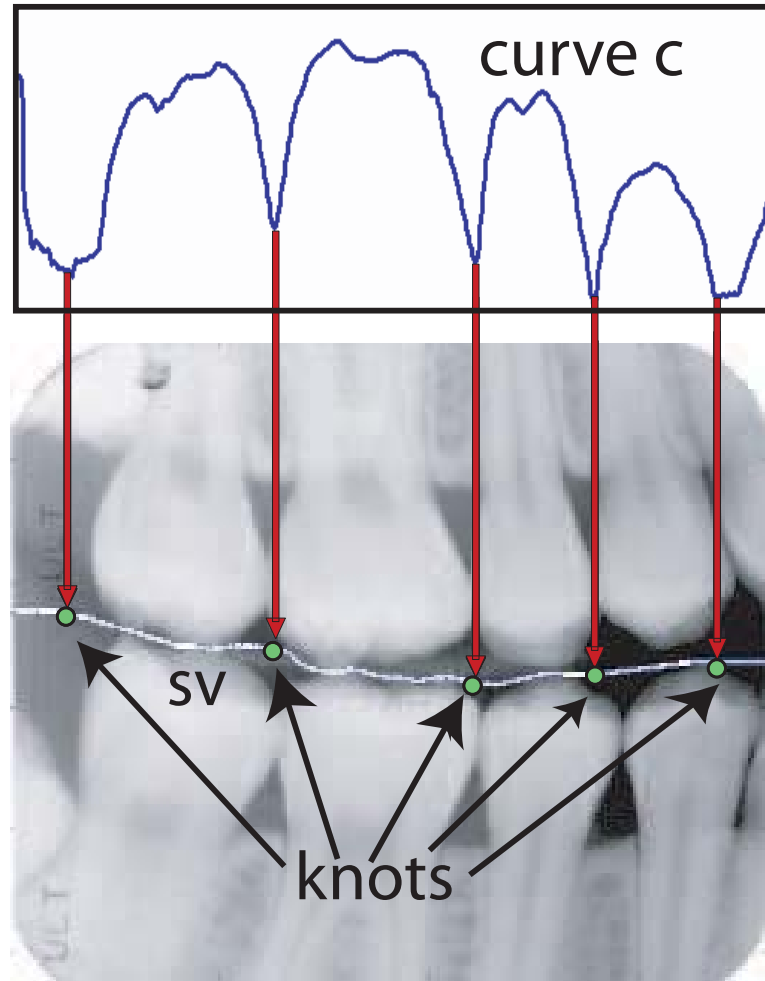


Figure 2.5. Finding knots in the segmentation line.

separating neighboring teeth touch the segmentation line, sv , as knots. Sum up values of the pixels above the segmentation line sv (integral projection) to form a curve, C . Knots in the segmentation line sv are points having the same x -coordinates as the valleys in the curve, C . Figure 2.5 illustrates the curve C and the knots.

2) Finding the isolation lines. For every knot t , find the shortest path from t to the top of the image. This fastest path always goes through the gap between neighboring teeth and isolates the two teeth.

The algorithm for segmenting individual teeth in the lower row is the same as for segmenting teeth in the upper row. Figure 2.6 shows some results of successful automatic

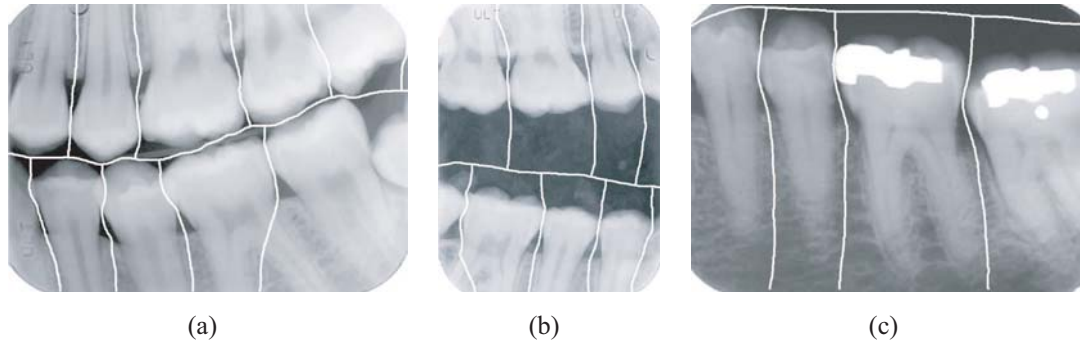


Figure 2.6. Some examples of correct segmentation.

segmentation.

Table 2.1 shows the results of applying the automatic radiograph segmentation algorithm to 611 dental radiograph images. On average, the entire segmentation process (implemented in C) takes ~ 2.5 seconds for a 300×250 image containing 8 teeth on a PC with a 2.99 GHz Pentium 4 processor. There are four types of errors that our algorithm makes (see Figure 2.7): incorrect location of segmentation line between upper and lower teeth, under segmentation, over segmentation, and improper segmentation. The first type of error occurs when the dental work present in upper and lower rows of teeth appears to be connected to form a single block in the radiographs. In this situation, the wave does not propagate sufficiently fast through the middle of the block, so the estimated separating line tries to avoid the dental work and therefore segments the upper and lower rows of teeth incorrectly (Figure 2.7(a)). This type of error also occurs when the space between upper and lower rows of teeth is not fully captured in the radiograph (Figure 2.7(b)). The under segmentation errors occur when the dental work or teeth overlap in the radiograph, leaving the gap between the teeth invisible (Figure 2.7(c)). Over segmentation errors occur when the space between cusps of a tooth creates a valley in the integral projection and the pixel intensity of the teeth is not sufficiently high to block the propagation of the wave (Figure 2.7(d)). Improper segmentation refers to the result in which the segmentation line goes through the inside of a tooth. This is caused by the overlapping dental work, which blocks

the propagation of the wave at the gap between teeth (Figure 2.7(e)).

Table 2.1. Results of Automatic Radiograph Segmentation

Segmentation Results	Percentage
Correct Segmentation	61.1%
Incorrect Segmentation Line Between Upper and Lower Teeth	11.1%
Under Segmentation	17.8%
Over Segmentation	3.0%
Improper Segmentation	7.0%

2.2.2 User Interaction

An algorithm is developed for detecting the following types of aberrant segmentation lines:

1. The segmentation line between upper and lower rows of teeth passes through the middle of teeth (Figure 2.7(a)). This type of error is detected if the variation of the pixel intensities along the segmentation line is larger than 100.
2. The segmentation line between upper and lower rows of teeth has sharp turns due to the upper and lower teeth biting together and blocking the wave propagation during detection of the segmentation line (see Figures 2.7(b) and 2.8(a)). This type of error is detected if the largest gradient in y coordinates of the segmentation line is larger than 20 pixels.
3. Under segmentation and over segmentation (Figures 2.7(c), (d) and (e)) are detected by computing the ratio of maximum interval to minimal interval between isolation lines. If the ratio is over 2, a warning message is issued.

Interactive methods based on fast marching algorithms have been developed to assist the system user in correcting all the above segmentation errors. After a user specifies some points in the image that the correct segmentation line must pass through, the fastest paths are established between the specified points and the original starting and ending points, and all line segments are then connected to form the final segmentation line. Figures 2.8, 2.9, 2.10, and 2.11 show user interactions for correcting the four types of segmentation errors.

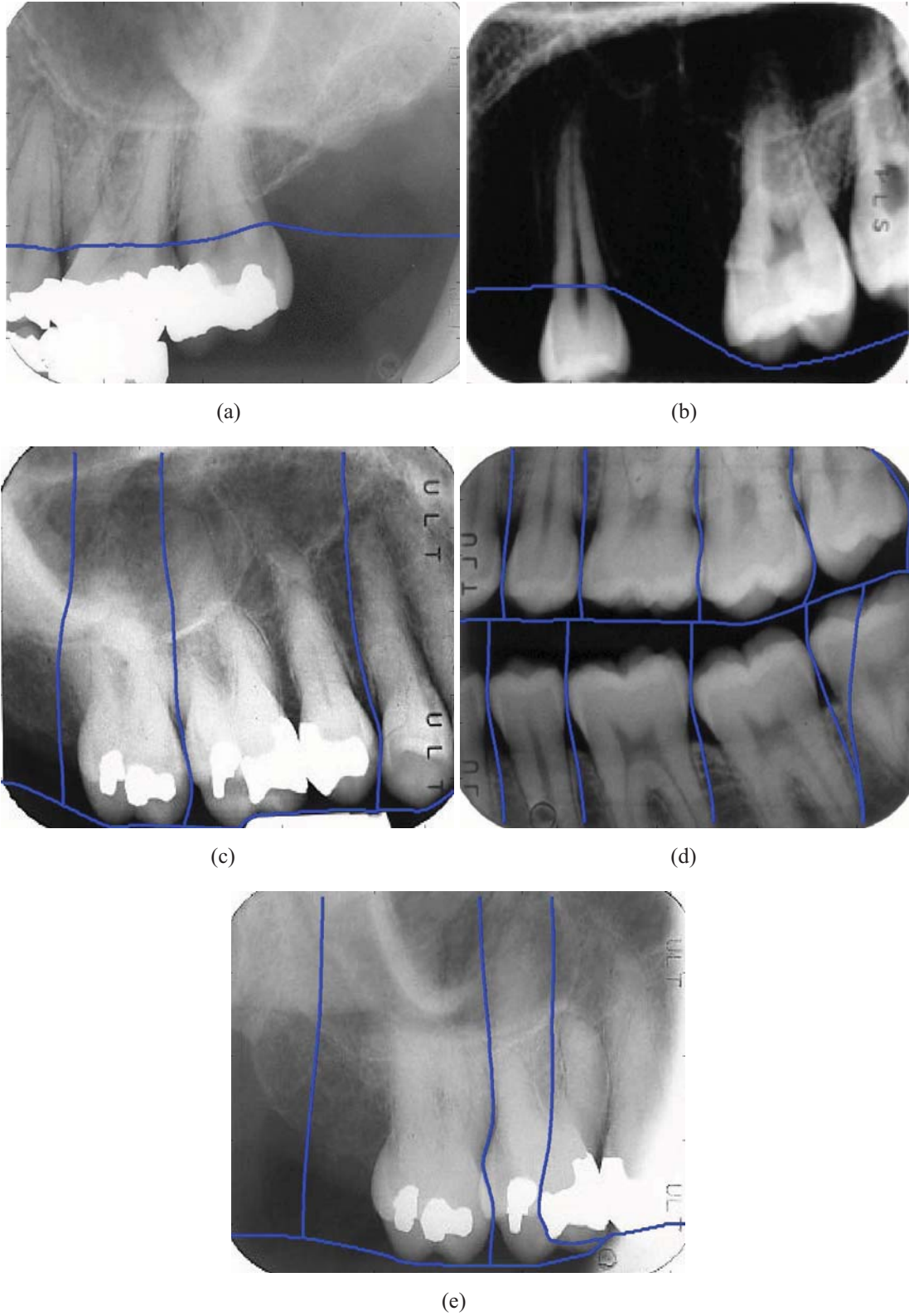


Figure 2.7. Some results of incorrect automatic segmentation. (a) and (b) incorrect location of segmentation line between upper and lower rows of teeth; (c) under segmentation; (d) over segmentation; (e) improper segmentation.

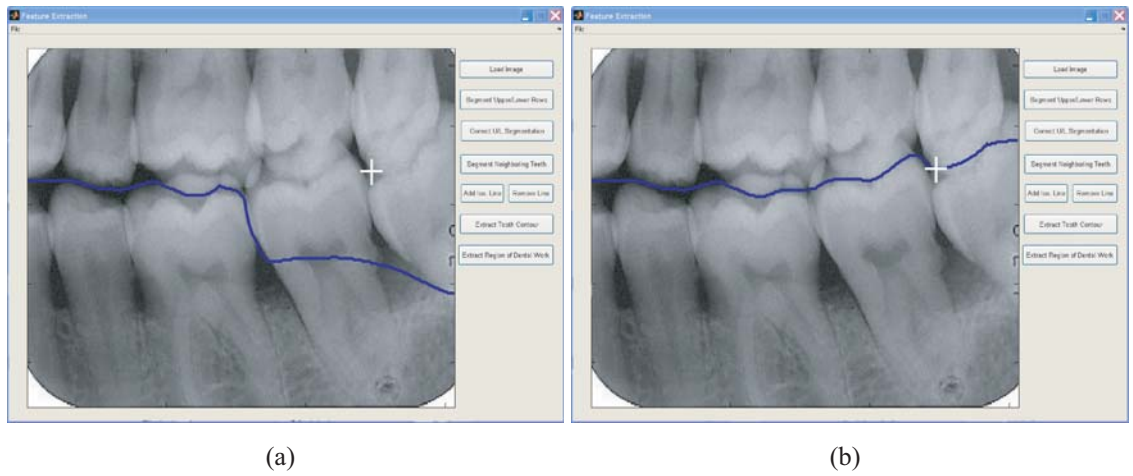


Figure 2.8. User interaction for correcting of the first type of error: incorrect location of segmentation line between upper and lower rows of teeth. (b) Correction of the incorrect segmentation line between upper and lower teeth in (a) by specifying one point (shown as cross).

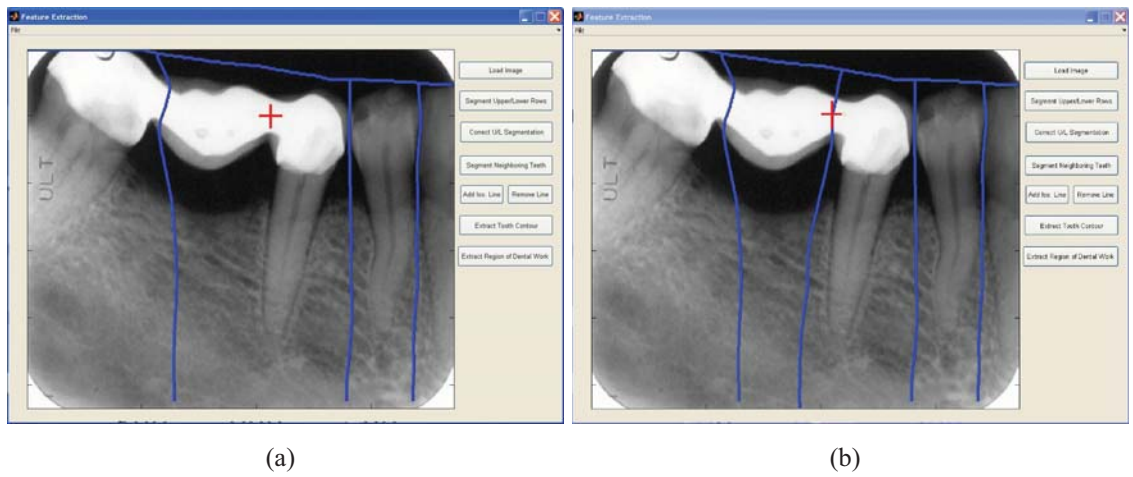


Figure 2.9. User interaction for correcting of the second type of error: under segmentation. (b) Adding an isolation line in (a) by specifying one point (shown as cross).

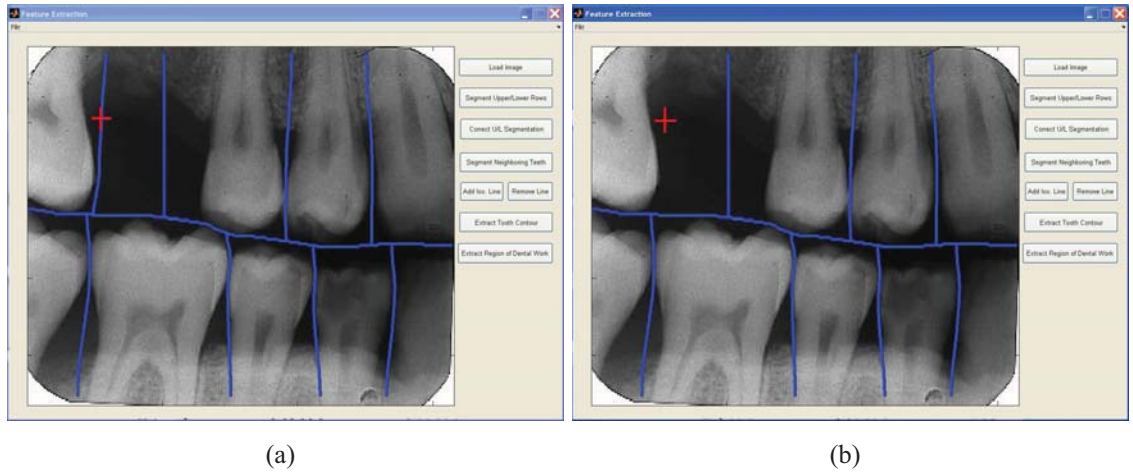


Figure 2.10. User interaction for correction of the third type of error: over segmentation. (b) Removing an extra isolation line in (a) by specifying one point (shown as cross).

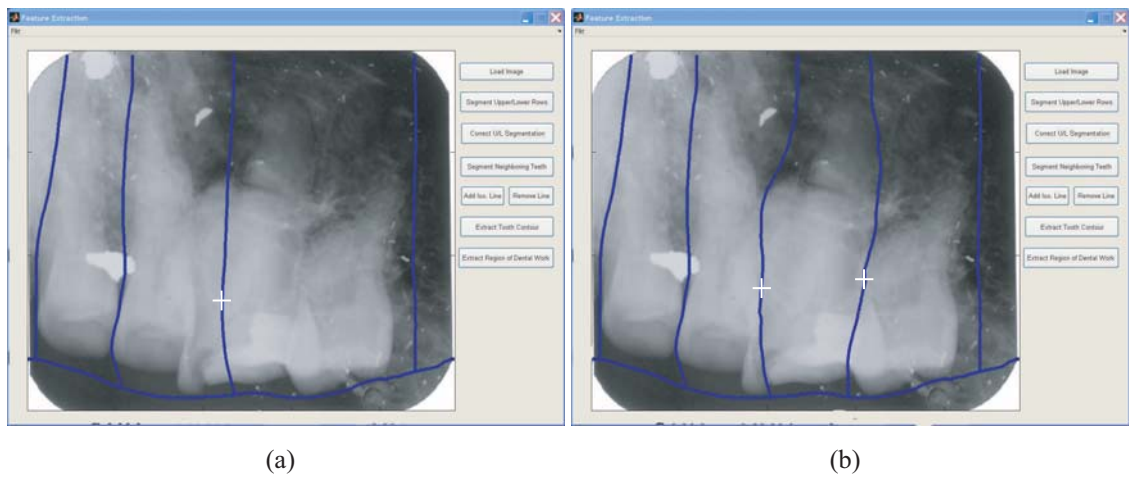


Figure 2.11. User interaction for correction of the fourth type of error: improper segmentation. (b) Correction of an improper segmentation by removing the improper segmentation line in (a) by specifying one point (shown as cross in (a)) and adding correct segmentation lines by specifying two points (shown as cross in (b)).

2.3 Extracting Tooth Contours

A region of interest (ROI) for a tooth is defined as an enclosing rectangle that tightly fits the segmented area (Figure 2.12). We propose an algorithm for extracting the tooth contours using active shape models.

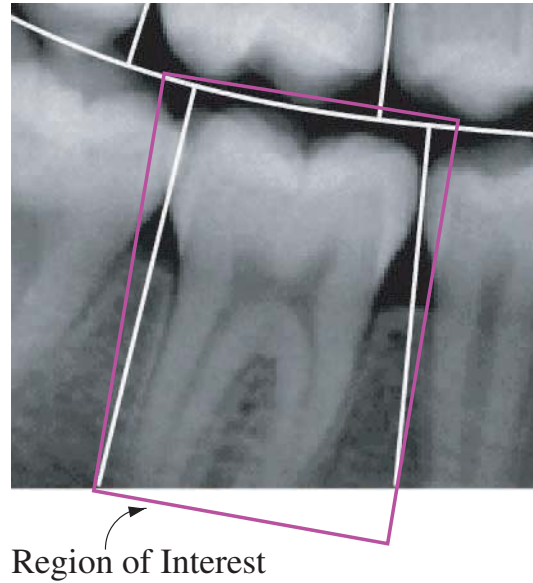


Figure 2.12. Region of Interest (ROI) for a tooth.

2.3.1 Introduction to Active Shape Models

Active Shape Models (ASMs) [23] are deformable models used for shape extraction. Unlike the active contour models (snakes), ASMs incorporate statistical global constraints on shapes. ASMs utilize the Principal Component Analysis to discover the principal modes of deformation among training shapes and find the most plausible shapes in the image with respect to the detected principal deformation. The details of the algorithm are introduced as follows [57]. Consider N planar training shapes each consisting of n boundary points. Let each shape be represented as:

$$\mathbf{x}_i = [x_1^i, x_2^i, \dots, x_n^i, y_1^i, y_2^i, \dots, y_n^i]^\top, i = 1, \dots, N, \quad (2.3)$$

where $(x_k^i, y_k^i), k = 1, \dots, n$ is the coordinate of point k in the i th shape. A linear orthogonal transformation, \mathbf{M} , of the data is designed to obtain the compact representation of \mathbf{x}_i , denoted as \mathbf{z}_i , where

$$\begin{aligned}\mathbf{z}_i &= \mathbf{M}(\mathbf{x}_i - \bar{\mathbf{x}}), \\ \bar{\mathbf{x}} &= \frac{1}{N} \sum_{i=1}^N \mathbf{x}_i,\end{aligned}\tag{2.4}$$

so that the covariance matrix of \mathbf{z}_i is a diagonal matrix. The mean of the \mathbf{z} -variables can then be expressed as:

$$\bar{\mathbf{z}} = \frac{1}{N} \sum_{i=1}^N \mathbf{z}_i = \mathbf{M} \cdot \left[\frac{1}{N} \sum_{i=1}^N (\mathbf{x}_i - \bar{\mathbf{x}}) \right] = \mathbf{0}.\tag{2.5}$$

The shape covariance matrix of \mathbf{x}_i is defined as

$$\Sigma_{\mathbf{x}} = \frac{1}{N} \sum_{i=1}^N (\mathbf{x}_i - \bar{\mathbf{x}})(\mathbf{x}_i - \bar{\mathbf{x}})^\top.\tag{2.6}$$

The covariance matrix of \mathbf{z}_i is defined as

$$\begin{aligned}\Sigma_{\mathbf{z}} &= \frac{1}{N} \sum_{i=1}^N (\mathbf{z}_i - \bar{\mathbf{z}})(\mathbf{z}_i - \bar{\mathbf{z}})^\top \\ &= \mathbf{M}\Sigma_{\mathbf{x}}\mathbf{M}^\top.\end{aligned}\tag{2.7}$$

Since \mathbf{M} is orthogonal, i.e., $\mathbf{M}^{-1} = \mathbf{M}^\top$, equation (2.7) can be changed into the following:

$$\Sigma_{\mathbf{x}}\mathbf{M}^\top = \mathbf{M}^\top\Sigma_{\mathbf{z}}.\tag{2.8}$$

So a possible solution for \mathbf{M}^\top is the (column) eigenvectors of the covariance matrix $\Sigma_{\mathbf{x}}$, and the diagonal of the covariance matrix $\Sigma_{\mathbf{z}}$ contains the corresponding eigenvalues. According to equation (2.4),

$$\mathbf{x}_i = \bar{\mathbf{x}} + \mathbf{M}^\top \mathbf{z}_i,\tag{2.9}$$

where each eigenvector column in M^T represents a typical variation among the shapes. This gives a different perspective on shapes: a particular shape can be viewed as the mean shape plus the sum of the weighted principal deformations. With this view point, the problem of detecting a shape is reduced to finding the correct coefficients, z_i .

There are usually three steps in applying ASMs to shape extraction problems:

1. *Shape Alignment*: Align training shapes to find the corresponding points;
2. *Modeling Shape Variation*: Find eigenvectors of the covariance matrix of the shapes, and the appropriate number of eigenvectors for representing the shape variations;
3. *Shape Extraction*: Use the statistical shape model to extract shapes from images.

The remainder of this section provides details of the above steps for extracting tooth contours.

2.3.2 ASM-Based Tooth Contour Extraction

In this section, we introduce the method for aligning the training tooth contours, provide a method for modeling shape variations including scaling and rotation, and describe a procedure for using the trained model to extract tooth contours in dental radiographs.

Shape Alignment

Before aligning training shapes, a prototype shape is created manually (Figure 2.13(a)). a precise definition of prototype shape is not needed; a typical shape of teeth with approximate height and width is good enough. It is used for aligning all three types of teeth: incisors, (bi)cuspid and molars. The training shapes are aligned to the prototype shape by first rotating them so that their tightest bounding boxes are in the upright positions. Then training shapes are scaled so that their heights become the same as the prototype (Figure 2.13(a)). Given a point x_0 in the prototype and a point set X , which contains points in

an aligned training shape, \mathbf{x}_0 's corresponding point \mathbf{x} in the training shape is detected as follows:

$$\mathbf{x} = \arg \min_{\mathbf{x}' \in \mathbf{X}} \|\mathbf{x}' - \mathbf{x}_0\|, \quad (2.10)$$

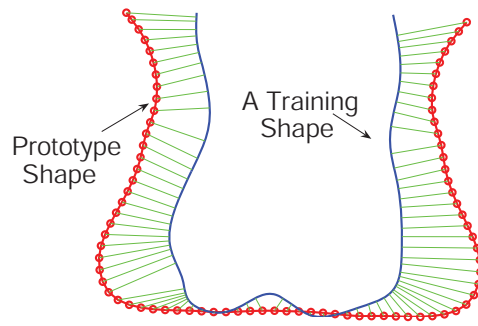
where $\|\cdot\|$ represents the Euclidean distance.

Modeling Shape Variation

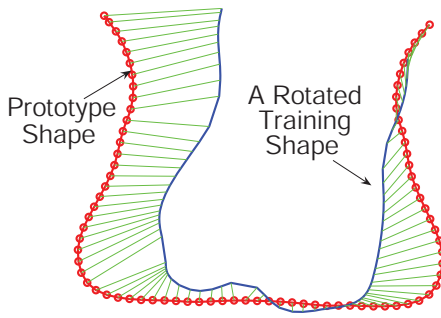
Traditional ASMs do not model scaling and rotation. To use the traditional ASMs for shape extraction, an additional linear transformation, including translation, scaling, and rotation, has to be imposed on the nonlinear transformation modeled by the ASMs. Both the ASM-based nonlinear transformation and the linear transformation take place simultaneously, but are handled sequentially, which is not only time consuming, but also makes it difficult to find an optimal solution.

We propose to solely use ASMs to represent the overall transformation, including scaling and rotation. To incorporate the scaling and rotation into the ASM model, scaling and rotation are applied to training shapes after point correspondence between the training shapes and the prototype shape has been established. Figures 2.13 (b) and (c) show the rotated and the scaled training shapes corresponding to the original training shape in Figure 2.13 (a).

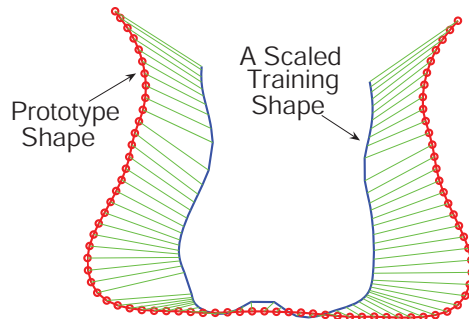
After the shape alignment is done, the principal modes of deformation are extracted as the eigenvectors of the covariance matrix of the shape vectors. Figure 2.14 shows the first five modes of shape variation captured by the trained model. The first mode indicates the scaling of shapes (Figure 2.14 (a)). Since the deformation of this mode is the shrinkage of all nodes towards the middle point of the shape, after the scale of a shape shrinks to zero, the orientation of the shape is inverted. The second mode indicates the rotation of shapes (Figure 2.14 (b)). The third mode indicates the variations in widths of tooth shapes (Figure 2.14 (c)). The fourth mode indicates the variations in the two ends of the shapes (Figure 2.14 (d)). The fifth mode indicates the shape variations in the tooth crowns (Figure 2.14



(a)



(b)



(c)

Figure 2.13. Shape Alignment. (a) correspondence between a prototype shape and a training shape; (b) correspondence between the prototype shape and the rotated training shape; (c) correspondence between the prototype shape and the scaled training shape.

(e)).

Shape Extraction

An algorithm for tooth contour extraction is given in Figure 2.15.

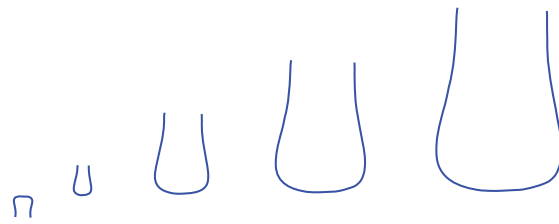
Algorithm: Tooth Contour Extraction

1. *Image Enhancement.* The input image is enhanced using the anisotropic diffusion to remove noise.
2. *Gradient Computation.* Salient edges in the enhanced images are detected using the Canny edge detector and a smoothed gradient field is computed based on the gradients of the detected edges.
3. *Shape Evolution.* The iterative procedure has the following steps:
 - (a) Initialize the current shape.
 - (b) Use ASMs to approximate the current shape.
 - (c) Search for optimal positions for all nodes in the model based on the current ASM-approximated shape.
 - (d) Replace the current shape with a smoothing spline, which connects detected optimal positions of the nodes.
 - (e) Repeat steps (b) to (d) five times to guarantee the convergence of shape evolution.
 - (f) Output the current shape.

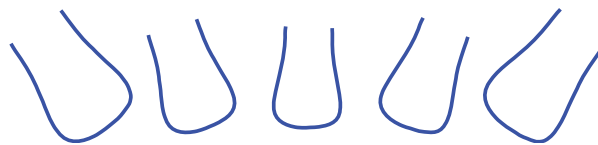
Details of each step are given below.

Image Enhancement

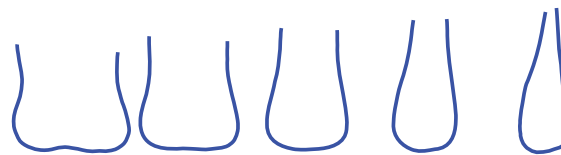
The input images are enhanced using the anisotropic diffusion algorithm, which is described in detail in Appendix B.



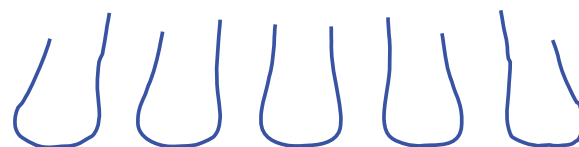
(a)



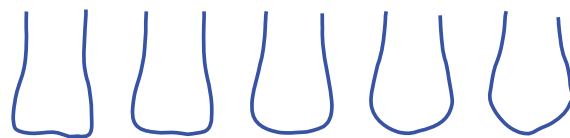
(b)



(c)



(d)



(e)

Figure 2.14. First five modes of the shape model of teeth. The middle shape in each row is the mean shape, while the other four shapes are, from left to right, mean shape plus four eigenvectors multiplied by -2 , -1 , 1 , and 2 times the square root of the corresponding eigenvalues.

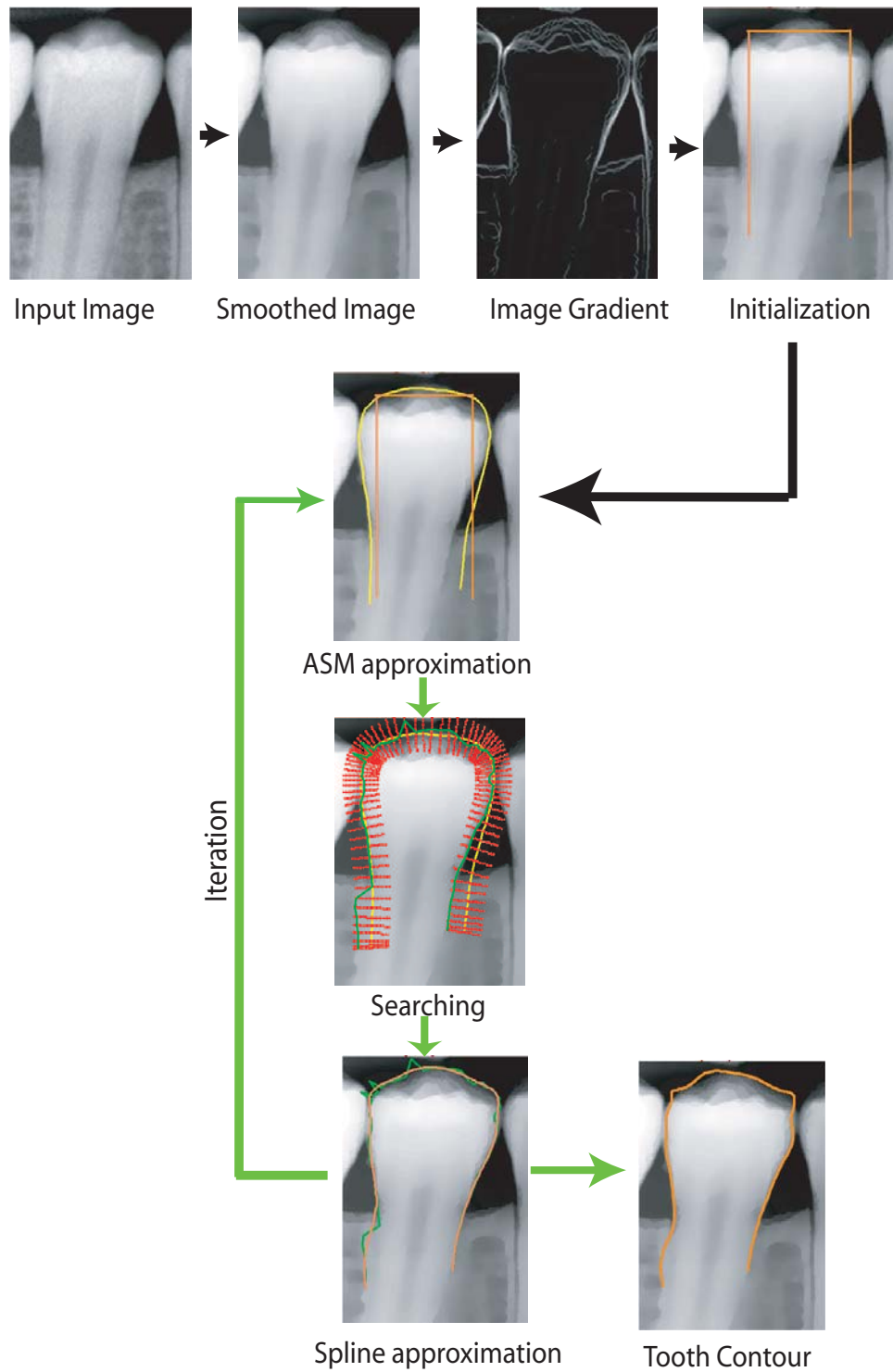


Figure 2.15. Shape extraction procedure.

Gradient Computation

We use a smoothed gradient field to guide the shape evolution. The smoothed gradient field is constructed in the following steps:

1. Edge Detection. The salient edges in the enhanced images are detected using the Canny edge detector.
2. Gradient Smoothing. A method inspired by Gradient Vector Field (GVF) [63] is used to construct the smoothed gradient field. Let the original gradient field be $(\mathbf{u}_0, \mathbf{v}_0)$, where for the edges detected in the previous step, \mathbf{u}_0 and \mathbf{v}_0 are the gradients in x and y directions, and for other pixels, \mathbf{u}_0 and \mathbf{v}_0 are zeros. Let \mathbf{u} and \mathbf{v} be the objective smooth gradient field that minimizes the energy E defined as follows:

$$E = \int \int \mu(\mathbf{u}_x^2 + \mathbf{u}_y^2 + \mathbf{v}_x^2 + \mathbf{v}_y^2) + (\mathbf{u}_0^2 + \mathbf{v}_0^2)((\mathbf{v} - \mathbf{v}_0)^2 + (\mathbf{u} - \mathbf{u}_0)^2) dx dy, \quad (2.11)$$

where μ controls the smoothness of the field, \mathbf{u}_x and \mathbf{u}_y are the gradients of \mathbf{u} in x and y directions, and \mathbf{v}_x and \mathbf{v}_y are the gradients of \mathbf{v} in x and y directions. The minimization procedure is the same as the GVF [63].

Shape Initialization

Given the ROI of the tooth, the tooth shape is initialized as the shape of 'n' (for lower row of teeth) or the shape of 'U' (for upper row of teeth) in the middle of the ROI (Figure 2.16). For the lower row of teeth, the width of the initialized shape is 1/3rd of the width of the ROI, and the height is the same as width of the ROI. The distance between the top of the shape and the top of the ROI is 1/8th of the width of the shape.

Approximate a Shape with ASM

Since shape rotation and scaling have been incorporated in the ASM model using the training techniques introduced in Section 2.3.2, the approximation procedure is simplified into a linear regression problem in vector space. To be robust with respect to noise in detected positions of boundary points, robust weighting is used [4]. The details of the approxima-

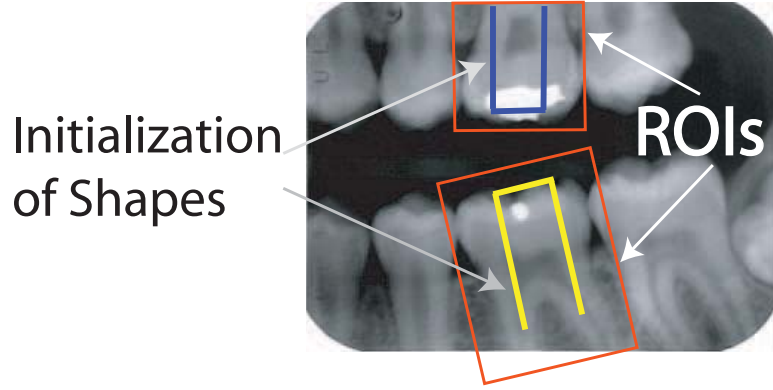


Figure 2.16. Initialization of tooth shapes.

tion algorithm are as follows. Let the shapes to be approximated be represented as a vector $\mathbf{V} = [x_1, x_2, \dots, x_n, y_1, y_2, \dots, y_n]^\top$. Let the mean shape of the trained ASM be denoted as $\mathbf{M} = [x_{1m}, x_{2m}, \dots, x_{nm}, y_{1m}, y_{2m}, \dots, y_{nm}]^\top$, and the eigenvectors of the trained ASM denoted as $\mathbf{e}_i, i = 1, 2, \dots, N - 1$, where N is the number of training shapes. Denote the number of eigenvectors used for shape extraction as k ($k = 10$ for tooth shape extraction since top-10 modes can explain 98% of variations in tooth shape [23]), the coefficient vector for those k eigenvectors as \mathbf{c} , and the translation as (x, y) . The objective function for shape approximation is defined as

$$\{\mathbf{c}, x, y\} = \arg \min_{\{\mathbf{c}, x, y\}} J, \quad (2.12)$$

where

$$\begin{aligned}
J &= \mathbf{L}^\top \mathbf{W} \mathbf{L}, \\
\mathbf{L} &= (\mathbf{M} + \mathbf{E} \cdot \mathbf{p}) - \mathbf{V}, \\
\mathbf{W} &= \text{diag}(\mathbf{w}), \\
\mathbf{E} &= [\mathbf{e}_1, \mathbf{e}_2, \dots, \mathbf{e}_k, \mathbf{e}_x, \mathbf{e}_y], \\
\mathbf{e}_x &= [\underbrace{1, \dots, 1}_{n \text{ 1's}}, \underbrace{0, \dots, 0}_{n \text{ 0's}}]^\top, \\
\mathbf{e}_y &= [\underbrace{0, \dots, 0}_{n \text{ 0's}}, \underbrace{1, \dots, 1}_{n \text{ 1's}}]^\top, \\
\mathbf{p} &= [\mathbf{c}^\top, x, y]^\top.
\end{aligned} \tag{2.13}$$

The weights \mathbf{w} are obtained using robust weighting [4], which is described as follows.

1. Calculate the residuals between the input shape and the appropriate shape obtained by using uniform weights.
2. Compute the robust weights for each point on the boundary. The weights are given by the bisquare function shown below.

$$w_i = \begin{cases} 1 - \left(\frac{r_i}{3 \cdot MAD}\right)^2, & \text{if } |r_i| < 3 \cdot MAD \\ 0, & \text{if } |r_i| \geq 3 \cdot MAD \end{cases}, \tag{2.14}$$

where r_i is the residual of the i th data point, and MAD is the median absolute value of the residuals:

$$MAD = \text{median}(|r|). \tag{2.15}$$

The median absolute value is a measure of how spread out the residuals are. If r_i is small compared to $3 \cdot MAD$, then the robust weight is close to 1. If r_i is greater than $3 \cdot MAD$, the robust weight is 0 and the associated data point is excluded from the

smoothness calculation.

3. Smooth the data again using the robust weights.
4. Repeat the previous two steps for five iterations.

To solve for the unknown parameters $\mathbf{p} = [\mathbf{c}^\top, x, y]^\top$ in equation (2.12), the derivative of J with respect to \mathbf{p} is set to be zero, i.e.,

$$\begin{aligned}
 \frac{\partial J}{\partial \mathbf{p}} &= \frac{\partial \mathbf{L}}{\partial \mathbf{p}} \frac{\partial J}{\partial \mathbf{L}} \\
 &= \mathbf{E}^\top \mathbf{W} \mathbf{L} \\
 &= \mathbf{E}^\top \mathbf{W} \cdot (\mathbf{M} + \mathbf{E} \cdot \mathbf{p} - \mathbf{V}) \\
 &= 0.
 \end{aligned} \tag{2.16}$$

So,

$$\mathbf{p} = (\mathbf{E}^\top \mathbf{W} \mathbf{E})^{-1} \cdot \mathbf{E}^\top \mathbf{W} \cdot (\mathbf{V} - \mathbf{M}). \tag{2.17}$$

Searching for Optimal Positions

To find the optimal position for each node in the model, the search range is the inside and outside $k/2$ ($k = 20$) points along the normal line at each node of the shape. The nodes in the model are classified into two types: crown nodes and root nodes (Figure 2.17). Different search strategies are used for the two types of nodes since boundaries of crowns and roots have different characteristics. The boundaries of crowns are located at the outermost gradients, while the boundaries of roots are located at the strongest gradients in the search range. Assume there are k points for the search. Denote the normal line direction of the node as \mathbf{n} , the gradient of the original image in the search scope as $\{\mathbf{g}_1, \mathbf{g}_2, \dots, \mathbf{g}_k\}$ and the smoothed gradient as $\{\mathbf{s}_1, \mathbf{s}_2, \dots, \mathbf{s}_k\}$. A metric for each point k in the search space

is defined as

$$M(k) = \begin{cases} \text{sign}(\mathbf{n} \cdot \mathbf{g}_k)(\mathbf{n}_x^2 \mathbf{g}_{k_x}^2 + \mathbf{n}_y^2 \mathbf{g}_{k_y}^2), & \text{if the node is a crown node,} \\ \text{sign}(\mathbf{n} \cdot \mathbf{s}_k)(\mathbf{n}_x^2 \mathbf{s}_{k_x}^2 + \mathbf{n}_y^2 \mathbf{s}_{k_y}^2), & \text{if the node is a root node,} \end{cases} \quad (2.18)$$

where \mathbf{n}_x and \mathbf{n}_y are x and y elements of the normal line direction \mathbf{n} , \mathbf{g}_{k_x} and \mathbf{g}_{k_y} are x and y elements of the gradient \mathbf{g}_k , and \mathbf{s}_{k_x} and \mathbf{s}_{k_y} are x and y elements of the smoothed gradient \mathbf{s}_k .

For crown nodes, the optimal position is the outermost point in the range which has a negative value of the metric $M(k)$. For root nodes, the optimal position is the point that has the most negative value of metric $M(k)$.

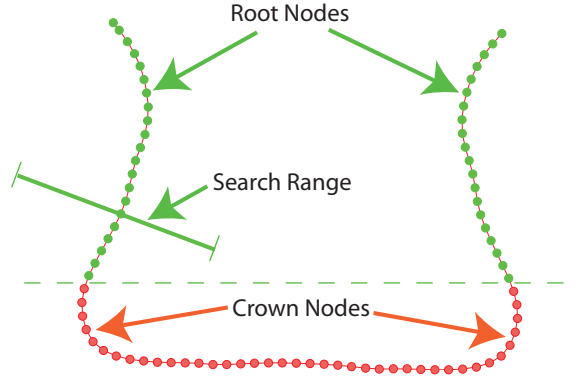


Figure 2.17. Crown nodes and root nodes in the model.

Smoothing Spline

The detected optimal positions of the nodes are connected using a smoothing spline s , which minimizes [5]

$$p \sum_{i=1}^n (\mathbf{y}_i - s(x_i))^2 + (1 - p) \int \left(\frac{d^2 s}{dx^2} \right)^2 dx, \quad (2.19)$$

where p is the smoothing factor, x_i is the index for the spline s , \mathbf{y}_i is the i th point to connect, and n is the number of boundary points in each training shape.

User Interaction

The automatic contour extraction algorithm may fail due to the poor image quality or improper initialization. The failure can be detected and a request can be issued for user interaction. The detection algorithm compares the coefficients, c , obtained in Equation (2.12) to the eigenvalues of the covariance matrix, Σ_x , in Equation (2.8). In particular, denote the eigenvalue of the i -th mode as v_i , $i = 1, 2, \dots, k$, where k is the number of eigenvectors used for shape extraction. Since eigenvalues represent the variances for a mode, if the absolute value of a coefficient, c_i , is larger than the square root of the eigenvalue, v_i , it may imply an aberrantly extracted shape and a warning message is issued. Figure 2.18 shows two examples of erroneous tooth contours detected by the algorithm. The check is not applied to the first two modes, since these modes represent scaling and rotation and, therefore, large coefficient values for these two modes do not imply aberrantly extracted shapes. The erroneous tooth contours are corrected by manually specifying points along the tooth contours.

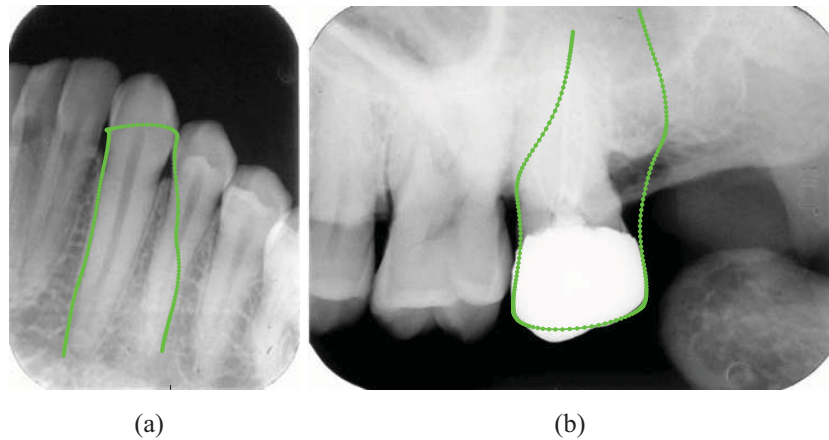


Figure 2.18. Detection of erroneous tooth contours.

2.3.3 Experiments

The tooth contour extraction routine (implemented in Matlab 7.0) takes ~ 15 seconds for a single tooth on a PC with a 2.99 GHz Pentium 4 processor. Experiments on 198

images containing a total of 1,284 teeth show that 59.4% of tooth contours were correctly extracted. For images of good quality, 76% of teeth were correctly extracted. The details of the accuracy are shown in table 2.2. Figure 2.19 shows some successfully extracted tooth shapes.

Table 2.2. Success Rate of Automatic Contour Extraction

Number of Extractions	Image Quality		
	Good	Medium	Poor
Successful	323	241	199
Failed	102	135	284

2.4 Segmenting Regions of Dental Work

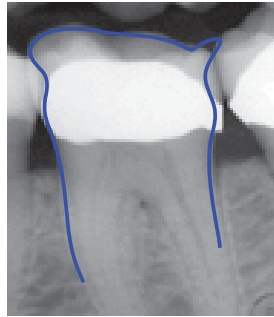
Another useful feature for matching AM and PM radiographs is the contours of dental work, if present, which appear as bright blocks in the radiograph (Figure 2.20 (a)). The most common dental work includes fillings and crowns, which are made of material such as silver amalgam, gold, stainless steel, CaOH base, and porcelain [31]. These materials are more radiopaque than the tooth enamel.

There are two steps for extracting the contours of dental work:

1. **Anisotropic Diffusion.** Anisotropic diffusion (see Appendix B) is used to enhance the image such that the boundaries of regions are preserved while the interiors of regions are smoothed. The number of iterations for enhancing dental work is eight, which has been determined empirically.

2. **Image Thresholding.** A mixture of Gaussians model is used to model the intensity histogram of the enhanced image. A threshold value is chosen to segment the dental work.

The details of the second step are given in the remainder of this section.



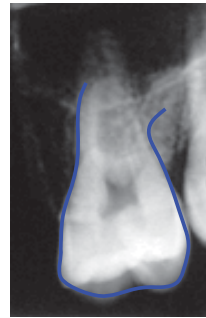
(a)



(b)



(c)



(d)



(e)



(f)

Figure 2.19. Tooth shapes successfully extracted using ASMs.

2.4.1 Image Thresholding

The extraction of dental work contours is accomplished using the intensity histogram of the radiographs. We fit a mixture of Gaussians to the intensity histograms. The Gaussian component with the largest mean corresponds to the pixel intensities associated with the dental work, while other components correspond to the pixel intensities belonging to the teeth. Dental work can be segmented using a threshold that best splits the Gaussian component with the largest mean from the other Gaussian components (See Figure 2.20) [34], [56]. Let the intensity histogram be denoted as $p(x)$. It is represented in terms of a mixture of $C + 1$ Gaussians as

$$p(x) = P_0 \cdot p_0(x) + \sum_{i=1}^C P_i \cdot p_i(x), \quad (2.20)$$

where $p_0(x)$ is the Gaussian component for the dental work and $p_i(x), i = 1, \dots, C$, are the C Gaussian components for the tooth pixels, P_0 and P_i 's are the mixing coefficients, and

$$p_i(x) = \frac{1}{\sqrt{2\pi}\sigma_i} \exp \frac{-(x - \mu_i)^2}{2\sigma_i^2}, i = 0, 1, \dots, C, \quad (2.21)$$

$$\mu_0 > \mu_i, i = 1, \dots, C, \quad (2.22)$$

$$\sum_{i=0}^C P_i = 1. \quad (2.23)$$

The number of components in the mixture, $(C + 1)$, can be estimated using the algorithm proposed by Figueiredo and Jain [29]. The method utilizes an expectation-maximization (EM) algorithm to select the number of components in a mixture model based on the minimum message length (MML) criterion.

Intuitively, if the variances of the Gaussians in the mixture decrease without changing the means, then misclassification error decreases as well, because there will be less overlap between the Gaussians. This objective is achieved by first enhancing the image with anisotropic diffusion. Figure 2.21 shows some input images ((a), (b), and (c)) compared with the smoothed images ((d), (e), and (f)) and the resulting contours of the tooth and the dental work. Small or narrow areas extracted in the images are regarded as artifacts and are

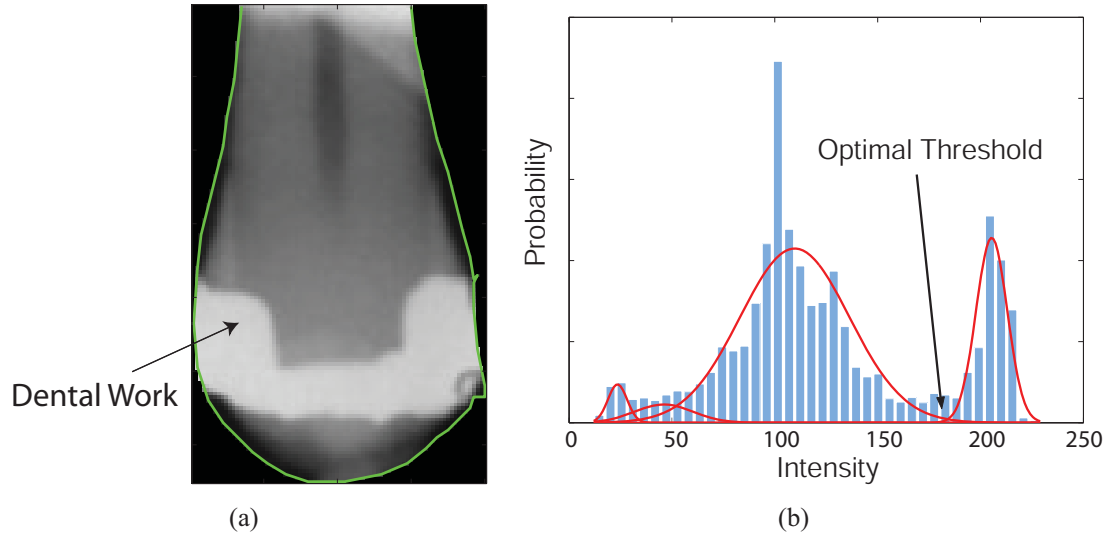


Figure 2.20. Fitting a mixture of Gaussians model to the intensity histogram (b) of an image (a), in which the dental work appears as a bright block.

removed. As can be seen, more accurate dental work contours are detected in smoothed images.

The process for extracting dental work contour for a single tooth takes ~ 10 seconds on a PC with a 2.99 GHz Pentium 4 processor. Experiments on 128 teeth images show that 90% of dental work contours are correctly extracted. The incorrectly retrieved contours are fixed by adjusting the parameters and number of iterations in the algorithm.

2.5 Summary

This chapter proposed methods for radiograph segmentation, extraction of tooth contours, and extraction of dental work contours. We proposed a method for segmenting dental radiographs based on fast marching algorithm. To correct the segmentation errors, an interactive method was developed. We also proposed an active shape model-based algorithm for extracting the contours of teeth. To extract dental work contours, an anisotropic diffusion-based technique was used to enhance the radiographs, and the regions of dental work were segmented using image thresholding. Segmenting a dental radiograph takes ~ 2.5 seconds,

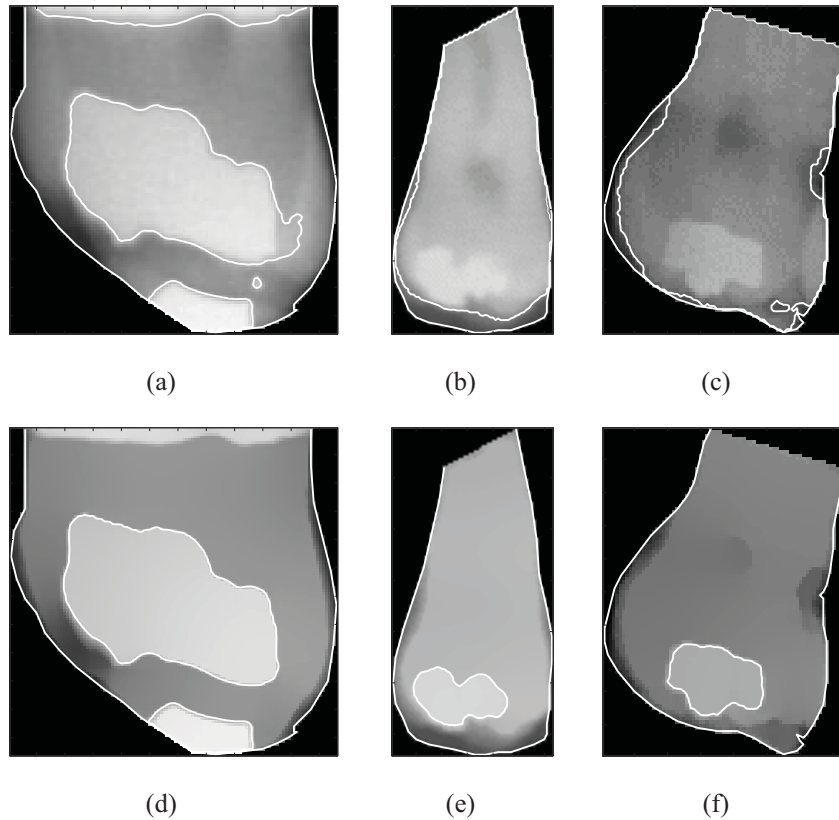


Figure 2.21. Extracted dental work contours with and without image enhancement. (a), (b) and (c) Without enhancement. (d), (e) and (f) After enhancement.

extracting tooth contours takes ~ 15 seconds for one tooth, and extracting dental work contours takes ~ 10 seconds for one tooth. These processes are evaluated on a PC with 2.99 GHz Pentium 4 processor. Table 2.3 summarizes the CPU time used in each step. Experiments have shown 61.1% accuracy for radiograph segmentation, 76% accuracy for tooth contour extraction (for images of good quality), and 90% accuracy for dental work contour extraction. An image quality evaluation function and monitoring scheme were developed to assess the image quality and correctness of results given by automatic algorithms. User interactions are requested when the image has poor quality or the results are incorrect. Figure 2.22 shows a process of extracting tooth contours and dental work contours with human interactions to correct detected errors.

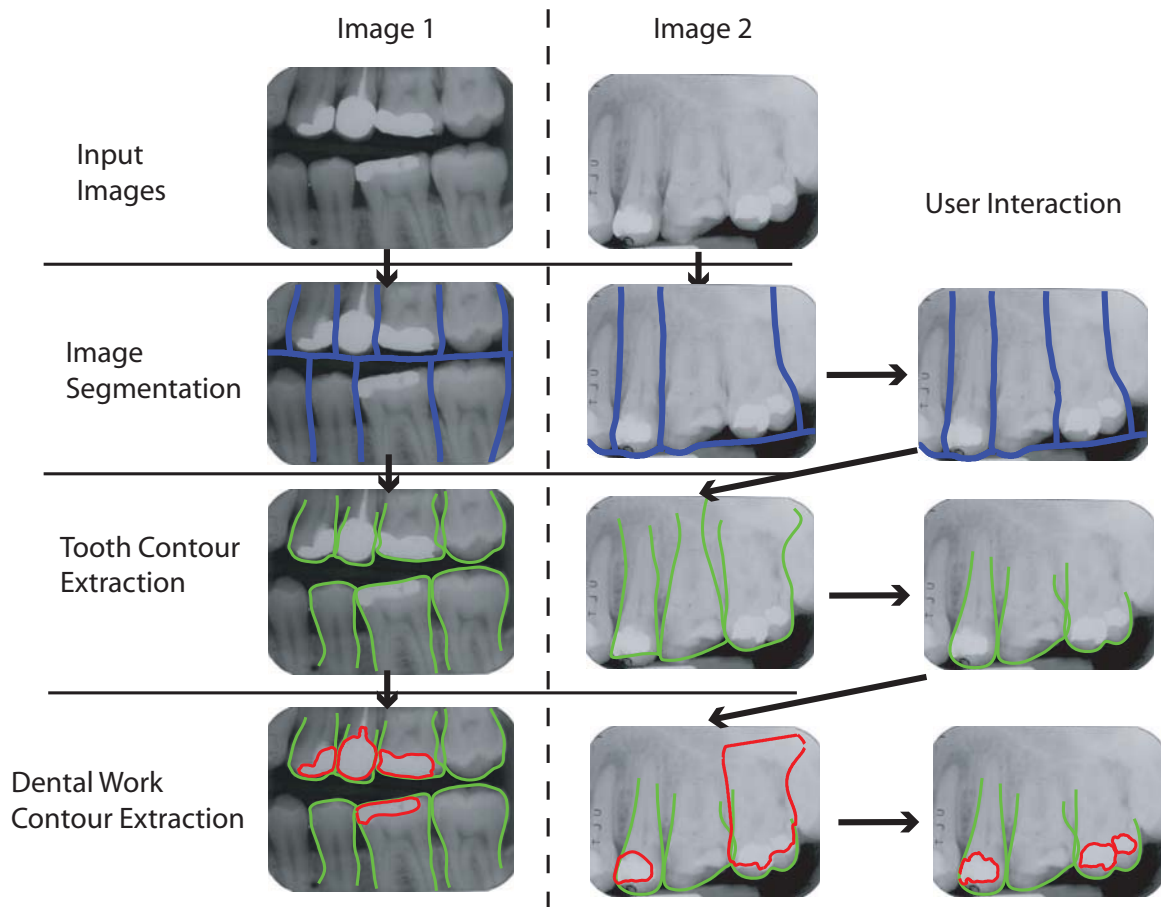


Figure 2.22. Process of extracting tooth contours and dental work contours with human interaction. Automatic method works well for the good quality image (image 1), but needs user interaction for poor quality image (image 2).

Table 2.3. Summary of CPU (2.99 GHz Pentium 4) Time for Extracting Features

Procedure	Time	Overall Time	Avg. Number of Calls
Radiograph Segmentation	2.5s	2.5s	1
Tooth Contour Extraction	15s	120s	8
Dental Work Extraction	10s	50s	5

CHAPTER 3

Registration of Radiographs to Dental

Atlas

One of the challenges in automatically matching dental radiographs is missing teeth in either the AM or PM image. In the presence of missing teeth, the matching algorithm will not be able to correctly align the tooth sequences in AM and PM images if it cannot determine which teeth are missing. However, missing teeth can be detected if the teeth in the images are first labeled based on dental anatomy. Anatomy-based tooth labeling can also accelerate the image matching stage, since a pair of PM-AM images need not be matched if no teeth share the same labels.

To label teeth with anatomical indices, dental radiographs are first registered to the human dental atlas, which is a descriptive model of the shapes and relative positions of teeth. We propose a hybrid model involving Support Vector Machines (SVMs) and a Hidden Markov Model (HMM) for representation of the dental atlas and classification of the teeth in dental radiographs.

3.1 Introduction

Mahoor and Abdel-Mottaleb [43] proposed a method to obtain the indices of teeth in bitewing images. After the tooth contours are extracted, Fourier descriptors, which are invariant to scaling, rotation and translation of the contours, are extracted from the sequence of contour coordinates. A Bayesian classifier is trained to classify the descriptor series into two categories: molars (M) and premolars or bicuspid (P). The tooth sequences without any missing teeth in the bitewing dental radiographs have only the following possible patterns: PM, PMM, PMMM, PPM, PPMM, and PPMMP for the left side image; MP, MMP, MMMP, MPP, MMPP, and MMMPP for the right side image, where “M” stands for molar, and “P” stands for premolar. Since the anatomical indices of teeth in each pattern are known, the indices of teeth in the radiographs can be determined after the pattern of the tooth sequence is identified. A major limitation of Mahoor and Abdel-Mottaleb’s method is that bitewing images are only one of the three types of dental radiographs, and bitewing images only include two classes of teeth: molars and premolars. Furthermore, this method assumes that there are no missing teeth in the images. When this assumption is not satisfied or classification errors between M and P types occur, the method results in false registrations. Experiments in [43] on 50 bitewing images show that the classification accuracy for molars in the lower row of teeth is 91.8%, the accuracy for molars in the upper row of teeth is 93.7%, the accuracy for premolars in the lower row of teeth is 82.0%, and the accuracy for premolars in the upper row of teeth is 91.4%.

Compared to Mahoor and Abdel-Mottaleb’s method, the method proposed here has the following advantages: it deals with all three types of dental radiographs (bitewing, periapical, and panoramic images (Figure 1.1)), and it considers all three classes of teeth (*molars*, *bicuspid*, and *incisors* (Figure 3.1)) [31]. The proposed method is a hybrid system involving the Support Vector Machine (SVM) and the Hidden Markov Model (HMM) for the representation and classification of teeth. The HMM serves as an underlying representation of the dental atlas by representing various teeth and the distances between the neighboring

teeth as HMM states. The SVM classifies the teeth into 3 classes based on their contours. Missing teeth in a radiograph can be detected by registering the observed tooth shapes and the distances between adjacent teeth to the dental atlas. Furthermore, instead of simply assigning a class label to each tooth, the posterior class probability associated with each tooth is extracted from the SVM and passed to the HMM. This approach reduces the impact of classification errors during registration. The hybrid model yields the probability of registering the tooth sequences in a radiograph to their possible positions in the atlas. The top- n ($n=3$) possible registrations are explored further in the radiograph matching stage.

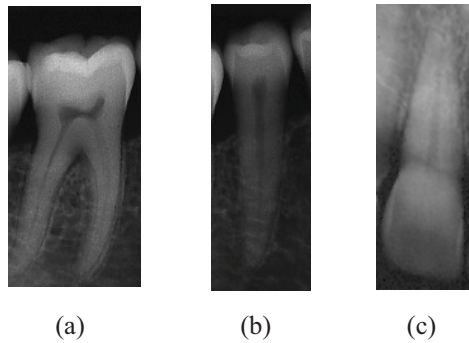


Figure 3.1. Three types of teeth. (a) Molar; (b) (bi)cuspid; (c) incisor.

In this chapter, the SVM/HMM model is described in section 3.2, and the representation of the dental atlas using the SVM/HMM model is discussed in section 3.3. Section 3.4 introduces a method for detecting incorrect estimations of tooth indices. Section 3.5 presents experimental results of applying the algorithm to a database of dental radiographs.

3.2 SVM / HMM Hybrid Model

Hybrid models of SVMs and HMMs have been utilized for sequential data analysis. Ganapathiraju et al. [30] used a SVM prior to a HMM for speech recognition. Castellani et al. [17] used the same structure for analysis and segmentation of teleoperation tasks. Campbell [16] applied a HMM before the SVM for speaker recognition. Our system utilizes SVM for classification of teeth and HMM for registering a tooth sequence to the dental atlas using

the classification results. By integrating SVM and HMM, the classification results passed from the SVM to the HMM are posterior class probabilities instead of classification labels. This reduces the impact of erroneous SVM classifications on registration.

A hybrid SVM/HMM system is used to model a sequence of events. The goal is to estimate $P(E, Q)$, the probability of observing a sequence of events $E = \{e_1, e_2, \dots, e_L\}$ from a sequence of states $Q = \{q_1, q_2, \dots, q_L\}$ in the model. Q is called a *path* in the following text. For a given event sequence E , the top- n registrations are retrieved by comparing $P(E, Q)$ for all possible Q 's. The SVM/HMM system is denoted as $\lambda = \{S, A, V, B, \pi\}$, where the definitions of the elements are as follows:

- $S = \{S_1, S_2, \dots, S_N\}$ denotes the set of N states;
- $A = \{a_{ij}\}$ is the $N \times N$ transition matrix, which represents the probability of transitioning from state S_i to state S_j .

$$a_{ij} = P(q_{t+1} = S_j | q_t = S_i), \quad (3.1)$$

where $1 \leq i, j \leq N$, $1 \leq t \leq L - 1$, $a_{ij} \geq 0$ and for all i , $\sum_{j=1}^N a_{ij} = 1$;

- $V = \{v_1, v_2, \dots, v_M\}$ is a set of M observation classes;
- $B = \{b_{jk}\}$ is an $M \times N$ emission matrix, indicating the probability of observing an instance of class k at state j , i.e.,

$$b_{jk} = P(v_k | S_j); \quad (3.2)$$

- $\pi = \{\pi_i\}$ is the set of N initial state probabilities, representing the probabilities of starting a sequence from every state, i.e.,

$$\pi_i = P(q_1 = S_i). \quad (3.3)$$

Given an event sequence $E = \{e_1, e_2, \dots, e_L\}$ and a path $Q = \{q_1, q_2, \dots, q_L\}$, the

probability $P(E, Q)$ evaluated by the model λ is defined as

$$P(E, Q) = P(E|Q)P(Q), \quad (3.4)$$

$$P(Q) = P(q_1) \prod_{i=2}^L P(q_i|q_{i-1}). \quad (3.5)$$

$$P(E|Q) = \prod_{i=1}^L P(e_i|q_i) \quad (3.6)$$

$$= \prod_{i=1}^L \sum_{k=1}^M p(e_i|v_k, q_i) P(v_k|q_i). \quad (3.7)$$

Since the shape of a tooth depends more on its type than on its position, let us assume that $p(e_i|v_k, q_i)$ is independent of the state q_i , i.e., $p(e_i|v_k, q_i) = p(e_i|v_k)$. Then, according to the Bayes rule,

$$p(e_i|v_k) = \frac{p(v_k|e_i)P(e_i)}{P(v_k)}. \quad (3.8)$$

Now equation (3.7) can be written as

$$P(E|Q) = \prod_{i=1}^L \sum_{k=1}^M \frac{p(v_k|e_i)P(e_i)}{P(v_k)} P(v_k|q_i), \quad (3.9)$$

$$\propto \prod_{i=1}^L \sum_{k=1}^M \frac{p(v_k|e_i)}{P(v_k)} P(v_k|q_i), \quad (3.10)$$

where the posterior probability $p(v_k|e_i)$ is extracted from the SVM, and $P(e_i)$ is the constant of proportionality, which does not impact the comparison of $P(E, Q)$'s. $P(v_k)$ is derived from the training data, and $P(v_k|q_i)$ is given by the emission matrix B . In Equation (3.5), $P(q_1)$ is given by the initial state probabilities π , and $P(q_i|q_{i-1})$ is given by the transition matrix A .

Traditional SVMs solve two-class classification problems, and they do not provide posterior class probabilities. To solve multi-class classification problems, a strategy of one-versus-one or a strategy of one-versus-all is used [50]. If there are M classes, $M(M-1)/2$ SVMs are needed for the one-versus-one strategy, as compared to M SVMs for the strategy of one-versus-all. Experiments on a number of standard classification tasks have shown

that one-versus-one classifiers are marginally more accurate than one-versus-all classifiers [10]. Therefore, our system uses the strategy of one-versus-one.

The extraction of posterior class probabilities from a group of one-versus-one SVMs involves two steps. We first estimate *pairwise posterior probabilities* from each one-versus-one classifier. The pairwise posterior probability is defined as

$$r_{kl} = p(v = k|e, v = k \text{ or } l), \quad (3.11)$$

where k and l are the class labels, and $p(v = k|e, v = k \text{ or } l)$ is extracted using the formula

$$p(v = k|e, v = k \text{ or } l) = \frac{1}{1 + e^{Af(e)+B}}, \quad (3.12)$$

where e is the input to SVM, $f(e)$ is the output score of SVM, and A and B are estimated using a model-trust minimization algorithm under cross-validation [50]. The global posterior probability for class k is denoted as p_k , where

$$p_k = p(v_k|e) = p(v = k|e), k = 1, \dots, M. \quad (3.13)$$

The global posterior probability, p_k , is estimated from all the r_{kl} 's by solving the following optimization problem [62]:

$$\begin{aligned} \min_{p_1, \dots, p_M} \frac{1}{2} \sum_{k=1}^M \sum_{l=1, l \neq k}^M (r_{lk}p_k - r_{kl}p_l)^2, \\ \text{subject to} \end{aligned} \quad (3.14)$$

$$\sum_{k=1}^M p_k = 1, p_k \geq 0, \forall k.$$

3.3 Registering a Tooth Sequence to Dental Atlas

The SVM/HMM model is used to represent the dental atlas, and the observation sequences are extracted from the dental radiographs and registered to the dental atlas to find the anatomical labels (molar, (bi)cuspid and incisor) of the teeth.

3.3.1 Representation of Dental Atlas

The dental atlas of a complete set of adult teeth is shown in Figure 3.2. The teeth are classified into three categories according to their appearances: molars, (bi)cuspid, and incisors.¹ Molars have 2 or 3 roots and 3 or 4 cusps in their crowns. Cuspids and bicuspid have 1 or 2 cusps and 1 to 3 roots. Usually only one of the roots is visible in the radiographs. Incisors have flat crowns compared to other types of teeth, and each incisor has a single root. According to the universal nomenclature system [9], tooth indexing starts from the rightmost upper molar to the leftmost upper molar, and resumes from the leftmost lower molar to the rightmost lower molar. Using SVM/HMM model, upper and lower teeth are modeled separately. A SVM/HMM model representing the 16 upper teeth is illustrated in Figure 3.3. For each tooth in the dental atlas, there is a *tooth state* representing the observed tooth in that position, as well as three *distance states* representing the number of missing teeth (0, 1, or 2) after this position. The tooth states are shown as circles, and the number inside each circle is the tooth index. The squares in the model are distance states, and the number inside the square is the number of missing teeth. Here we assume there are at most 2 consecutive missing teeth. For the 16 lower teeth, the model has the same structure as the model shown in Figure 3.3, except that the tooth indices now go from 32 down to 17. Since an observation sequence can start from any tooth state, the initial state probabilities for the tooth states in the model are the same, i.e., $P(q) = 1/16$ for each row of teeth, where q is any one of the 16 tooth states in the model. The teeth are not classified with respect to their indices by SVMs due to the fact that the small inter-category variability poses difficulty for classification.

¹Bicuspid and cuspid are sometimes regarded as two different classes. Here we use “(bi)cuspid” to refer to both bicuspid and cuspid as one class due to their similar appearances in dental radiographs.

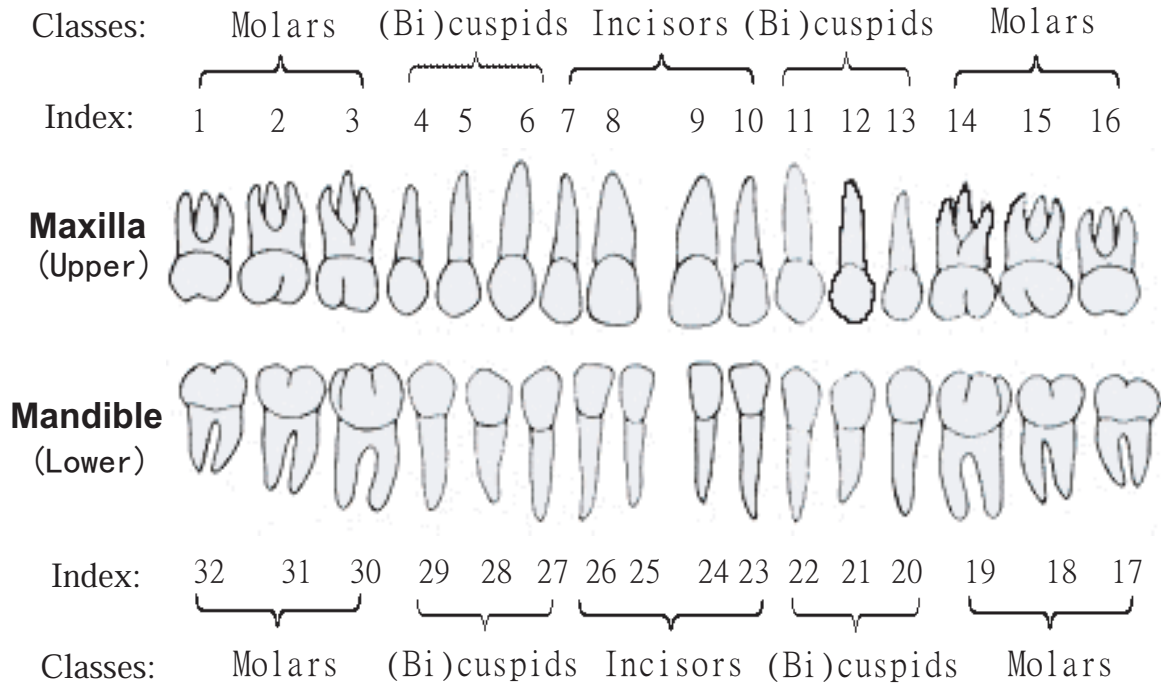


Figure 3.2. Dental Atlas of a complete set of adult teeth containing indices and classification labels of the teeth.

3.3.2 Extraction of Observation Sequences

The model structure in Figure 3.3 shows that a feasible path is an alternating sequence of tooth states and distance states. The observation for a path is accordingly an alternating sequence of observations for tooth states and for distance states; Figure 3.4 shows the procedure for generating an observation sequence. The observation for a tooth state is the contour of the tooth (methods for extracting the tooth contours are discussed in Chapter 2 (See Figure 3.4)). Tooth contours are then normalized into equal-length vectors as the input to the SVM. The observation for a distance state is the distance between the neighboring teeth. To eliminate the inconsistency caused by different resolutions used in radiograph digitization, each distance is divided by the width of its preceding tooth.

The teeth belong to one of three classes: molars, (bi)cupids, or incisors. For a tooth-contour vector e_i , the SVM generates the posterior class probabilities $p(v_k|e_i)$, $v_k \in \{\text{molar, (bi)cupids, incisor}\}$. For a distance state q_j and an observed distance e_j , a trained

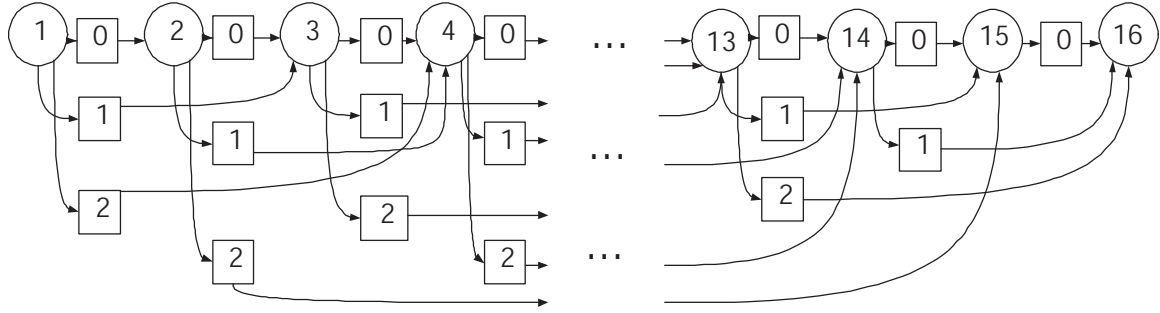


Figure 3.3. SVM/HMM model for the upper row of 16 teeth.

mixture of Gaussians model generates the probability $p(e_j|q_j)$ in Equation (3.6). By comparing $P(E, Q)$'s given by Equation (3.4), we retrieve the top- n possible paths. The indices of the teeth in the observation sequence are obtained from the tooth states in the path.

3.4 User Interaction

Detection of incorrect estimation of tooth indices makes it possible for users to interactively correct the errors. The estimation errors result from untypical shapes of teeth. Given an untypical shape, SVMs produce similar posterior probabilities for the three classes. A probability-based error detection algorithm is proposed based on this phenomenon. The detection rule is: if the difference between the probabilities of top-2 estimations is less than 0.2, the estimated tooth indices may be incorrect. The incorrect estimation can be corrected by manually assigning the tooth indices to the teeth. Figure 3.5 shows the user interface for manually specifying tooth indices.

3.5 Experimental Results

The algorithm was evaluated on the database mentioned in Chapter 1. A total of 1,702 tooth contours associated with 33 subjects were extracted from the radiographs in the database with the contour extraction methods, proposed in Chapter 2. Experiments were conducted

on the extracted tooth contours before and after user interaction.

There are 676 tooth sequences in the database, and the 33 subjects were separated into 3 folds of approximately equal-size. One fold was used for training the SVM, the second fold was used for training the HMM, and the third fold was used for testing the registration algorithm. We used the 3-fold cross-validation, so all the tooth sequences were registered to the dental atlas after three executions of the routine. The implementation of the SVM used in the experiments was LibSVM². The confidence measure for each estimate of the tooth indices in a tooth sequence is evaluated in the SVM/HMM model as the probability of registering the tooth sequence to the corresponding states in the atlas. The estimates of the tooth indices were ranked with respect to the confidence measures. For fully automatically extracted tooth contours, the accuracy for top-1 estimation is 60.1%, the accuracy for top-2 estimations is 72%, and the accuracy for top-3 estimations is 75%. For extracted tooth contours with the help of user interaction, accuracy using top-1 estimation increases to 85.1%, accuracy using top-2 estimations is 91.1%, and accuracy using top-3 estimations is 92.6%. The top-3 estimations will be used in the matching process discussed in Chapter 4 since there is no increase in the accuracy by using top-4 estimations compared to top-3 estimations. The training process takes 0.18s for each sequence (consisting of 2.5 teeth on average), and the registration process takes 0.17s for each sequence on a PC with a 2.99 GHz Pentium 4 processor.

Figure 3.6 shows some instances of successful atlas registrations, while Figure 3.7 shows some instances of atlas registration errors. The errors in atlas registration are caused due to three main sources: (i) Insufficient length of tooth sequences. For example, a sequence of 2 consecutive lower molars can be registered to positions 30 and 31, or 31 and 32, or 17 and 18, or 18 and 19 with equal probabilities, though only one of the four estimates is true (Figure 3.7(a)). (ii) Tooth classification errors in short sequences, for which the lengths of the sequence are not sufficient to compensate for the tooth misclassifications.

²LibSVM can be downloaded at (<http://www.csie.ntu.edu.tw/~cjlin/libsvm/>)

In other words, a classification error in a 16-tooth sequence is easier to correct than an error in a 4-tooth sequence (Figure 3.7(b)). (iii) Errors in detection of missing teeth, because the remaining teeth slide together and nearly fill the gap caused by the missing teeth (Figure 3.7(c)). Table 3.1 shows the accuracies of estimating tooth indices and the percentage of errors caused by each of the three factors in the top-3 estimations.

Table 3.1. Accuracies and Sources of Error in Estimating Tooth Indices

Rank of Registration	Accurate Estimation	Sources of Error		
		Factor (i)	Factor (ii)	Factor (iii)
Top-1	85.1%	8.1%	5.6%	1.2%
Top-2	91.1%	4.3%	3.6%	1.0%
Top-3	92.6%	3.6%	3.1%	0.7%

3.6 Summary

This chapter discussed a scheme for registering dental radiographs to the dental atlas. The method utilizes a SVM/HMM model to represent the dental atlas and classify teeth in the radiographs. Tooth indices are determined by registering the tooth sequence in the radiograph to the dental atlas. The system generates probabilities for each registration of the tooth sequence. Experiments were conducted on a database of 676 tooth sequences. For tooth contours that were not corrected by the user, the accuracy for top-1 estimation is 60.1%, the accuracy for top-2 estimations is 72%, and the accuracy for top-3 estimations is 75%. For user corrected tooth contours, accuracy using top-1 estimation is 85.1%, accuracy using top-2 estimations is 91.1%, and accuracy using top-3 estimations is 92.6%. On average, training of the proposed SVM/HMM model takes 0.18s for each sequence, and estimation of tooth indices takes 0.17s for each sequence on a PC with a 2.99 GHz Pentium 4 processor.

The proposed method fails when tooth sequences do not have sufficient number of teeth for correct registration, the tooth types are misclassified, or teeth slide together after tooth extraction. We have developed an error detection algorithm and a graphical user interface

(GUI) to interactively correct the estimation errors.

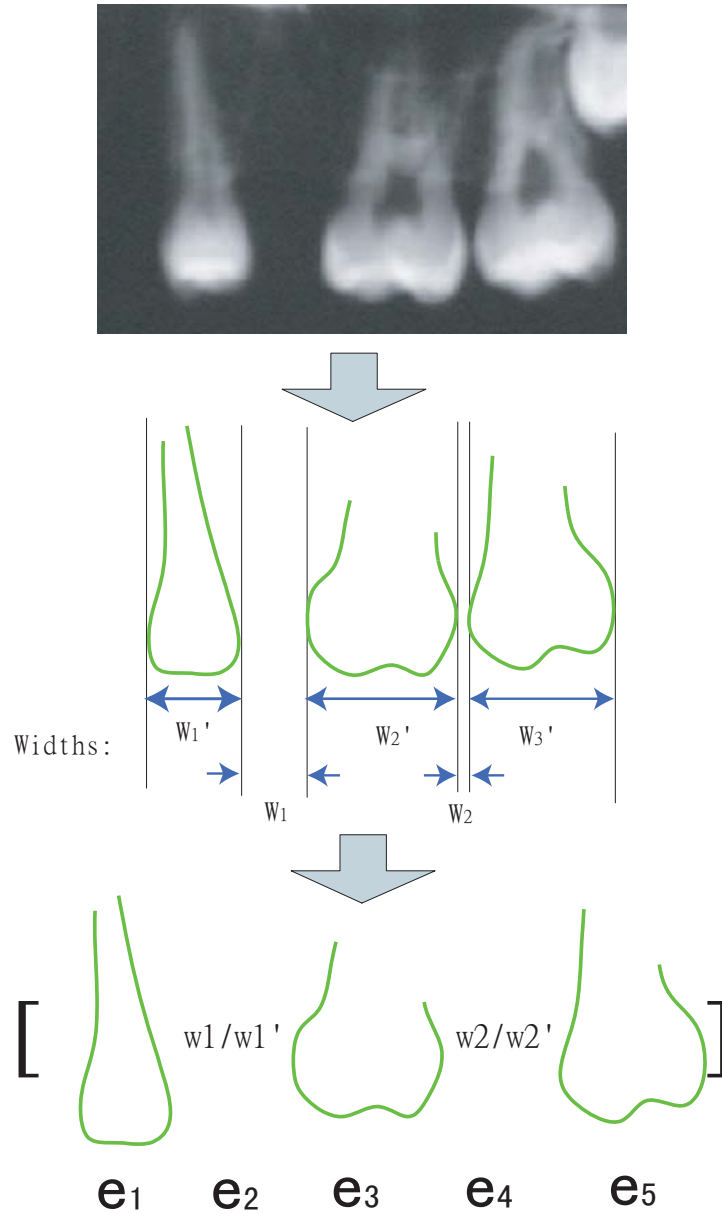


Figure 3.4. Extraction of tooth contours and generation of an observation sequence, $E = \{e_1, e_2, e_3, e_4, e_5\}$; e_1 , e_3 and e_5 correspond to tooth states, and e_2 and e_4 correspond to distance states.

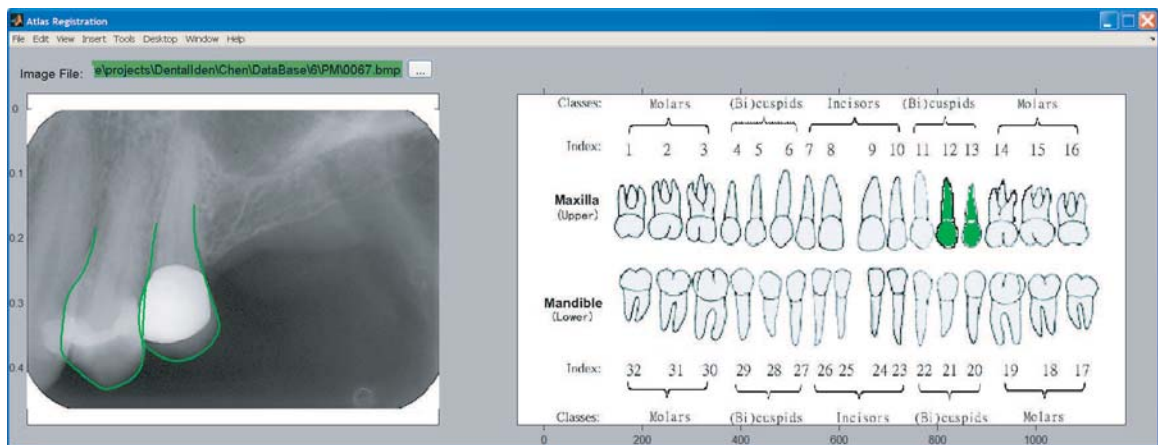


Figure 3.5. A user interface for manually specifying tooth indices by clicking the corresponding teeth in the dental atlas, which is shown on the right side of the dental radiograph.

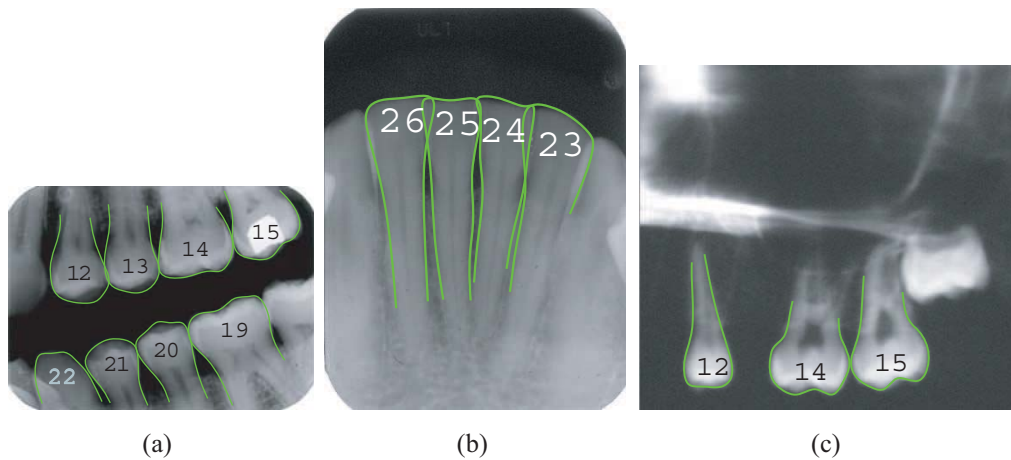


Figure 3.6. Examples of successful registration of the dental atlas to (a) a bitewing image, (b) a periapical image, and (c) an image with a missing tooth. In (c), teeth numbered as 12, 14, and 15 are correctly registered. The missing tooth (number 13) is detected.

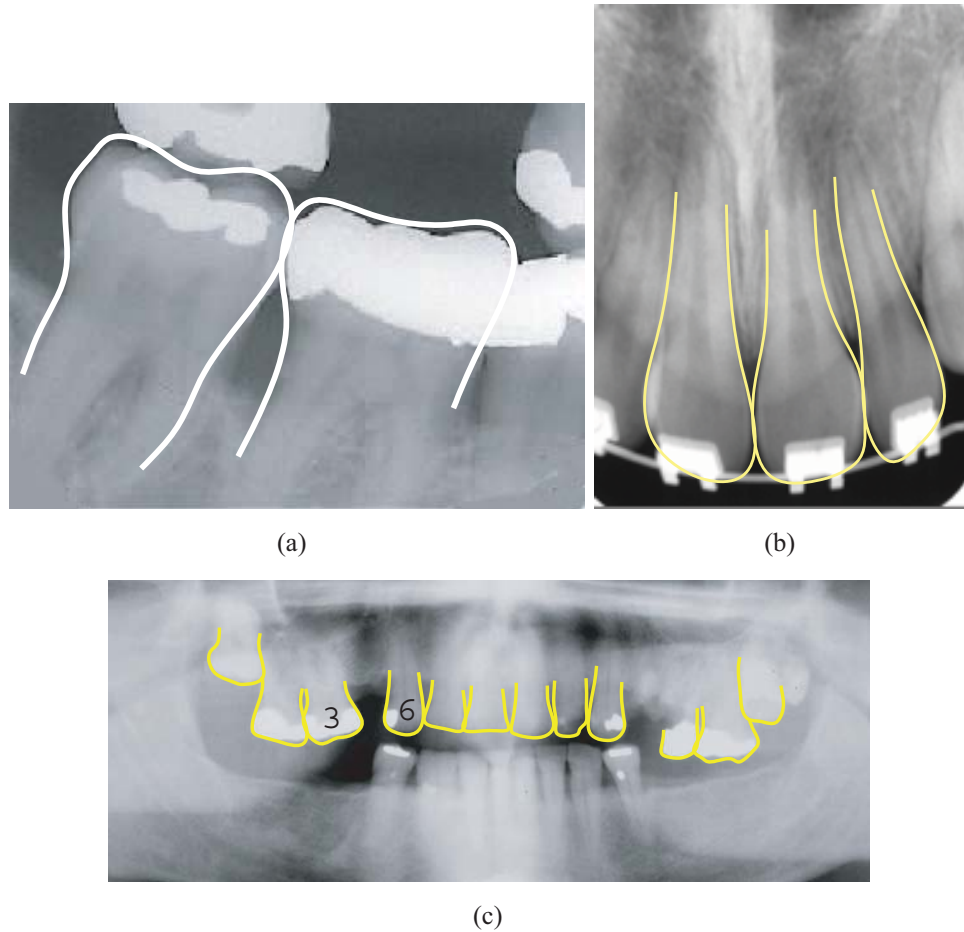


Figure 3.7. Examples of atlas registration errors. (a) The tooth types are correctly classified as molars, but the teeth (with genuine indices 30 and 31) are registered to teeth 31 and 32 in the atlas since teeth 30, 31, and 32 are all molars and the length of the sequence is insufficient for resolving the ambiguity; (b) all the three incisors are classified as (bi)cuspid, thus these teeth (with genuine indices 8, 9, and 10) are registered to teeth 3, 4, and 5 in the atlas; (c) the distance between teeth 3 and 6 seems to support only one missing tooth, so the input sequence is registered to the atlas teeth numbered 1, 2, 3, 5, 6, 7, 8, 9, 10, 12, 13, and 14, while the genuine indices are 1, 2, 3, 6, 7, 8, 9, 10, 11, 13, 14, and 15. The lower row of teeth is, however, correctly registered to the atlas.

CHAPTER 4

Matching and Retrieval

The final stage of the identification system is to match dental radiographs of unidentified subjects against dental radiographs of subjects in the database. Tooth-wise matching is executed first to match tooth contours of every pair of teeth. When dental work is present in both teeth, the shapes of dental work are also matched. An overall matching distance for a pair of teeth is generated by fusing the matching distances for the tooth contours and the dental work via posterior probabilities. A method using the results of tooth index estimation is proposed for computing the distances between the given unidentified subject and all database subjects. The database subjects are then sorted in ascending order of the matching distances and presented to forensic experts for final analysis.

4.1 Radiograph Matching

This section discusses the process of matching dental radiographs using tooth contours and regions of dental work.

4.1.1 Introduction to Shape Matching

In terms of the dimensionality of shapes, shape matching tasks can be categorized into 2D shape matching and 3D shape matching. Tooth and dental work contours are 2D shapes, therefore this chapter only discusses 2D shape matching. 2D shape matching can be classified according to the closeness/openness of the contours, where the difference is the ease or difficulty of establishing correspondences. When matching closed contours, every point in one contour must correspond to a point in the counterpart contour. This assumption is not satisfied when matching open contours, where some sections of one contour may not have corresponding sections in the counterpart contour. Matching closed contours is generally easier than matching open contours, since the overlapping sections of the two open contours need to be detected before alignment.

Matching closed shapes is a well-studied problem. Closed-shape matching algorithms are classified into two classes: *contour-based* methods and *region-based* methods [65]. The features used for contour-based matching are extracted from the contours, while the features used for region-based matching are extracted from the entire shape. Each class can be further divided into *global* methods and *structural* methods. For the global methods, features are extracted from the entire contour, e.g., the Fourier descriptor, while the structural methods match shapes using contour primitives (segments/sections), such as chain codes. Based on whether the features are extracted in the spatial domain or the transformed domain, the methods can also be categorized into *space domain* methods and *transform domain* methods. Zhang et al. provide a taxonomy of closed shape matching methods in [65] (see Figure 4.1).

The main challenge for the open shape matching task is to establish the correspondence. Since it is generally more difficult to establish correspondence between regions than between contours, open shapes are generally matched based on contours, instead of regions. Since the shape correspondence is unknown, global representations of shapes are not appropriate because they cannot be used to explicitly establish correspondences.

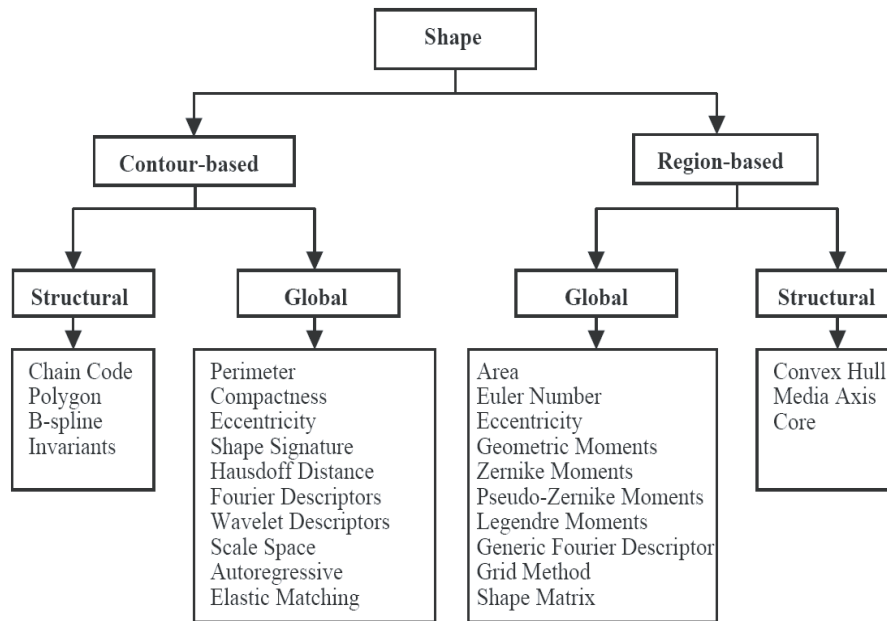


Figure 4.1. Classification of shape matching methods [65].

A solution to the open shape matching problems is to convert them into point matching problems. As noted by Gold et al. [32], to solve a point matching problem, one has to search in two complimentary spaces: the space of correspondence functions (e.g., finding correspondence with respect to shape context [12] and sharpness of corners [38]), and the space of similarity transformations (e.g., thin-plate splines [15] or ICP [13]). Point matching problems can be solved either by minimizing an energy function that incorporates transformation and matching metrics, such as Gold et al.'s *softassign* algorithm [32] [22], or by sequentially and iteratively finding the point correspondence and optimizing the transformation between the two shapes.

The tooth contours we extract from the dental radiographs are open contours, while the contours of the dental work are closed contours. The methods for matching these features are presented in the following sections.

4.1.2 Matching Tooth Contours

Given two tooth contours A and B , the problem of matching A and B is to find a transformation T between a segment of A , denoted as $A'(t)$ ($t \in [0, 1]$) and a segment of B , denoted as $B'(t)$ ($t \in [0, 1]$), such that

$$\{T, A', B'\} = \arg \min_{\{T, A', B'\}} \int_0^1 \|A'(t) - B'(t)\| dt, \quad (4.1)$$

where $\|\cdot\|$ is the Euclidean distance between two points. The algorithm for solving this problem in a discrete fashion is outlined here, followed by more detailed explanations in the remainder of this section.

Algorithm: Matching Tooth Contours

Input: two shape instances A and B in the form of spline curves.

1. *Polygonal approximation*: Approximate shape A and shape B with point sets AP and BP . In order to find the correspondence from shape A to shape B , the sampling rate for B should be higher than the sampling rate for A so that BP can approximate B precisely enough for distance computation.
2. *Shape registration*: If the applied transformation from AP to BP is T , then find the correspondence from $T(AP)$ to BP that preserves the topologies of the two curves.
3. *Distance computation*: Compute the distance between $T(AP)$ and BP on the basis of their correspondence. Denote the distance as $D(T(AP), BP)$.
4. *Optimization*: Optimize $D(T(AP), BP)$ in the space of transformations and correspondences by repeating steps 2 and 3 until the value of $D(\cdot, \cdot)$ converges or the maximum number of iterations is reached.

Polygonal Approximation

The polygonal approximation of tooth contours converts the shape matching problem into a point matching problem. There are many methods for approximating curves with polygonal

lines [28] [49] [60]. We use arc length parametrization to generate equally spaced points along curves [49] [60], so that the overall distance between two curves will not be biased by some portions of the curve that are more densely sampled than other portions.

Let \mathbf{Q} be a spline curve with m control points. Using Lee's centripetal scheme [42], the m control points are represented with $4(m + 1)$ coefficients, denoted as \mathbf{c}_{ji} , $i = 1, 2, 3, 4, j = 0, \dots, m$ and m control values, v_1, \dots, v_m . The cubic spline representation of the j th ($j = 0, \dots, m$) piece of \mathbf{Q} is formulated as:

$$\mathbf{Q}_j(u) = \sum_{i=1}^4 (u - v_j)^{4-i} \mathbf{c}_{ji}. \quad (4.2)$$

Define δ as an index into \mathbf{Q} 's knot vector, i.e., \bar{u}_δ occurs before $\bar{u}_{\delta+1}$, $\bar{u}_\delta < \bar{u}_{\delta+1}$. Given a control value u , $\bar{u}_0 \leq u \leq \bar{u}_m$, the arc length of the curve from u_0 to u is:

$$L(u) = \sum_{\substack{\delta < \alpha \\ \text{for all } \delta}} \int_{\bar{u}_\delta}^{\bar{u}_{\delta+1}} \|\mathbf{Q}'(u)\| du + \int_{\bar{u}_\alpha}^u \|\mathbf{Q}'(u)\| du, \quad (4.3)$$

where α is the largest index satisfying the condition that $\bar{u}_\alpha < u$.

Since $L(u)$ is a monotonically non-decreasing function, the inverse function $L^{-1}(\cdot)$ exists and we can calculate u for a given arc length a as $u = L^{-1}(a)$. So $\mathbf{Q}(L^{-1}(a))$ is the point at distance a from the starting point of the curve. When a increases evenly, the extracted points have equal distances along the curve.

The process for obtaining \mathbf{Q} 's polygonal approximation QP is summarized as follows:

1. Curve length computation: Use Equation (4.3) to get the length of the curve, $L(\bar{u}_m)$, where \bar{u}_m is the largest control value of the spline.
2. Selection of control values: Given interval arc length l , generate an array a_i , $i = 0, \dots, \lfloor L(\bar{u}_m)/l \rfloor$, such that $a_0 = 0$ and $a_{i+1} - a_i = l$. The corresponding array p_i , $i = 0, \dots, \lfloor L(\bar{u}_m)/l \rfloor$ is obtained as $p_i = L^{-1}(a_i)$.
3. Point generation: Use p_i , $i = 0, \dots, \lfloor L(\bar{u}_m)/l \rfloor$, as the parameter in Equation (4.2) to obtain the i th point in QP .

Figure 4.2 shows polygonal approximations of a tooth contour with different interval

arc lengths. In our experiments, we use interval arc length $l = 10$ for approximating query shapes, and $l = 5$ for approximating database shapes.

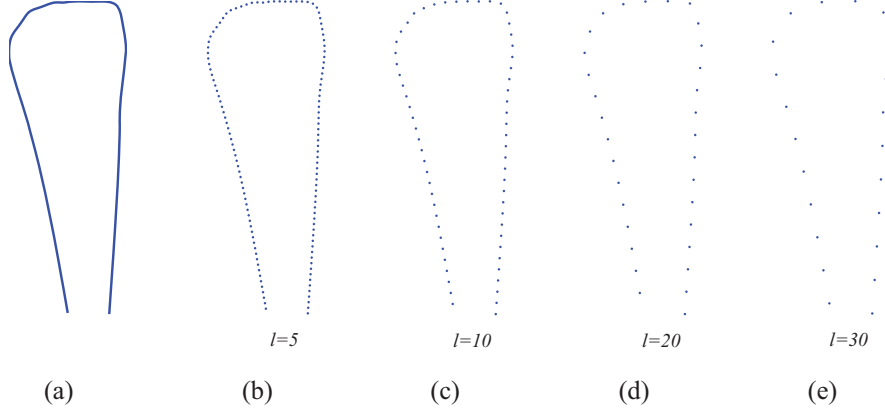


Figure 4.2. Polygonal approximation of a tooth contour with different interval arc lengths. (a) Original tooth contour; (b) polygonal approximation of (a) with interval arc length $l = 5$ pixels; (c) polygonal approximation of (a) with interval arc length $l = 10$ pixels; (d) polygonal approximation of (a) with interval arc length $l = 20$ pixels; (e) polygonal approximation of (a) with interval arc length $l = 30$ pixels.

Transformation

The dental radiographs are projections of 3D structures (teeth) onto 2D planes (X-ray films) (Figure 4.1.2). Changes in imaging angle are equal to rotation and translation of the tooth in 3D space. However, the rotations around the x -axis and y -axis are small enough to be ignored, so rotation in 3D space can be modeled as the rotation around the z -axis in 2D space, and the translation along z -axis can be viewed as scaling in x - y space [31]. Let the rotation around the z -axis be θ , the translations along x -axis and along y -axis be t_x and t_y , respectively, and the scale factor be s . Then a point (x, y) is mapped to $T(x, y)$ after transformation, where $T(x, y)$ is defined as:

$$T(x, y) = s \begin{pmatrix} \cos \theta & -\sin \theta \\ \sin \theta & \cos \theta \end{pmatrix} \begin{pmatrix} x \\ y \end{pmatrix} + \begin{pmatrix} t_x \\ t_y \end{pmatrix}. \quad (4.4)$$

The transformation T is optimized to find the minimum of the matching distances (de-

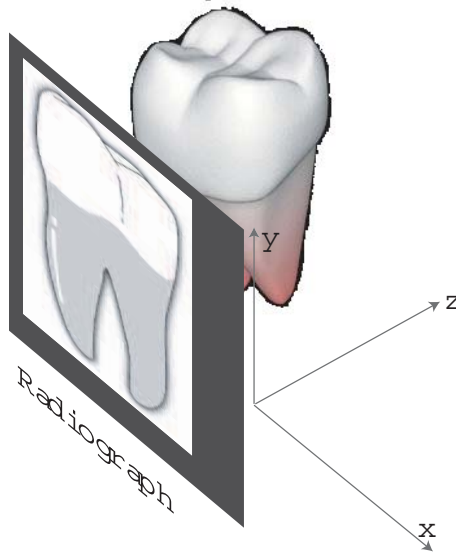


Figure 4.3. Dental radiographs are 2D projections of 3D structures.

defined in section 4.1.2) between the corresponding sections of tooth contours $T(AP)$ and BP . Before initializing T , both shapes should be normalized so that the widths of their bounding boxes are scaled to a constant (100 pixels in our experiments). This normalization sets the matching distances to the same scale so that they can be compared. The initialized transformation T is the transform that aligns the bounding boxes of the two shapes (Figure 4.4(c)).

Shape Registration

Denote the approximation point set for shape A as AP , the approximation point set for shape B as BP and the transformation from AP to BP as T . The *shape registration* stage establishes the correspondence from $T(AP)$ to BP , which preserves the topologies of the two curves, i.e., if a_i and a_j ($a_i, a_j \in T(AP)$) correspond to b_k and b_l ($b_k, b_l \in BP$), respectively, and $i < j$, then $k < l$ [26]. Because the two curves may not fully overlap, *outliers* (the points in either curve that do not have corresponding points in the counterpart curve) may be present. The shape registration algorithm (illustrated in Figure 4.4) is given

as follows:

Algorithm: Shape Registration

Input: Two ordered point sets, TAP and BP , where TAP is the transformed version of AP , i.e., $TAP = T(AP)$. The k th point in TAP is denoted as $TAP(k)$ and the k th point in BP is denoted as $BP(k)$.

Goal: To find the correspondence from TAP to BP , which is denoted as $Cor(i)$, where $i = 1, \dots, |TAP|$, and $1 \leq Cor(i) \leq |BP|$. The notation “ $|\cdot|$ ” denotes the number of elements in the set.

1. Initialization: Initialize $Cor(\cdot)$ as $Cor(i) = \lfloor \frac{|BP|}{|TAP|}(i - 1) + 1 \rfloor$, where $i = 1, \dots, |TAP|$, and $\lfloor m \rfloor$ denotes the greatest integer below m . For descriptive convenience, we add two elements to $Cor(\cdot)$, i.e., $Cor(0) = 1$ and $Cor(|TAP| + 1) = |BP|$.

2. For $i = 1, \dots, |TAP|$ do

$$Cor(i) \leftarrow \arg \min_{k=Cor(i-1)..Cor(i+1)} \|TAP(i) - BP(k)\|;$$

$$Dis(i) \leftarrow \|TAP(i) - Cor(i)\|.$$

3. Repeat step 2 until the algorithm converges or a maximum number of iterations is reached.

4. If some adjacent points in TAP correspond to the same point in BP , i.e., $Cor(i) = Cor(i + 1) = \dots = Cor(i + k)$, and $p = \arg \min_{k=i..i+k} Dis(k)$, then $Cor(i) = nil, \forall i \neq p$. The points for which $Cor(i) = nil$ are the outliers (Figure 4.4(f)).

Denote the subset of TAP that has corresponding points in BP as TAP' . The distance between tooth contours A and B is given as $D_{tc}(A, B)$, where:

$$D_{tc}(A, B) = \min_{\forall T} \frac{1}{|TAP'|} \sum_{\text{all } a' \in TAP'} \|T(a') - Cor(a')\|. \quad (4.5)$$

The distance $D_{tc}(A, B)$ is minimized by searching for the optimal transformation T . This optimization problem is solved iteratively using Sequential Quadratic Programming [36]. Since $Cor(\cdot)$ is affected by T , the correspondence is established at each optimizing iteration.

4.1.3 Matching Dental Work Contours

The shape of dental work is another feature used to match dental radiographs. Since the appearance of dental work varies widely, it is more discriminative to match dental work than to match tooth contours. However, because the dental work does not always have a convex shape, even a slight change in the imaging angle can cause great variation in the shape of dental work in dental radiographs (Figs. 4.5(a), (b), (c)). To solve this problem, we use a metric based on the area of the dental work.

The preprocessing goal is to set the pixels inside the tooth contours to be 0, and the pixels inside the contours of the dental work to be 1 (See Figs. 4.5(d), (e)). Given two images F and G , the ratio of Misaligned Pixels (R_{mp}) between them is defined as:

$$R_{mp}(F, G) = \frac{\sum_{x,y} F'((x, y) \in A) \oplus G'(x, y)}{\sum_{(x,y) \in A} F'(x, y) + G'(x, y)}, \quad (4.6)$$

where A is the overlapped region of tooth pixels and dental work pixels in images F and G , \oplus is the ‘Exclusive-OR’ operator, and F' and G' are the results of preprocessing on F and G , i.e.,

$$F'(x, y) = \begin{cases} 0, & \text{if } F(x, y) \text{ is a tooth pixel;} \\ 1, & \text{if } F(x, y) \text{ is a dental work pixel.} \end{cases} \quad (4.7)$$

Image G' is defined in a similar way. The metric R_{mp} is used to measure the alignment of the dental work. If the dental works in images F and G have similar shapes and are well aligned, then G_{mp} is small. So the distance between the dental works in images F and G is defined as:

$$D_{dw}(F, G) = \min_{\text{for all } T} R_{mp}(T(F), G), \quad (4.8)$$

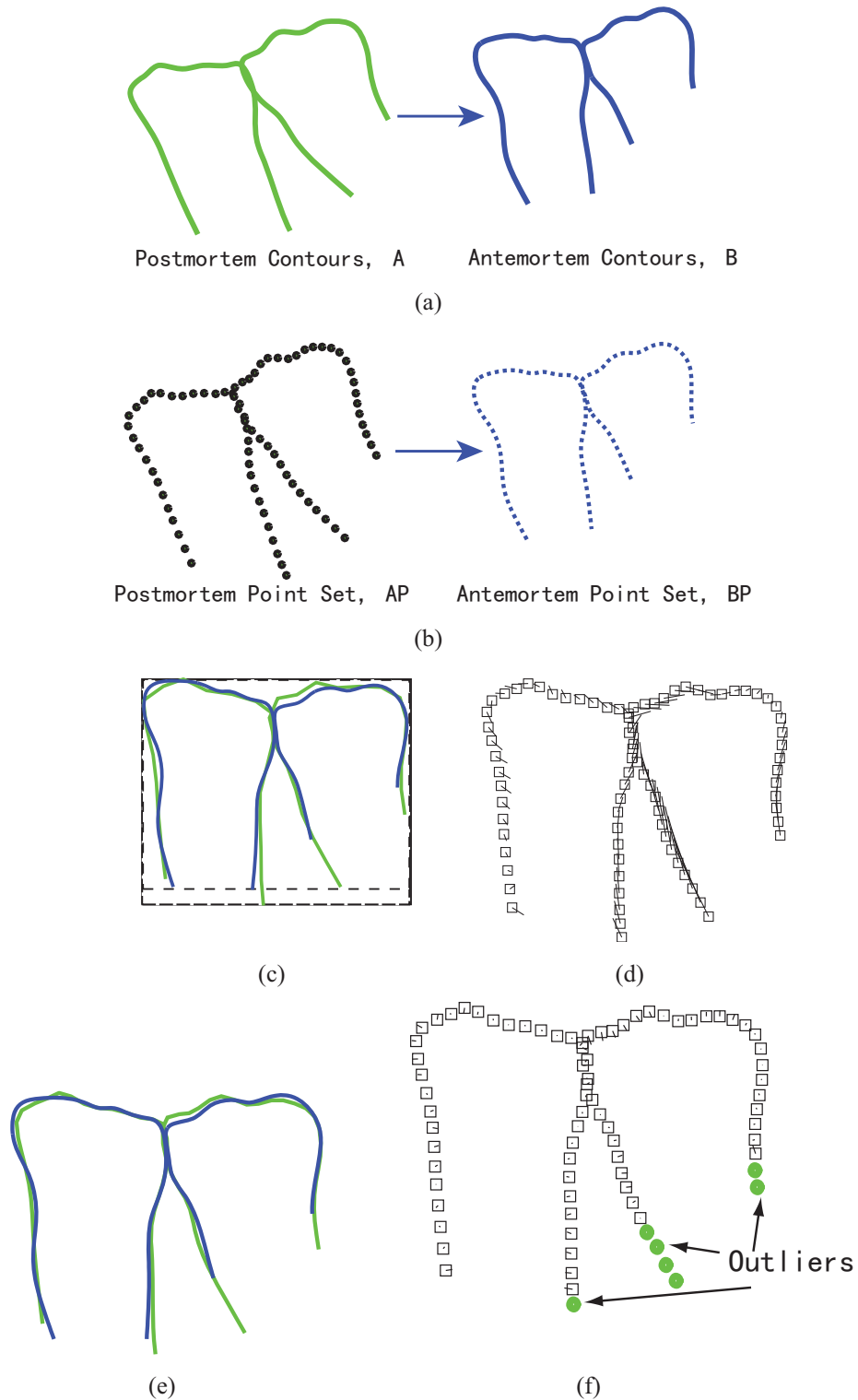


Figure 4.4. Shape registration process. (a) Continuous tooth contours; (b) discrete tooth contours; (c) initialization by aligning bounding boxes; (d) initialized point correspondence; (e) aligned contours after optimum transformation; (f) correspondence after alignment and outlier detection.

where T is the transformation defined in Equation (4.4) and optimized using Sequential Quadratic Programming [36].

4.1.4 Fusing the Matching Distances

In the previous section we defined the distance D_{tc} , which measures the difference between tooth contours, and the distance D_{dw} , which computes the difference between dental work contours. Combining these two matching distances should improve the retrieval accuracy. However, for teeth without dental work, D_{dw} is not available. To handle this situation, we propose to combine the distances D_{tc} and D_{dw} via posterior probabilities.

Let ω_g represent the matching between radiographs of the same subject (genuine class), and ω_i represent the matching between radiographs belonging to two different subjects (imposter class). The likelihood distributions (shown in Figure 4.6) of D_{dw} for genuine and imposter classes, $p(D_{dw}|\omega_g)$ and $p(D_{dw}|\omega_i)$, were estimated using approximately 100 genuine and 100 imposter matchings. A Parzen window approach with a Gaussian kernel was used to estimate the probability distributions, $p(D_{dw}|\omega_i)$ and $p(D_{dw}|\omega_g)$. The two posterior probabilities are

$$P(\omega_i|D_{dw}) = \frac{p(D_{dw}|\omega_i)P(\omega_i)}{p(D_{dw})}, \quad (4.9)$$

$$P(\omega_g|D_{dw}) = \frac{p(D_{dw}|\omega_g)P(\omega_g)}{p(D_{dw})}, \quad (4.10)$$

where the priors, $P(\omega_i)$ and $P(\omega_g)$, are assumed to be 0.5. The probability $p(D_{dw})$ is defined as $p(D_{dw}) = 0.5 \cdot [p(D_{dw}|\omega_i) + p(D_{dw}|\omega_g)]$.

The matching distance D_{tc} is combined with D_{dw} to generate the fused distance D_f between the two teeth, A and B , as follows

$$D_f(A, B) = D_{tc}(A, B) \cdot (1 + \alpha \cdot (T(D_{dw}))), \quad (4.11)$$

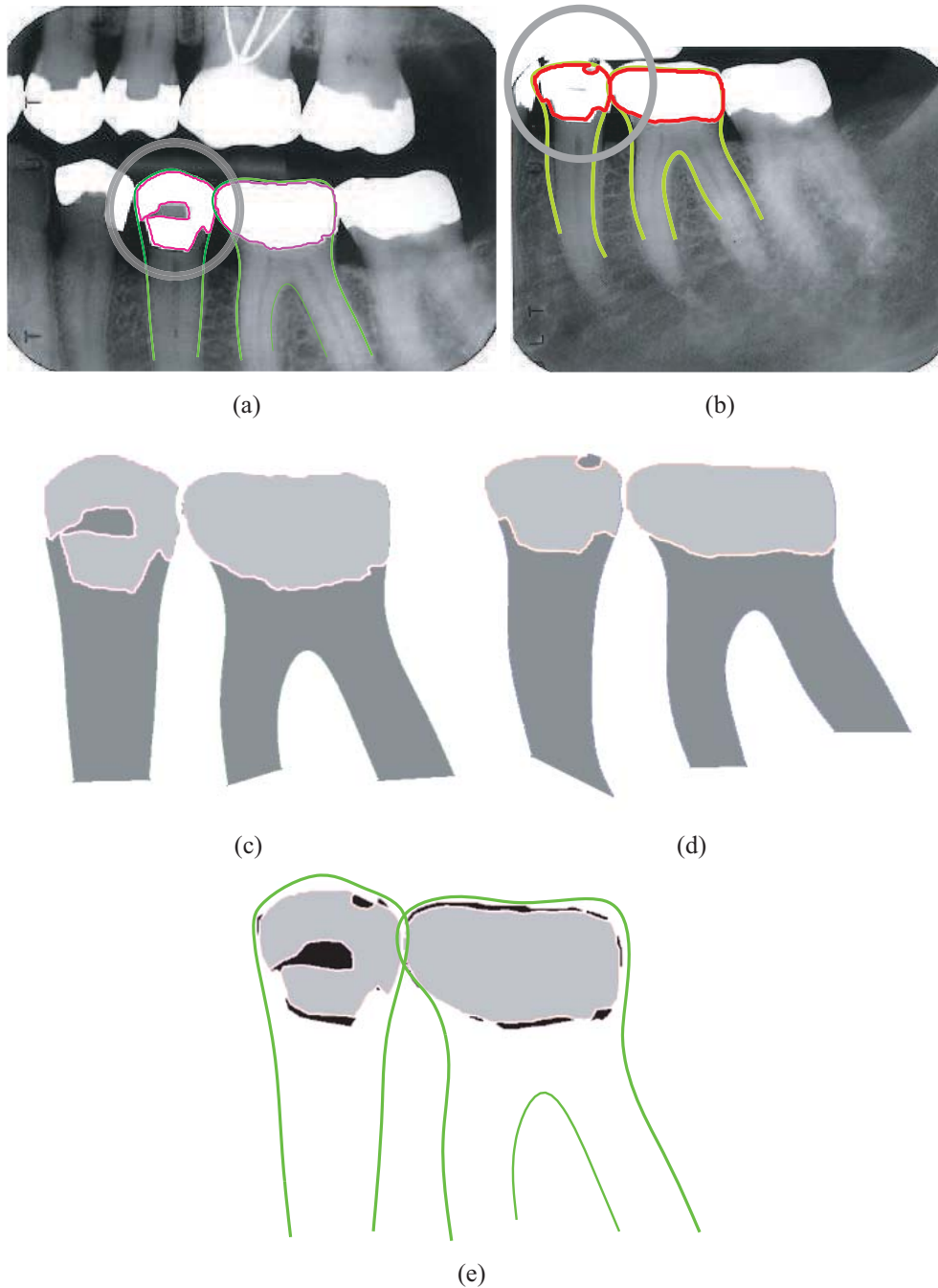


Figure 4.5. Dental work merging due to a change in the imaging angle. The hole in the circled dental work seen in image (a) is occluded when viewed from the angle shown in (b) even though both the images are of the same tooth; (c) preprocessed image for two teeth in image (a); (d) preprocessed image for two teeth in image (b); (e) result of 'Exclusive-Or' operation for the two teeth. Pixels of value '1' are displayed in black, and the pixels of value '0' are displayed in gray.

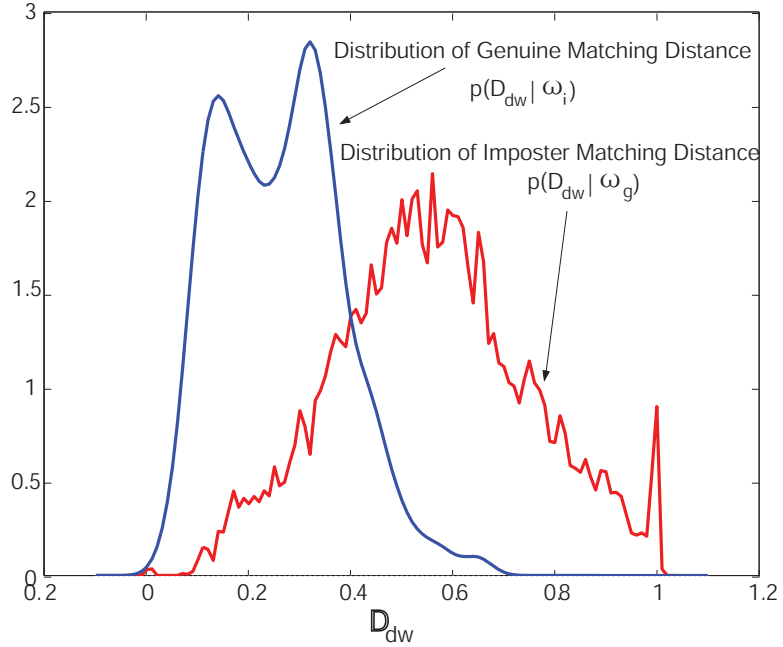


Figure 4.6. Distribution of matching distances based on the shape of dental work.

and

$$T(D_{dw}) = \begin{cases} P(\omega_i|D_{dw}) - P(\omega_g|D_{dw}), & \text{if } D_{dw} \text{ is available} \\ 0, & \text{otherwise,} \end{cases} \quad (4.12)$$

where α weighs the importance of the dental work shape in fusion ($0 \leq \alpha \leq 1$). The combination scheme described above implies that if D_{dw} is more likely to be the distance between the genuine teeth, i.e., $P(\omega_g|D_{dw}) > P(\omega_i|D_{dw})$, D_{tc} is reduced by multiplying it with $(1 + \alpha \cdot (T(D_{dw})))$, which is less than 1; if D_{dw} is more likely to be the distance between imposter teeth, i.e., $P(\omega_g|D_{dw}) < P(\omega_i|D_{dw})$, D_{tc} is amplified by multiplying it with $(1 + \alpha \cdot (T(D_{dw})))$, which is larger than 1; if D_{dw} is not available, D_{tc} is not modified.

In practice, neighboring teeth are matched as a unit denoted as $D_f([R_i, R_{i+1}], [R'_i, R'_{i+1}])$, where R_i and R_{i+1} are neighboring teeth in image R , and R'_i and R'_{i+1} are neighboring teeth in image R' ; the notation $[R_i, R_{i+1}]$ means the concatenation of R_i and R_{i+1} , and similarly for $[R'_i, R'_{i+1}]$. Distances $D_{tc}(\cdot)$ and $D_{dw}(\cdot)$ are also computed based on pairs of neighboring teeth. This scheme has the advantage that

both tooth contours and their relative positions contribute to the matching score.

4.2 Matching Subjects

Given a database of AM radiographs, the identity associated with a set of PM radiograph images is established by matching the tooth sequences in the PM images to a database of tooth sequences in labeled AM radiographs. Note that for each subject in the database, there may be more than one AM image. *Tooth correspondence*, which means that teeth from the two sequences have the same indices, is established by comparing the indices of teeth, which are estimated by registering the tooth sequence to the dental atlas, introduced in chapter 3.

Given two tooth sequences R and S , suppose ζ is one of the top- m estimated tooth indices for teeth in sequence R , and η is one of the top- m estimated tooth indices for teeth in sequence S . In our experiments, we use $m = 3$. Despite the fact that the numbers of teeth in R and S may be different, as long as there are corresponding teeth, denote them as $(R_1, S_1), (R_2, S_2), \dots, (R_n, S_n)$, where $n \geq 1$. We denote the distance between sequences R and S based on ζ and η as $D_{\zeta, \eta}(R, S)$, which is given by

$$D_{\zeta, \eta}(R, S) = \begin{cases} \frac{1}{n} \sum_{i=1}^n D_f(R_i, S_i), & \text{if } n \geq 1, \\ \infty, & \text{otherwise,} \end{cases} \quad (4.13)$$

where $D_f(R_i, S_i)$ is the distance between teeth R_i and S_i , which is obtained in the previous section. The minimum value of $D_{\zeta, \eta}$ among all the combinations of top- m estimations for R and S is set to the value of the distance between sequences R and S , written as

$$D(R, S) = \min_{\forall \zeta, \eta} D_{\zeta, \eta}(R, S). \quad (4.14)$$

To estimate the similarity of subjects Φ and Ψ , assume that sequence R belongs to Φ and sequence S belongs to Ψ . Denote the distance measure between subjects Φ and Ψ as

$D_S(\Phi, \Psi)$, which is given by:

$$D_S(\Phi, \Psi) = \frac{\sum_{R \in \Phi} \min_{S \in \Psi} \kappa(R, S)}{\#\{R | R \in \Phi, \sum_{S \in \Psi} n(R, S) > 0\}}, \quad (4.15)$$

where Φ means all tooth sequences of subject Φ , Ψ means all tooth sequences of subject Ψ , and

$$\kappa(R, S) = \begin{cases} D(R, S), & \text{if } n(R, S) > 0, \\ \infty, & \text{if } n(R, S) = 0, \end{cases} \quad (4.16)$$

where $n(R, S)$ is the number of corresponding teeth used for computation of $D(R, S)$, and $\{\#\{R | R \in \Phi, \sum_{S \in \Psi} n(R, S) > 0\}\}$ is the number of sequences of Φ that have corresponding teeth in any sequence of Ψ . According to Equation (4.16), the distance between the sequence R of subject Φ and the subject Ψ is first calculated as the minimum distance between sequence R and all the sequences of subject Ψ . Then we calculate the average distances between the sequences of subject Ψ and subject Φ that have corresponding teeth.

To compare the experimental results with and without the use of tooth index information, we developed a method for matching subjects that does not use results of atlas registration, but uses the results of the tooth-level matching to establish correspondence between two sequences, R and S , instead. The numbers of teeth in R and S are not necessarily the same. Suppose a possible tooth correspondence starts from the i th tooth in R and the j th tooth in S ($i = 1$ or $j = 1$), denoted as $\mathbb{C} = \{(R_i, S_j), (R_{i+1}, S_{j+1}), \dots, (R_{i+l}, S_{j+l})\}$, where R_{i+k} is the corresponding tooth of S_{j+k} , $k = 0, \dots, l$. Then the correct tooth correspondence should minimize the average distance between corresponding teeth, defined as:

$$D(R, S) = \min_{\substack{\forall i, j, \\ i=1 \\ \text{or } j=1}} \frac{1}{l} \sum_{k=0}^{l-1} D_f([R_{i+k}, R_{i+k+1}], [S_{i+k}, S_{i+k+1}]), \quad (4.17)$$

where $[\cdot, \cdot]$ means that the contours of neighboring teeth are concatenated and matched as a unit, as discussed in section 4.1.4. Figure 4.7 illustrates the computation of D in matching a 5-tooth sequence to a 7-tooth sequence. Figure 4.8 shows some correctly established tooth

correspondences.

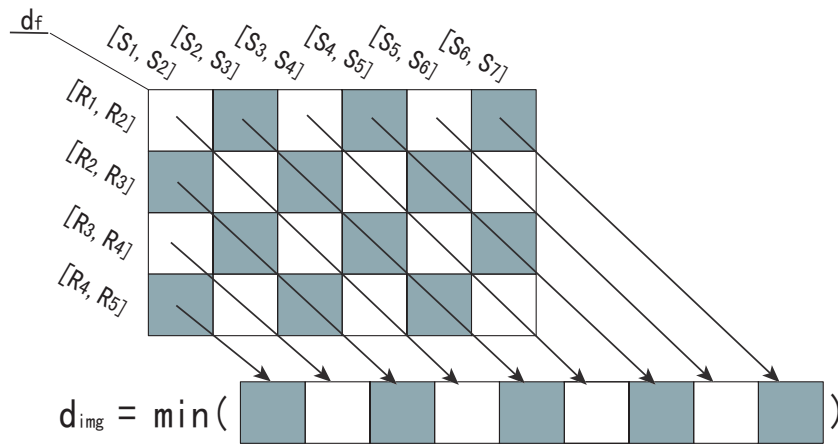


Figure 4.7. Coupling 4 pairs of neighboring teeth with 6 pairs of neighboring teeth. The matching score between each pair of neighboring teeth is calculated and the average is taken along the arrows. The results are listed in the bottom bar of black and white cells, and the minimum of these values is defined as the matching distance between the two sequences.

4.3 Experimental Results

We evaluated our algorithm on the two databases mentioned in Chapter 1. Figure 4.9 shows some of the AM and PM images associated with one subject in the databases. The first database includes 33 subjects, with several AM and PM images from each subject. Each panoramic or bitewing image is divided into two sequences: an upper set of teeth and a lower set of teeth. The teeth in the same sequence will not change their relative positions in different radiographs, while teeth from different sequences will probably change relative positions in different radiographs because of the opening and closing of the jaws. So we match the two sequences of teeth separately.

The database contains a total of 360 PM and 316 AM dental sequences, containing a total of 810 PM teeth and 892 AM teeth. The experimental results reported here are based on the experiments involving retrieving 29 subjects out of the 33 subjects, because the images

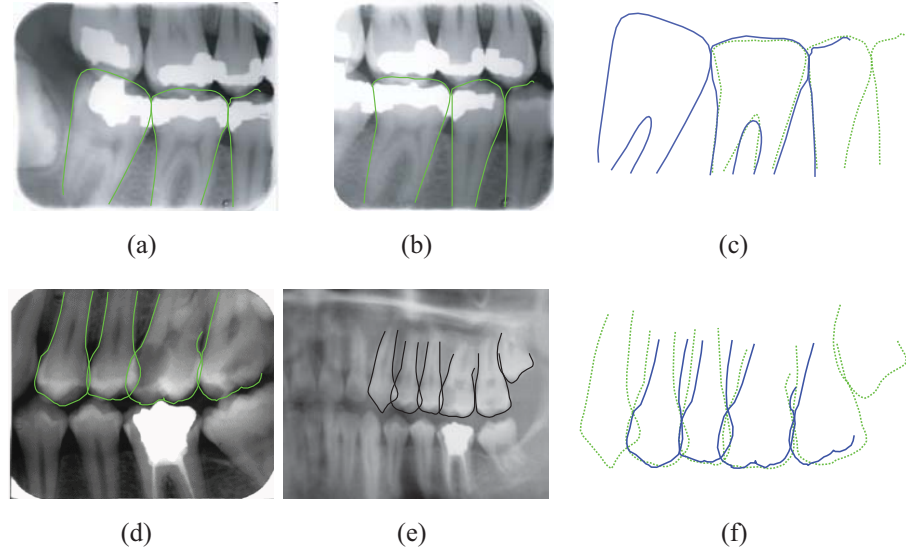
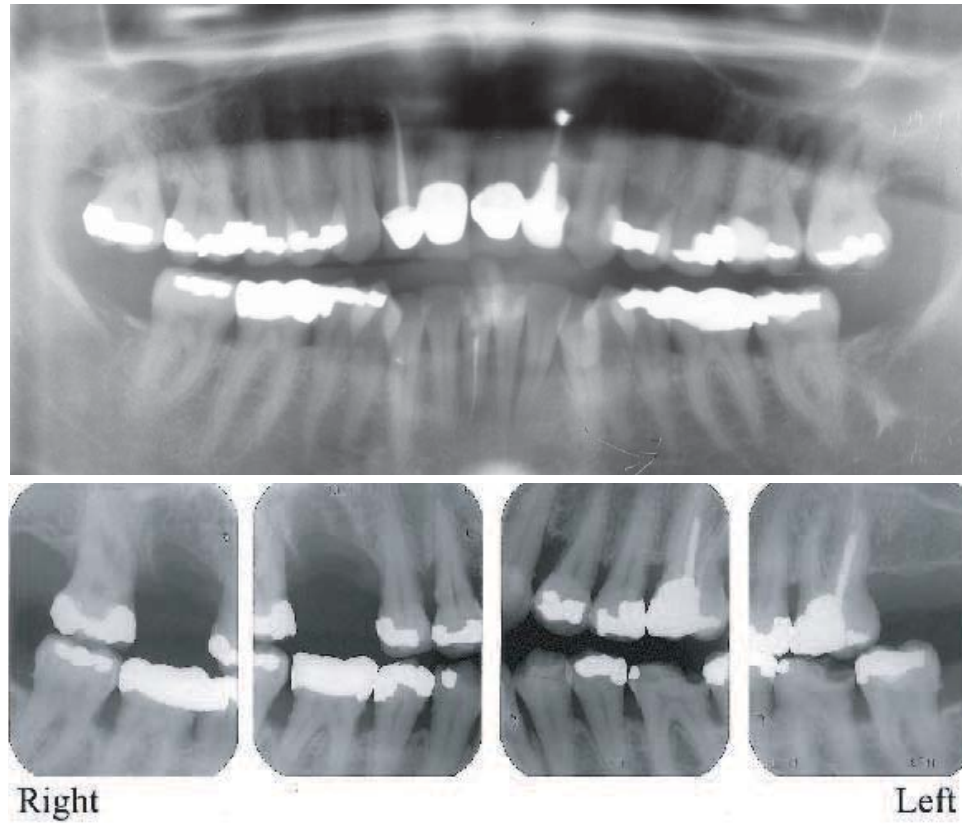


Figure 4.8. Two examples of tooth correspondence. Tooth contours in (a) and (b) are paired up in (c); tooth contours in (d) and (e) are paired up in (f).

of 4 remaining subjects cannot be used for following reasons: i) tooth contours of subjects 10 and 36 cannot be extracted due to poor image quality (Figs. 4.14 and 4.17), ii) subjects 14 and 21 have variations in dental structure due to tooth development or orthodontic treatment (Figs. 4.15 and 4.16). We did not try to establish the identities of these 4 subjects, but instead used the AM images of these 4 subjects as the imposter identities in the database. In other words, the 29 subjects (312 PM sequences) used in our experiments were matched to all the 33 subjects (316 AM sequences) in the database.

The dental radiographs are matched in two steps. The first step is shape registration - the PM teeth are matched with the AM teeth individually. Matching a pair of teeth takes ~ 2 seconds on a PC with a 2.99 GHz Pentium 4 processor. It takes about 1.7 hours to perform the matching process to retrieve a subject from the 33 subject database. To estimate the probability distribution of the matching distances for contours of dental work ($p(D_{dw}|\omega_i)$) and ($p(D_{dw}|\omega_g)$), we use a Parzen window approach with Gaussian kernels [25]. By comparing the accuracies of teeth matching (all with dental work) with different values for the weight coefficient in Equation (4.11), $\alpha = 0, 0.1, 0.2, \dots, 1$, the optimum



(a)



(b)

Figure 4.9. Some AM images (a) and PM images (b) of a single individual in the database.

value of α , $\alpha = 1$, is selected.

The second step is subject identification. The distances between images are generated first. Figure 4.10 shows some examples of query images matched with a genuine and an impostor database image. The distance score between two images with corresponding teeth is smaller than the distance score for the impostor teeth pair. Figure 4.11 shows the top 4 retrievals for three different query images, and how the query shapes are matched to the database shapes. In some cases, query images were not correctly matched because: (i) the images were of poor quality, so the tooth shapes were not reliably extracted, (ii) the tooth was only partially visible, and (iii) different individuals had similarly shaped teeth.

Figure 4.12 shows the Cumulative Match Characteristics (CMC) curve for retrieving 29 subjects from the database consisting of 33 subjects, compared with results obtained by the method without using tooth index information. Without using tooth index information, the accuracy for the top-1 retrieval is 20/29 (= 69%). Using top-2 retrievals, the retrieval accuracy is 76%. The accuracy reaches 100% for the top-20 retrievals. Using the tooth indices obtained by registering the images to the dental atlas, the accuracy for top-1 retrieval is 21/29 (= 72%). Using top-2 retrievals, the retrieval accuracy is 27/29 (=93%). The accuracy reaches 100% when the top-7 retrievals are used. It is clear that using tooth index information greatly improves the retrieval accuracy.

AM and PM images of the subjects that were not correctly retrieved in the top-1 retrieval are shown in Figs. 4.18, 4.19, 4.20, 4.21, 4.22, 4.23, 4.24, 4.25. The reasons for the incorrect retrievals are as follows: (i) subjects 2, 28, and 42 have only one panoramic radiograph in AM records, and no panoramic radiographs in PM records. Matching between different types of images (i.e., panoramic against bitewing) results in large matching distances, even for genuine subjects. (ii) The extensive overlapping of upper and lower teeth in images of subjects 9 and 25 results in unreliably extracted tooth contours. (iii) Change in the appearance of dentition due to loss of teeth or tooth filling for subjects 1 and 16. (iv) The number of available teeth for matching AM and PM radiographs of subject 39 is

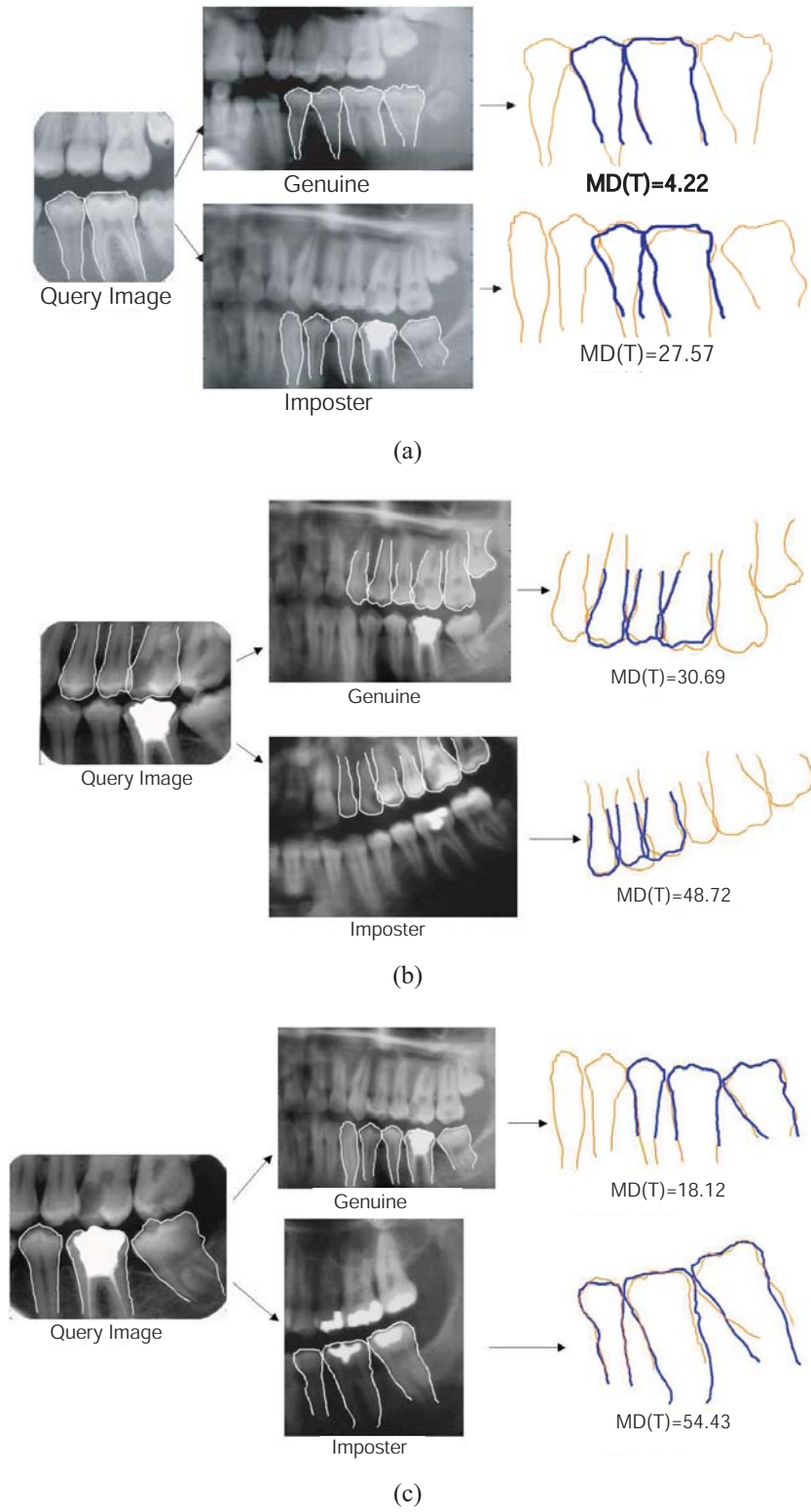


Figure 4.10. Examples of matching. The gray lines represent the tooth shapes in the database and the query images; the black lines represent the query shapes after transformation. Note that in these examples, the matching distance for the genuine AM images is smaller than the matching distance for the imposter AM images.

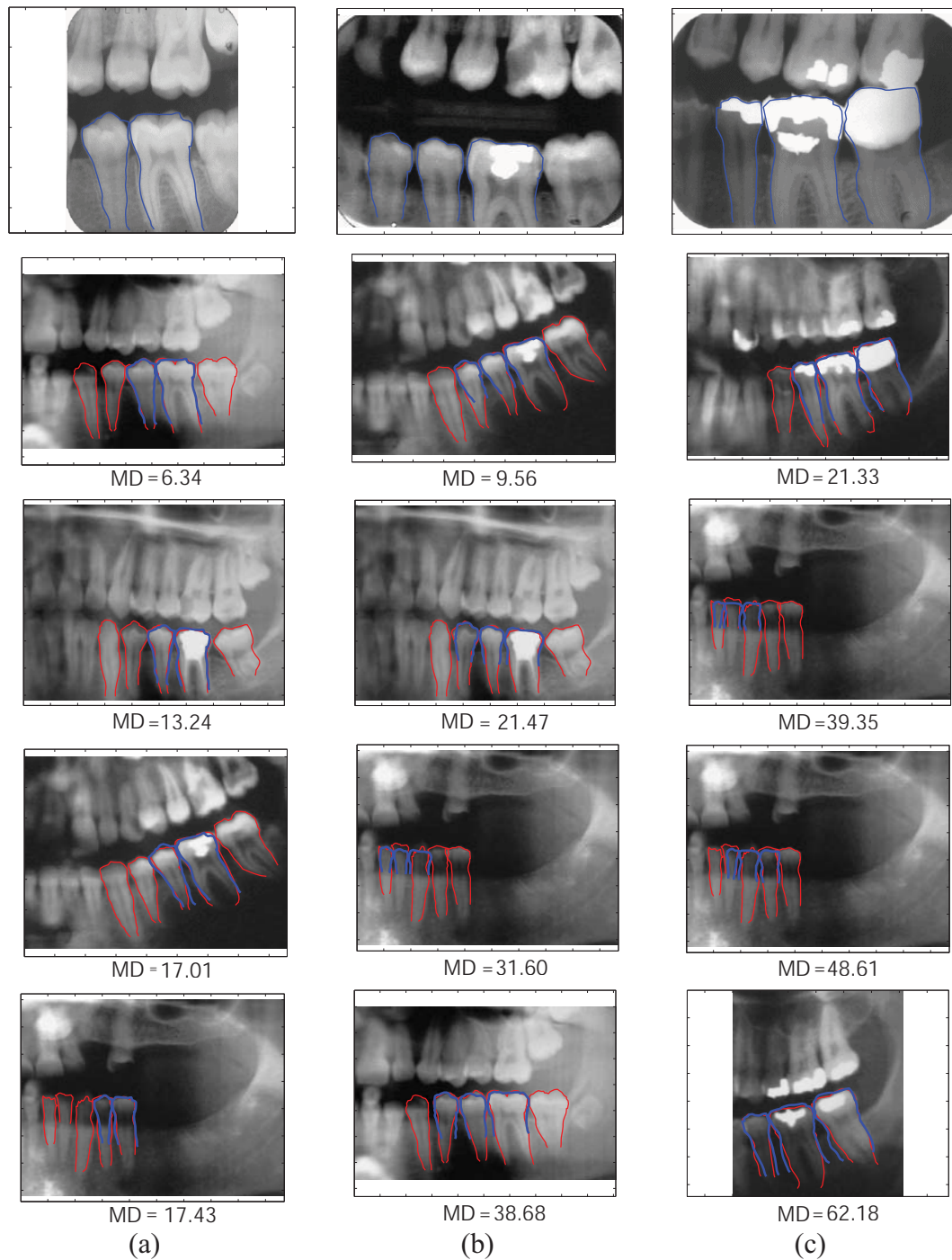


Figure 4.11. The top-4 retrievals for 3 different queries. The first image in each column is the query image and the remaining four images are the top-4 retrievals. The genuine AM images are ranked first for these three queries.

insufficient for discriminating genuine and imposter subjects.

A second set of experiments involved retrieval of 29 PM subjects used in the previous experiment from a larger AM database, consisting of 33 AM subjects in the previous experiment and 100 additional subjects. The database is composed of 360 PM tooth sequences (810 teeth) and 1,064 AM tooth sequences (3,271 teeth). It takes about 7 hours to perform the matching processes to retrieve one subject from the 133 subject database. Figure 4.13 shows the Cumulative Match Characteristics (CMC) curve for retrieving 29 subjects from the database consisting of 133 subjects. The accuracy for top-1 retrieval is 19/29 (= 66%), the top-4 accuracy is 23/29 (= 79%), and the top-13 accuracy is 26/29 (=90%). The reasons for the failed retrieval of the remaining 3 cases within the top-13 retrievals are as follows: (i) The appearance of dentition of subject 1 has changed due to loss of teeth (Figure 4.18) and (ii) subjects 2 and 42 have only one panoramic radiograph in AM records, and no panoramic radiographs in PM records (Figures 4.19 and 4.25). Matching between different types of images (i.e., panoramic against bitewing) results in large matching distances, even for genuine subjects.

4.4 Summary

This chapter examined methods for matching dental radiographs. The matching method proposed here is based on the tooth contours of corresponding teeth, as well as shape of the dental work region if dental work is present in both teeth. The matching distances obtained based on tooth contours and dental work contours are fused to generate matching distances between the unidentified subject and subjects in the database.

Experiments were conducted on retrieving 29 PM subjects from two databases of 33 AM subjects and 133 AM subjects, respectively. For the database of 33 AM subjects, it takes about 1.7 hours to retrieve one subject. The top-1 retrieval accuracy is 21/29 (= 72%). Using top-2 retrievals, the retrieval accuracy is 27/29 (=93%). The accuracy reaches 100%

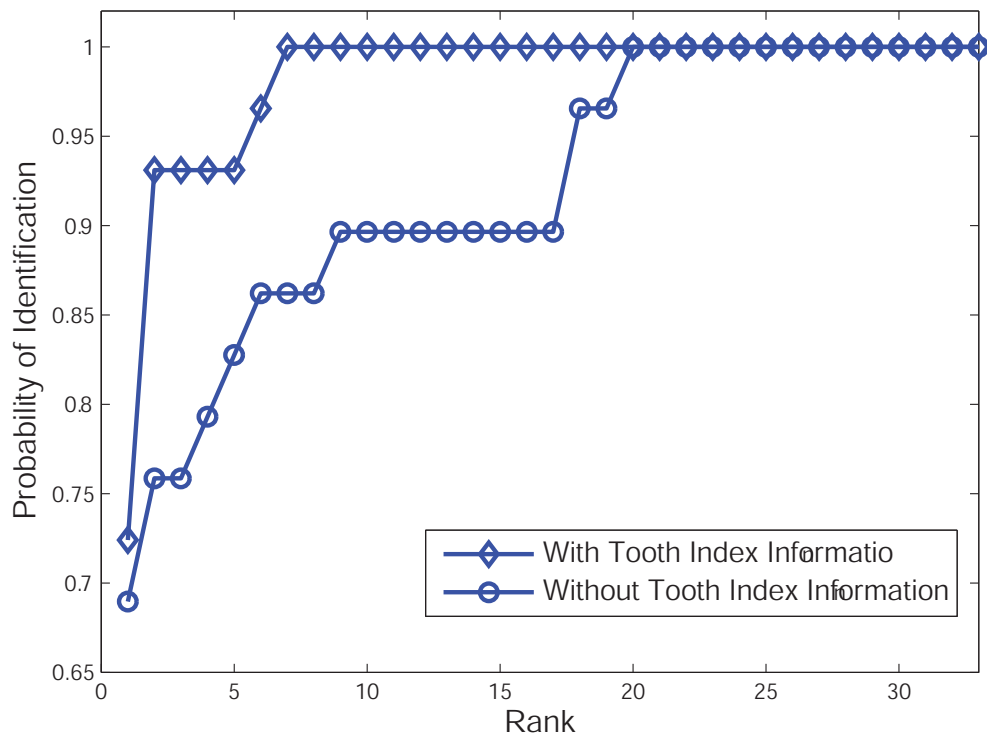


Figure 4.12. Cumulative matching characteristics (CMC) curves for subject retrieval in the database of 33 subjects.

when the top-7 retrievals are used.

For the experiments with the database of 133 AM subjects, it takes about 7 hours to retrieve one subject. The accuracy for top-1 retrieval is 19/29 (= 66%), the top-4 accuracy is 23/29 (= 79%), and the top-13 accuracy is 26/29 (=90%). The reasons for failed retrieval of the remaining 3 cases within the top-13 retrievals are (i) change in dentition appearance, and (ii) matching between different types of dental radiographs.

Table 4.1 gives a breakdown of the computational requirements for each of the major modules in our system. The column “Time for One Call” shows the time for one execution of the program for the procedure. The column “Overall Time” shows the time the procedure takes during the entire process of matching one PM query image set against one AM database image set. The column “Avg. Number of Calls” means the average number of

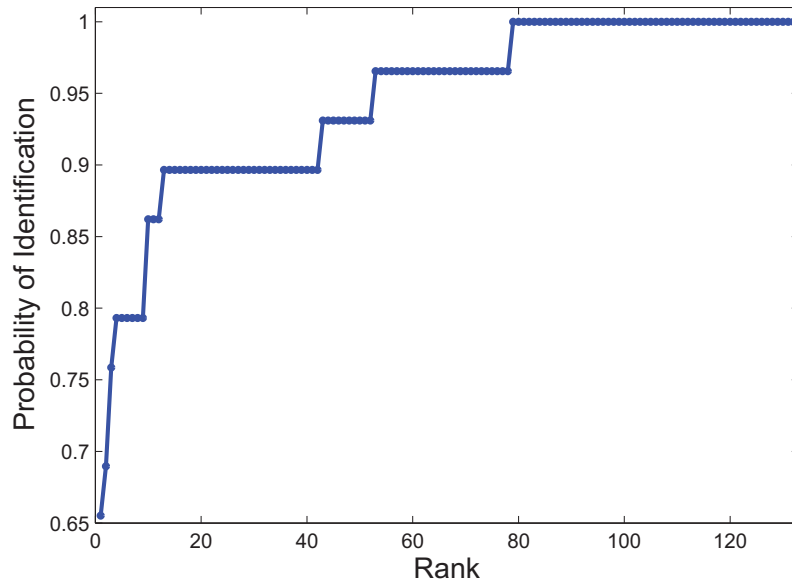
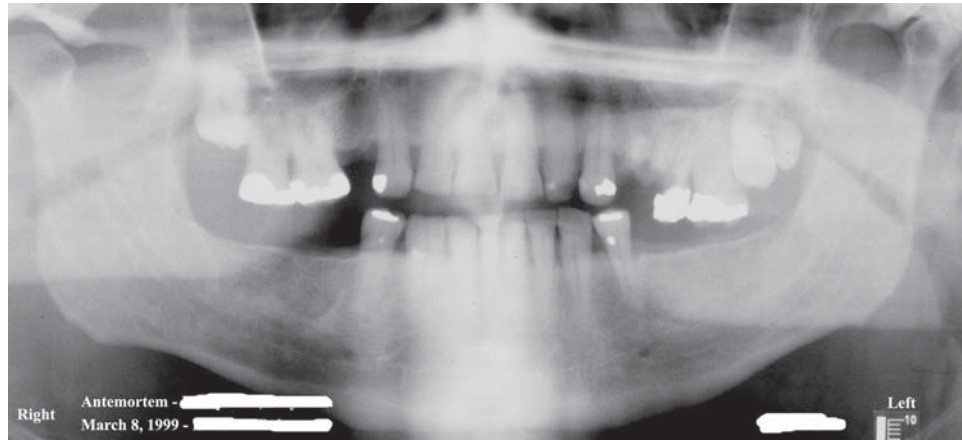


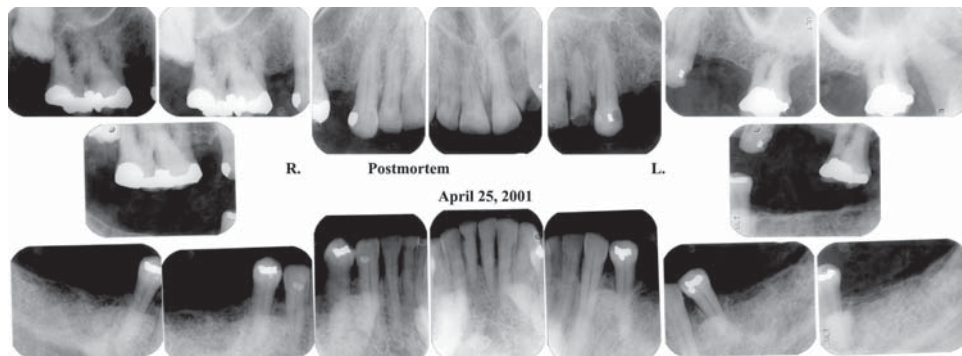
Figure 4.13. Cumulative matching characteristics (CMC) curves for subject retrieval in the database of 133 subjects.

times the procedure is called during the entire process. Note that the AM database image set has been processed beforehand. Each PM query contains several images. After image segmentation, upper and lower rows of teeth are treated as different sequences. Each PM query includes 6 images and 10.9 sequences on average, since some images have both upper and lower rows while others have only upper or lower row. The software has not been optimized and most of the algorithms are implemented in Matlab 7.0. The speed of matching process can be significantly accelerated if the algorithms are implemented in C/C++. To get an idea of this speedup, the gradient vector flow (GVF) algorithm used for tooth contour extraction was implemented in both Matlab and C. It takes 5.75 seconds for the Matlab program to process a 159×236 image, while it takes only 0.76 seconds for the C program to process the same image.

The retrieval accuracy could be improved by using digital radiographs since they provide more gray levels, which will lead to higher reliability of the extracted tooth contours and dental work contours.



(a)



(b)

Figure 4.14. Subject 10 was not tested for retrieval due to poor image quality. (a) AM radiograph; (b) PM radiographs.

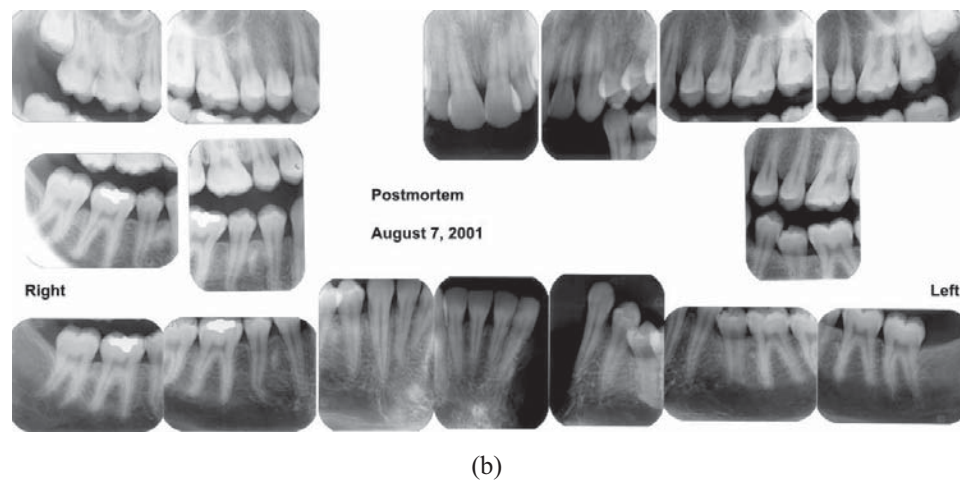
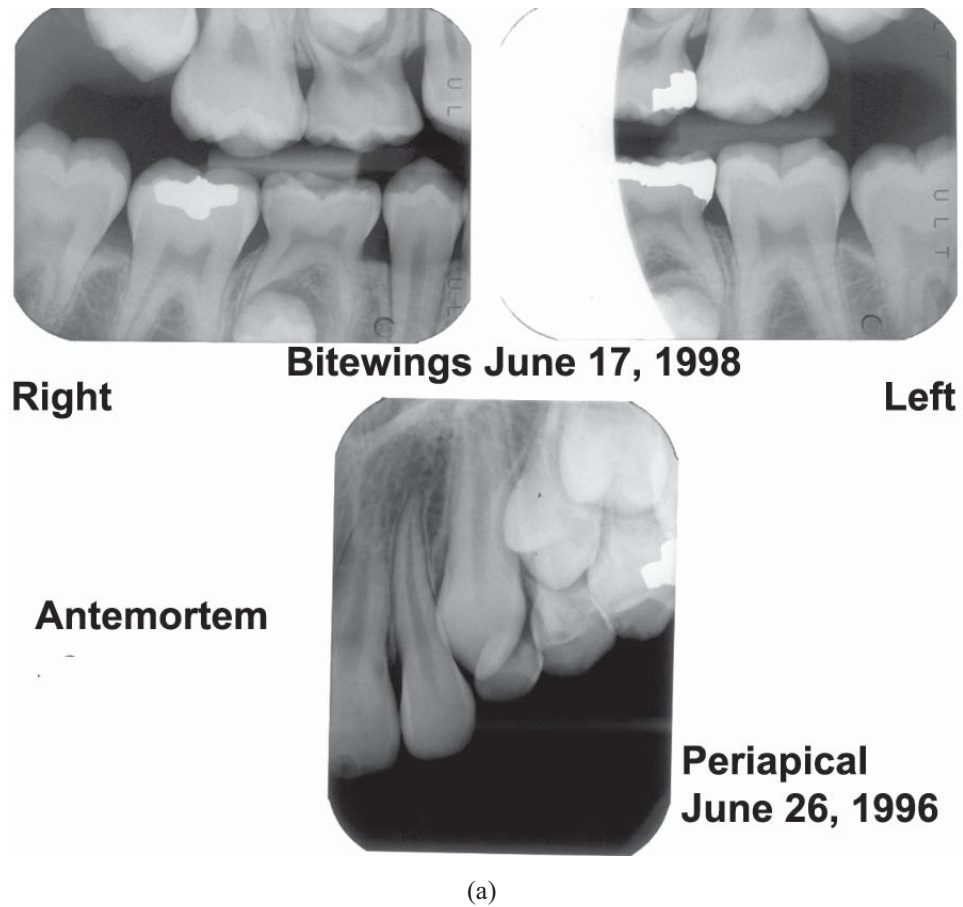
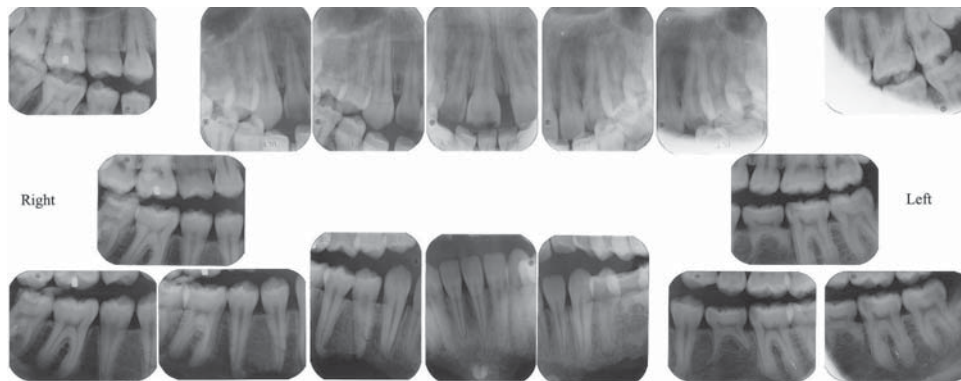


Figure 4.15. Subject 14 was not tested for retrieval due to eruption of new teeth in AM radiographs. (a) AM radiographs; (b) PM radiographs.



(a)

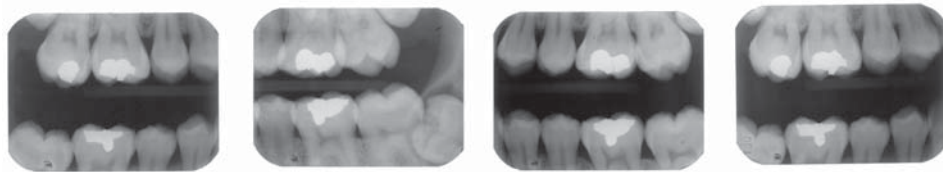


(b)

Figure 4.16. Subject 21 was not tested for retrieval due to eruption of new teeth in AM radiographs. (a) AM radiographs; (b) PM radiographs.

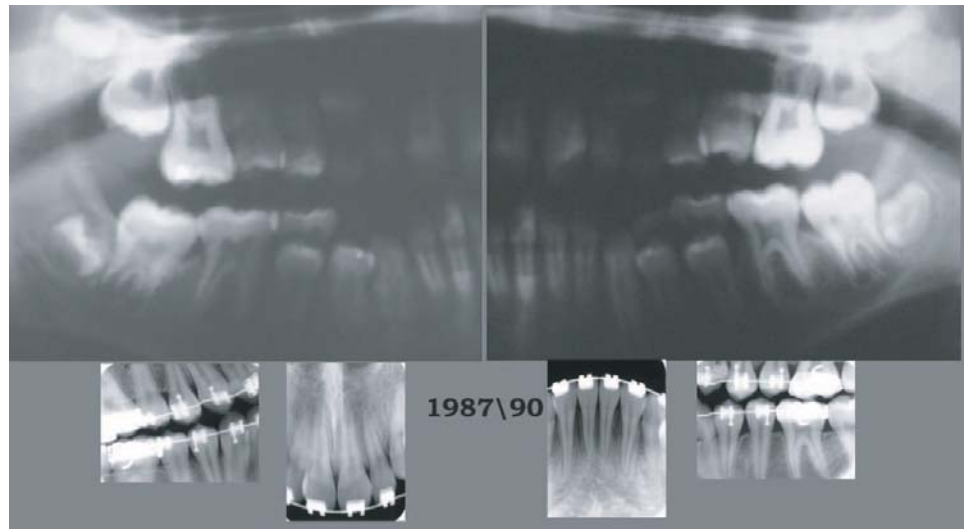


(a)

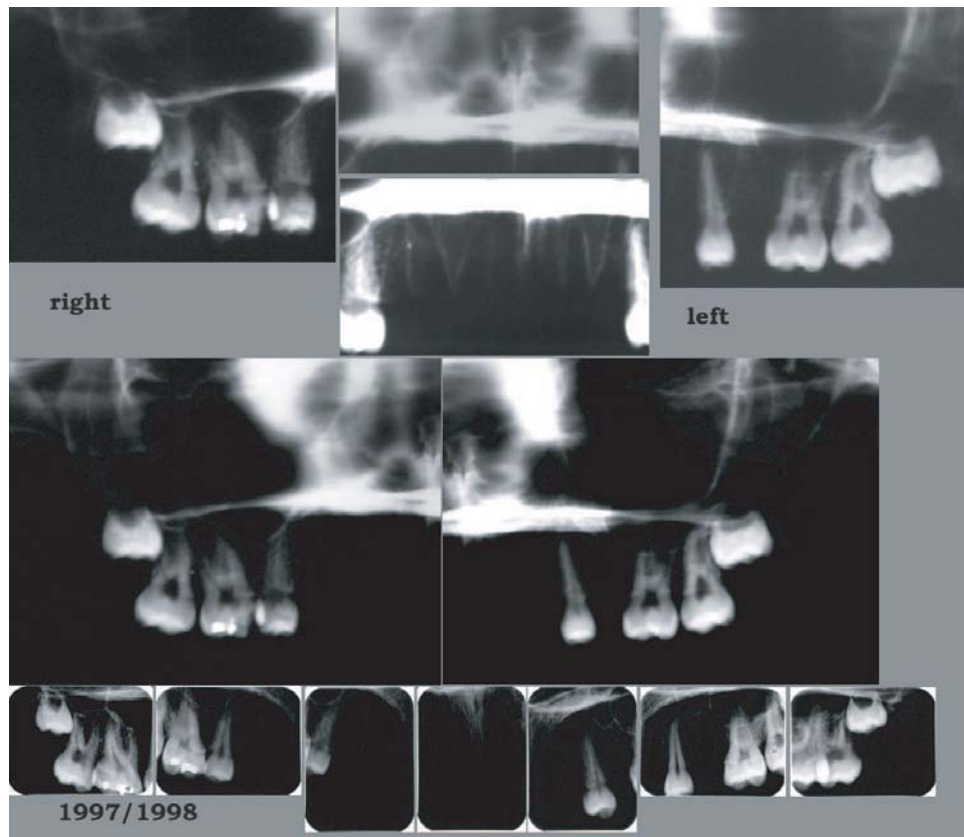


(b)

Figure 4.17. Subject 36 was not tested for retrieval due to poor image quality. (a) AM radiograph; (b) PM radiographs.



(a)

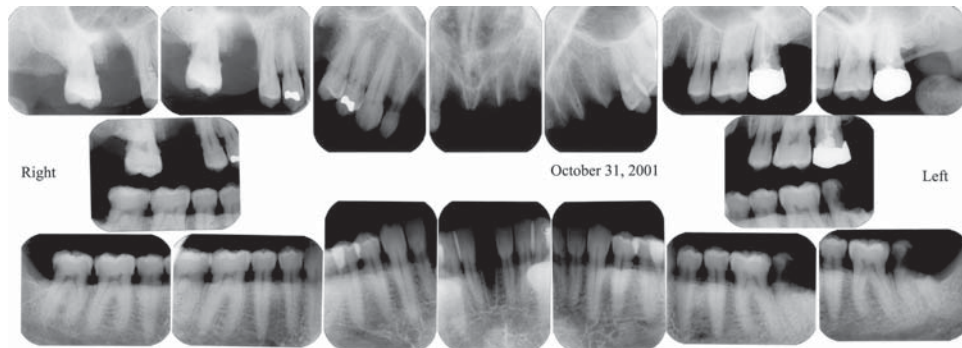


(b)

Figure 4.18. Subject 1 was not correctly retrieved from the database due to changes in the dentition caused by loss of teeth. (a) AM radiographs; (b) PM radiographs.

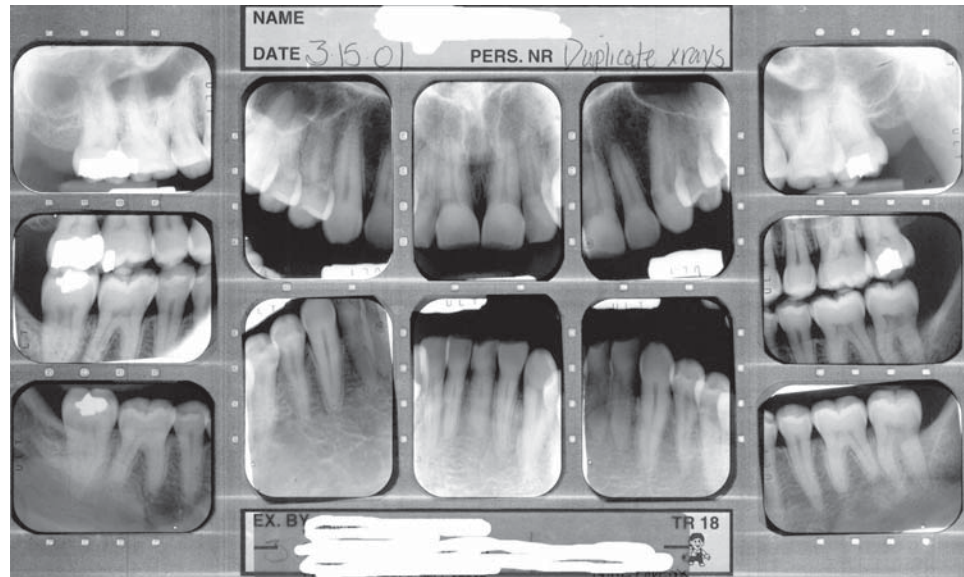


(a)

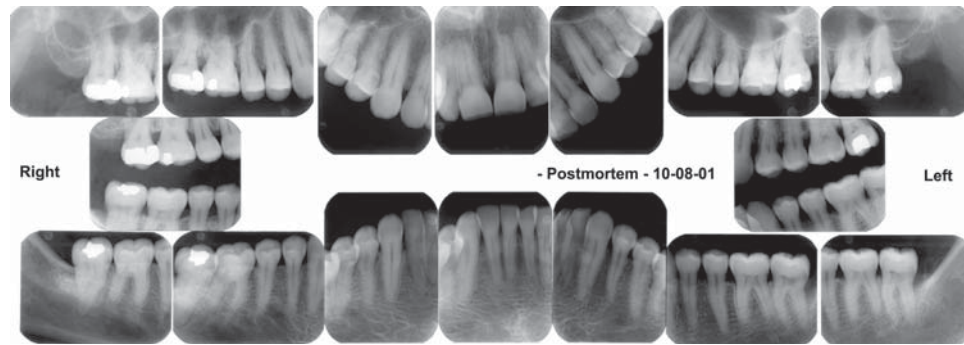


(b)

Figure 4.19. Subject 2 was not correctly retrieved from the database due to incorrect AM tooth contour extraction from the only available panoramic image. (a) AM radiograph; (b) PM radiographs.



(a)



(b)

Figure 4.20. Subject 9 was not correctly retrieved from the database due to incorrect AM tooth contour extraction caused by overlapping upper and lower rows of teeth. (a) AM radiographs; (b) PM radiographs.

Table 4.1. CPU (2.99 GHz Pentium 4) Time for Matching one PM Query Image Set to one AM Database Image Set

Procedure	Time for One Call	Overall Time	Avg. Number of Calls
Feature Extraction	172.5s per Image	17.3m	6
Atlas Registration	0.165s per Sequence	1.8s	10.9
Matching	2s per Tooth Pair	3.1m	93

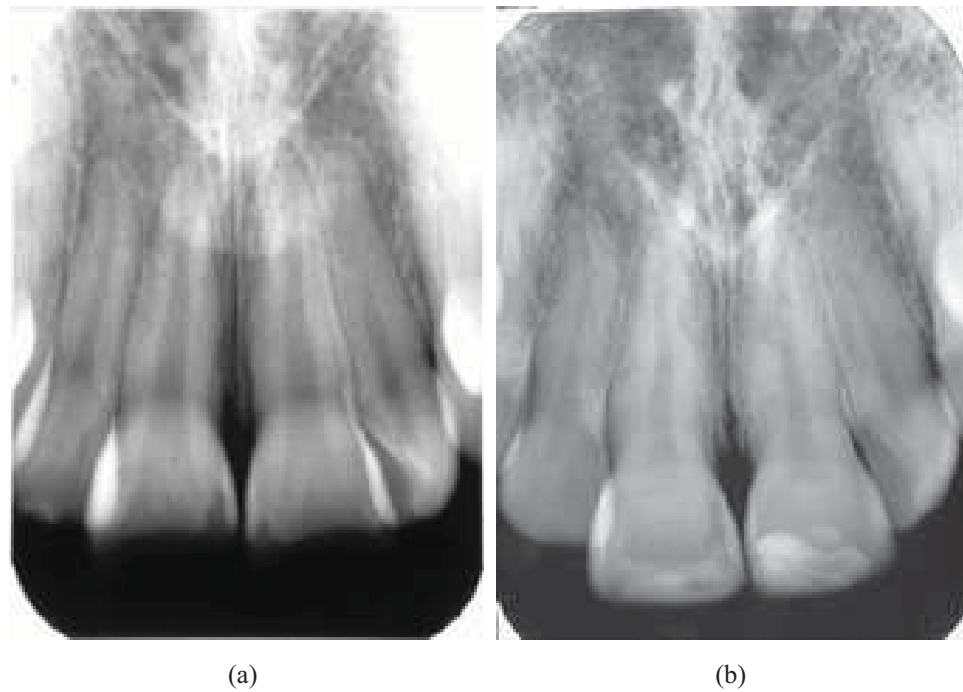
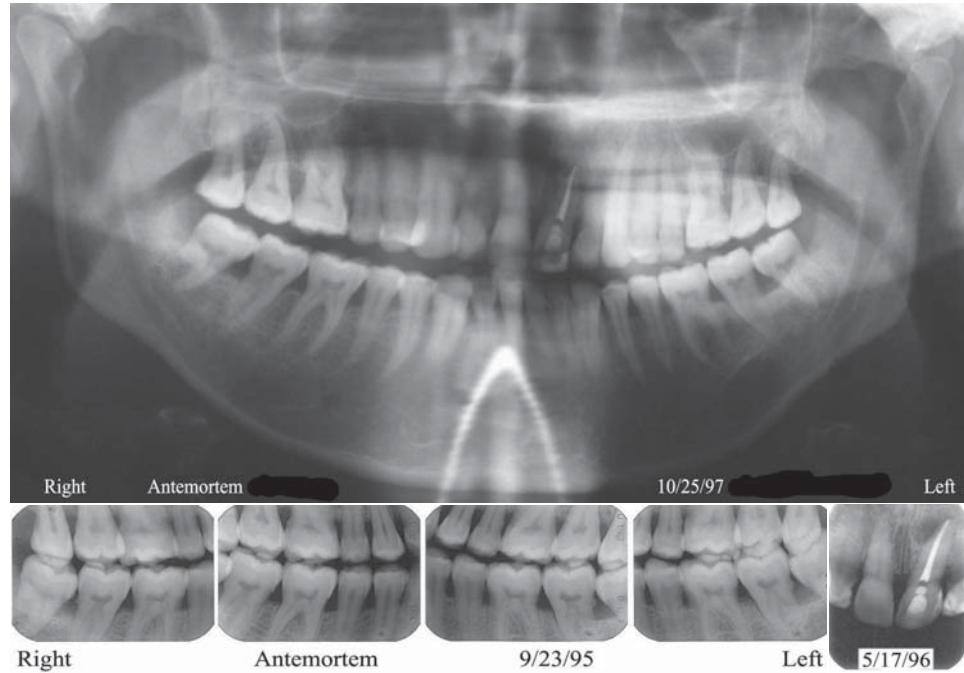
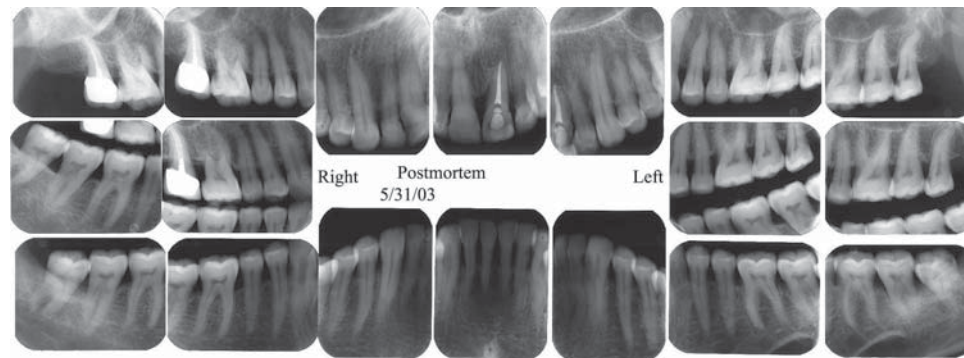


Figure 4.21. Subject 16 was not correctly retrieved from the database due to changes in tooth appearances in AM and PM radiographs. (a) AM radiograph; (b) PM radiograph.

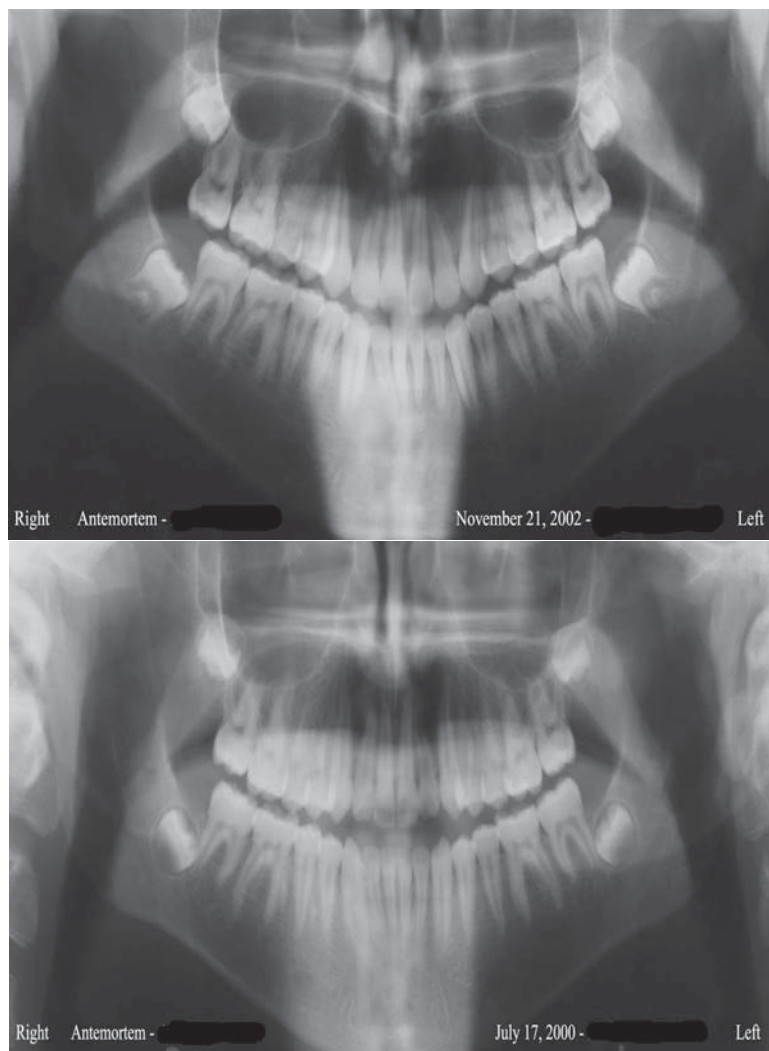


(a)

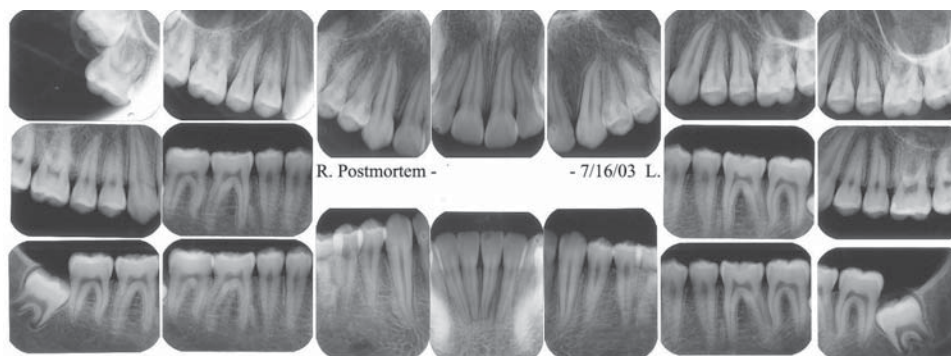


(b)

Figure 4.22. Subject 25 was not correctly retrieved from the database due to incorrect AM tooth contour extraction from the panoramic image and the bitewing images where upper and lower rows of teeth overlap. (a) AM radiographs; (b) PM radiographs.



(a)

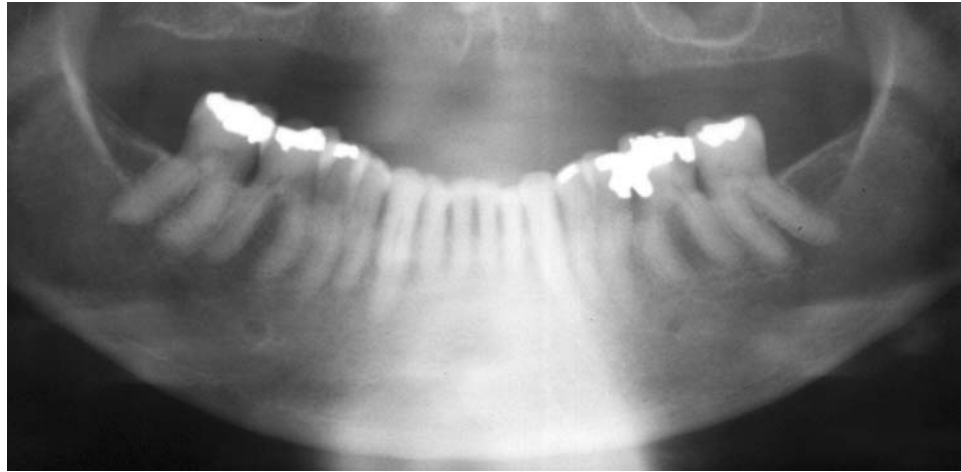


(b)

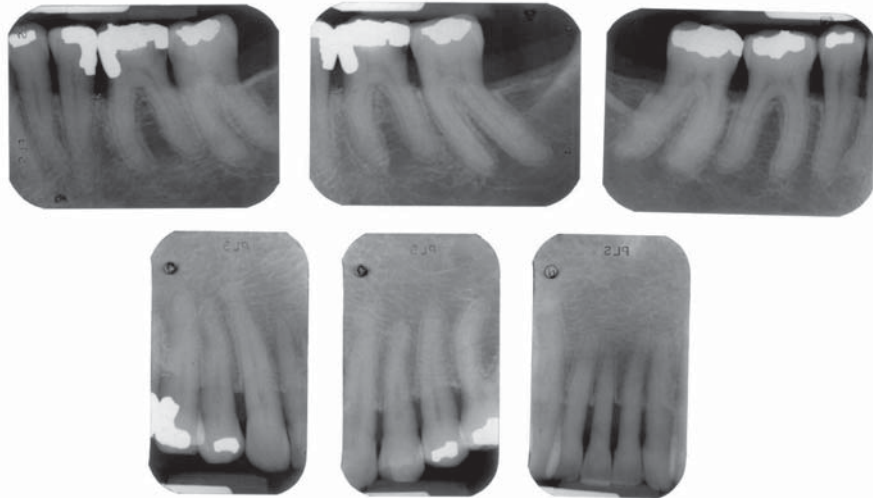
Figure 4.23. Subject 28 was not correctly retrieved from the database due to incorrect AM tooth contour extraction from the only available panoramic image. (a) AM radiograph; (b) PM radiographs.



Figure 4.24. Subject 39 was not correctly retrieved from the database due to insufficient number of teeth in the AM image. (a) AM radiograph; (b) PM radiographs.



(a)



(b)

Figure 4.25. Subject 42 was not correctly retrieved from the database due to incorrect AM tooth contour extraction from the only available panoramic image. (a) AM radiograph; (b) PM radiographs.

CHAPTER 5

Conclusions and Future Directions

We have developed an automatic system for using dental radiographs to identify disaster victims. The system has three stages: feature extraction, atlas registration, and matching and retrieval. Related publications for Chapter 2 are [27], [27], [40], [18]. The publication for Chapter 3 is [41]. Publications for Chapter 4 are [19], [40] and [18]. Major contributions of the thesis are summarized in the following sections.

5.1 Feature Extraction

- *Segmentation of Radiographs.* We have proposed a fast marching based algorithm to segment radiographs into homogeneous regions so that each region contains only one tooth. This method utilizes the characteristics of dental radiographs in that soft tissue and bone have different pixel intensity. This method can be extended to analyze other types of radiographs [20].
- *ASM-Based Tooth Contour Extraction.* We have proposed an active shape model (ASM) to extract tooth contours. The incorporated statistical shape information in ASM deals with shape extraction difficulties caused by poor quality of dental radiographs. We have made some changes to the traditional ASMs so that ASMs can be

used for tooth contour extraction. The proposed changes are as follows:

- *Aligning Tooth Contours for Training.* Tooth contours are smooth curves and have no salient feature points. To align tooth contours, our method aligns the given shape to an atlas and registers the points in the shape to nodes in the atlas.
- *Rotation and Scaling of Training Shapes During Training.* The training method incorporates rotation and scaling into the ASM so that rotation and scaling need not be modeled in the transformation.
- *Different Searching Strategies for Crown and Root Nodes.* All nodes in a traditional ASM use the same search strategy. For an ASM for tooth shape extraction, crown nodes and root nodes have to use different search strategies because the boundaries of crowns are located at the outermost gradients while the boundaries of roots are located at the strongest gradients.
- *Smoothed Gradient Field for Searching Optimal Positions of ASM nodes.* Traditional ASMs use profile correlation to find the optimal positions for the nodes, which requires the search range to be sufficiently large to include the optimal position. If the true optimal position is not in the search range, an incorrect position will be located for the nodes. We use the smoothed gradient field to provide the search guidance for the root nodes in the ASM, so that even if the optimal position is not in the search range, a position closest to the true optimal position can be located.
- *Robust Weighting During ASM-based Shape Approximation.* Newly detected node positions need to be approximated with the trained ASMs. To deal with the noise in the detected positions, robust weighting used in linear regression is applied. Since rotation and scaling have been modeled with ASMs, the entire approximation procedure can be deduced into a linear regression form in vector space, and thus the robust weighting can be used.

- *Extraction of Contours of Dental Work.* We use anisotropic diffusion to enhance the images and extract the contours of dental work with a reasonable assumption that pixel values of dental restoration follow a Gaussian distribution [18].

5.2 Atlas Registration

- *Hybrid HMM/SVM Model for Representation of Dental Atlas.* Tooth states in the HMM combined with SVMs model the shape of teeth, and distance states in the HMM model the inter-teeth distance caused by missing teeth [41].
- *Construction of Observation Sequences.* An observation sequence is an alternating sequence of tooth shapes and distances between successive teeth. To compensate for the difference between image resolutions of AM and PM images, the tooth shapes are normalized to a fixed width, and the distances between teeth are regularized with the width of neighboring teeth [41].

5.3 Matching

- *Matching of Tooth Contours.* Tooth contours are open curves. To match tooth contours, correspondence between the tooth contours has to be established. We have developed an iterative procedure to align tooth contours and compute distances based on the corresponding segments of the two curves [18].
- *Matching of Contours of Dental Work.* Topological changes may occur between the contours of the same type of dental work in different images. We have developed an algorithm to align dental work and compute the distance between two images using a metric of overlapping pixels [18].
- *Fusion of Matching Scores of Tooth Contours and Contours of Dental Work via Posterior Probability.* Dental restorations are not always present in the dental radi-



Figure 5.1. A dental X-ray shows loss of jaw bones caused by periodontal disease.

ographs. To fuse the matching distances between tooth contours and dental restoration contours, we developed a scheme based on posterior probability [18].

- *Calculation of Distances between Subjects Based on Distances between Teeth.* We developed a scheme to compute the distance between an image and a subject and the distance between two subjects [18].

5.4 Future Directions

The following directions should be considered for future research.

- *Abnormality-Based Identification.* Dental abnormalities, such as tumors, periodontal disease, tooth malformations and abnormal resorptions, are important features used by human experts in matching dental radiographs [1]. Figure 5.1 shows an example of loss of jaw bones due to periodontal disease. To detect dental abnormality, a dental radiograph needs to be registered to a dental atlas, and a statistical approach is needed to discover the uniqueness of the given image in terms of tooth shape, tooth position, and intensity, etc.

- *Knowledge Inference.* Knowledge of the victim, such as age, gender, and periodontal disease, etc., can be inferred from dental radiographs and matched with the side (ancillary) information of suspected victims to narrow the search scope. An expert system incorporating rich odontological knowledge needs to be developed to fulfill the task.
- *User Feedback-Based Improvement.* A machine learning scheme can be developed to improve the system based on user feedback, including user correction on tooth contours, tooth indices, and final decision by human experts.
- *Matching of Non-tooth Feature.* Features shown in dental radiographs, e.g., the trabecular pattern of mandible bones and the shape of sinus and canals in the mandible and maxilla bones [1], can be extracted and used for identification.

APPENDICES

APPENDIX A

Database Description

The number and types of images as well as the source of images for each subject are listed in table A.1. In the table, source A is the Criminal Justice Information Service (CJIS) division of the FBI; source B is the Washington State Police Department; source C is Dr. Howell from West Virginia University. The subject IDs are not continuous due to removal of some duplicate subjects from the database after the subjects were indexed. So, the total number of subjects is only 33 though the subject IDs range from 1 to 42.

Table A.1. List of Types, Numbers, and Sources of Images in the Database.

Subject ID	Number and Type of Images						Source
	Antemortem (AM)			Postmortem (PM)			
	Panoramic	Bitewing	Periapical	Panoramic	Bitewing	Periapical	
1	2	2	2	0	0	8	A
2	1	0	0	0	2	12	A
3	1	0	6	0	0	6	A
4	1	4	0	0	1	1	A
5	0	2	0	0	2	0	A
6	0	4	1	0	1	15	A
8	0	6	0	0	2	15	A
9	0	2	10	0	2	14	A
10	1	0	0	0	0	10	A
11	0	7	4	0	1	13	A
12	0	2	1	0	1	2	A
13	0	10	0	0	2	14	A
14	0	2	1	0	2	14	A
16	0	0	1	0	0	1	B
20	0	3	0	0	2	14	B
21	0	4	1	0	2	14	B
22	0	9	14	0	0	16	B
23	0	4	14	0	2	14	B
24	2	4	16	0	2	14	B
25	1	4	1	0	1	17	B
26	0	4	14	0	0	16	B
27	2	4	0	0	0	16	B
28	2	0	0	0	0	18	B
29	0	2	1	0	2	14	B
31	0	4	14	0	2	4	C
32	0	4	0	0	4	0	C
33	0	4	14	0	4	0	C
35	0	2	0	0	2	0	C
36	1	0	0	0	4	0	C
37	0	2	14	0	0	16	C
39	0	0	1	0	2	0	C
42	1	0	0	0	0	6	C

APPENDIX B

Anisotropic Diffusion

The anisotropic diffusion method was introduced by Perona and Malik [48] and modified by others [64], [37], [14]. It is used for smoothing images while preserving boundaries in the images, which is a desired property for image enhancement. Let the original image be denoted as $I(x, y, 0)$, and the transformed image after the t^{th} iteration be $I(x, y, t)$. Then the anisotropic diffusion equation is given by

$$\frac{\partial I}{\partial t} = \text{div}(c(x, y, t)\nabla I), \quad (\text{B.1})$$

where div is the divergence operator, ∇ is the gradient operator, and $c(x, y, t)$ is the smoothing criterion. When c is constant, Equation (B.1) reduces to the isotropic heat diffusion equation, which is a smoothing operation on the image. If we want to encourage smoothing within each region in preference to smoothing across the boundaries, $c(x, y, t)$ can be defined as $c(x, y, t) = g(|\nabla I(x, y, t)|)$. The function $g(\cdot)$ should be chosen such that when $|\nabla I(x, y, t)|$ is small, $g(\cdot)$ is large to encourage smoothing, and when $|\nabla I(x, y, t)|$ is large, $g(\cdot)$ is small to inhibit smoothing. Since the boundaries of regions are assumed to have a large gradient magnitude $|\nabla I(x, y, t)|$, this process smoothes the pixels inside the homogeneous regions, while suppressing smoothing across the boundaries. Thus, the means of the intensities inside the regions do not change while their variance decreases. If we

assume that gray level distributions of each region can be modeled as a Gaussian, this has the effect of reducing the overlap of the Gaussians for different regions and minimizing the classification error. One option of specifying $g(\cdot)$ is Weickert's definition [61]:

$$g(x) = \begin{cases} 1, & \text{if } x = 0 \\ 1 - e^{-C_m(x/\lambda)^{-2m}}, & \text{if } x > 0, \end{cases} \quad (\text{B.2})$$

where λ is the threshold for the flux change, C_m is selected such that $g'(\lambda) = 0$, and m controls the speed of the flux changes. For enhancing dental radiographs, the values for the parameters were chosen as $\lambda = 5$ and $m = 12$.

BIBLIOGRAPHY

BIBLIOGRAPHY

- [1] ABFO body identification guidelines. <http://www.abfo.org/ID.htm>.
- [2] Disaster victim identification. <http://www.interpol.int/Public/DisasterVictim/Guide>.
- [3] Disaster victims identification information management center starts operation in Phuket. http://english.people.com.cn/200501/12/eng20050112_170385.html.
- [4] Lowess and loess: Local regression smoothing. http://www.mathworks.com/access/helpdesk/help/toolbox/curvefit/ch_data7.html.
- [5] Smoothing spline : Fitting data (curve fitting toolbox). http://www.mathworks.com/access/helpdesk/help/toolbox/curvefit/ch_fit15.html.
- [6] Dental records beat DNA in tsunami IDs. *New Scientists*, 2516:12, Sept. 2005. <http://www.newscientist.com/article.ns?id=mg18725163.900>.
- [7] Forensic identification of 9/11 victims ends, February 2005. <http://abcnews.go.com/WNT/story?id=525937&page=1>.
- [8] B. Adams. The diversity of adult dental patterns in the United States and the implications for personal identification. *Journal of Forensic Science*, 48(3):497–503, 2003.
- [9] B. Adams. Establishing personal identification based on specific patterns of missing, filled and unrestored teeth. *Journal of Forensic Science*, 48(3):487–496, 2003.
- [10] E. Allwein, R. E. Schapire, and Y. Singer. Reducing multiclass to binary: A unifying approach for margin classifiers. *J. Machine Learning Research*, 1:113–141, 2000.
- [11] E. Arana and L. Marti-Bonmati. Digital dental radiology. <http://www.priory.com/den/dentrvg1.htm>.
- [12] S. Belongie, J. Malik, and J. Puzicha. Feature based 2d shape transformation. *IEEE Trans. Pattern Analysis and Machine Intelligence*, 24(4):509–522, 2002.
- [13] Paul J. Besl and Neil D. McKay. A method for registration of 3d shapes. *IEEE Trans. Pattern Analysis and Machine Intelligence*, 14(2):239–256, 1992.

- [14] M.J. Black, G. Sapiro, D.H. Marimont, and D. Heeger. Robust anisotropic diffusion. *IEEE Trans. Image Processing*, 7(3):421–432, 1998.
- [15] F.L. Bookstein. Principal warps: thin-plate splines and the decomposition of deformations. *IEEE Trans. Pattern Analysis and Machine Intelligence*, 11(6):567–585, 1989.
- [16] W. M. Campbell. A SVM/HMM system for speaker recognition. In *Proc. ICASSP*, volume II, pages 209–212, Hong Kong, April 2003.
- [17] Andrea Castellani, Debora Botturi, Manuele Bicego, and Paolo Fiorini. Hybrid HMM/SVM model for the analysis and segmentation of teleoperation tasks. In *Proc. IEEE International Conference on Robotics & Automation*, pages 2918–2923, New Orleans, LA, April 2004.
- [18] Hong Chen and Anil Jain. Dental biometrics: Alignment and matching of dental radiographs. *IEEE Trans. on Pattern Analysis and Machine Intelligence*, 27(8):1319–1326, 2005.
- [19] Hong Chen and Anil Jain. Dental biometrics: alignment and matching of dental radiographs. In *Proc. WACV (Workshop on Applications of Computer Vision)*, pages 316–321, Breckenridge, Colorado, January 2005.
- [20] Hong Chen and Carol Novak. Segmentation of hand radiographs using fast marching methods. In *Proc. SPIE Conference on Medical Imaging*, volume 6144, pages 68–76, San Diego, California, 2006.
- [21] Yi Chen, Anil Jain, and Sarat Dass. Fingerprint deformation for spoof detection. In *Proc. Biometric Symposium*, Crystal City, VA, 2005.
- [22] H. Chui, J. Rambo, R. Shultz, and A. Rangarajan. Registration of cortical anatomical structures with robust 3d point matching. In *Proc. Information Processing in Medical Imaging*, pages 168–181, 1999.
- [23] T. F. Cootes and C. J. Taylor. Active shape models - ‘smart snakes’. In *Proc. British Machine Vision Conf.*, pages 266–275, 1992.
- [24] R. Derakhshani, Stephanie Schuckers, and Larry Hornak. Determination of vitality from a non-invasive biomedical measurements for use in fingerprint scanners. *Pattern Recognition*, 36(2):383–396, 2003.
- [25] Richard O. Duda, Peter E. Hart, and David G. Stork. *Pattern Classification*, chapter 10, pages 164–174. Wiley Interscience, 2nd edition, 2001.

- [26] Nicolae Duta, Anil K. Jain, and Marie-Pierre Dubuisson-Jolly. Automatic construction of 2D shape models. *IEEE Trans. Pattern Analysis and Machine Intelligence*, 23(5):433–446, May 2001.
- [27] G. Fahmy, D. Nassar, E. Haj-Said, H. Chen, O. Nomir, J. Zhou, R. Howell, H. H. Ammar, M. Abdel-Mottaleb, and A. K. Jain. Towards an automated dental identification system (ADIS). In *Proc. ICBA (International Conference on Biometric Authentication)*, volume LNCS 3072, pages 789–796, Hong Kong, July 2004.
- [28] M. Figueiredo, J. Leitaó, and Anil K. Jain. Unsupervised contour-representation and estimation using B-splines and a minimum description length criterion. *IEEE Trans. Image Processing*, 9(6):1075–1087, 2000.
- [29] Mario Figueiredo and Anil K. Jain. Unsupervised learning of finite mixture models. *IEEE Trans. Pattern Analysis and Machine Intelligence*, 24(3):381–396, 2002.
- [30] Aravind Ganapathiraju, Jonathan E. Hamaker, and Joseph Picone. Applications of support vector machines to speech recognition. *IEEE Trans. Signal Processing*, 52(8):2348–2355, 2004.
- [31] Paul W. Goaz and Studart C. White. *Oral Radiology—Principles and Interpretation*. The C. V. Mosby Company, St. Louis, 1982.
- [32] S. Gold, A. Rangarajan, C. Lu, S. Pappu, and E. Mjolsness. New algorithms for 2d and 3d point matching: Pose estimation and correspondence. *Pattern Recognition*, 31(8):1019–1031, 1998.
- [33] M. Goldstein, Sweet D. J., and Wood R. E. A specimen positioning device for dental radiographic identification. *Journal of Forensic Science*, 43:185–189, 1998.
- [34] Rafael C. Gonzalez and Paul Wintz. *Digital Image Processing*. Addison-Wesley Publishing Company, Inc., 1977.
- [35] G. Gustafson. *Forensic Odontology*. Staples Press, 1966.
- [36] S. P. Han. A globally convergent method for nonlinear programming. *Journal of Optimization Theory and Applications*, 22:297, 1977.
- [37] Hao Huang and Junghua Wang. Anisotropic diffusion for object segmentation. In *Proc. IEEE International Conference on Systems, Man, and Cybernetics*, volume 3, pages 1563–1567, Nashville, TN, October 2000.
- [38] K.C. Hui and Yadong Li. Feature based 2d shape transformation. In *Proc. IEEE Conference on Information Visualization (IV '97)*, pages 337–342, London, UK, August 1997.

- [39] A. K. Jain, R. Bolle, and Pankanti S., editors. *BIOMETRICS: Personal Identification in Networked Society*. Kluwer Academic Publishers, 1999.
- [40] Anil Jain and Hong Chen. Matching of dental x-ray images for human identification. *Pattern Recognition*, 37(7):1519–1532, 2004.
- [41] Anil Jain and Hong Chen. Registration of dental atlas to radiographs for human identification. In *Proc. of SPIE Conference on Biometric Technology for Human Identification II*, volume 5779, pages 292–298, Orlando, Florida, 2005.
- [42] Eugene Lee. Choosing nodes in parametric curve interpolation. *Computer-Aided Design*, 21:363–370, 1989.
- [43] Mohammad H. Mahoor and Mohamed Abdel-Mottaleb. Classification and numbering of teeth in dental bitewing images. *Pattern Recognition*, 38(4):577–586, 2005.
- [44] T. Matsumoto, H. Matsumoto, K. Yamada, and S. Hoshino. Impact of artificial “gummy” fingers on fingerprint systems. volume 4677, pages 275–289, April 2002.
- [45] J. McGarvey. WinID: Dental identification system, 2005. <http://www.winid.com>.
- [46] J. Murray. *Prevention of oral disease*. Oxford: Oxford University Press, 1986.
- [47] Patrice O’Shaughnessy. More than half of victims IDd. *New York Daily News*, 11 Sep. 2002.
- [48] Pietro Perona and Jitendra Malik. Scale-space and edge detection using anisotropic diffusion. *IEEE Trans. Pattern Analysis and Machine Intelligence*, 12(7):629–639, 1990.
- [49] John W. Peterson. Arc length parameterization of spline curves. <http://www.saccade.com/writing/graphics/>.
- [50] John C. Platt. Probabilistic outputs for support vector machines and comparison to regularized likelihood methods. In Alexander J. Smola, Peter Bartlett, Bernhard Schlkopf, and Dale Schuurmans, editors, *Advances in Large Margin Classifiers*. MIT Press, Cambridge, MA, 1999.
- [51] I. A. Pretty and D. Sweet. A look at forensic dentistry - part 1: The role of teeth in the determination of human identity. *British Dental Journal*, 190(7):359–366, April 2001.
- [52] D. M. Russell, P. P. Maglio, R. Dordick, and C. Neti. Dealing with ghosts: managing the user experience of autonomic computing. *IBM systems Journal*, 42(1):177–188, 2003.

- [53] Marie Sandstrom. Liveness detection in fingerprint recognition systems. Master's thesis, Examensarbete utfört i Informationsteori, vid Linköpings tekniska högskola, 2004.
- [54] James Sethian. *Level Set Methods and Fast Marching Methods*. Cambridge University Press, Cambridge, UK, 2nd edition, 1999.
- [55] H. Silverstein. *Comparison of antemortem and postmortem findings*. In: *Manual of forensic odontology*. Ontario: Manticore, 3rd edition edition, 1995.
- [56] Milan Sonka, Vaclav Hlavac, and Roger Boyle. *Image Processing - Analysis, and Machine Vision*. Brooks/Cole, Thomson Learning, Florence, KY, 2nd edition, 1999.
- [57] M. B. Stegmann and D. D. Gomez. A brief introduction to statistical shape analysis. Technical report, Richard Petersens Plads, Building 321, DK-2800 Kgs. Lyngby, Mar. 2002.
- [58] Ambika Suman. *Knowledge-Based Intelligent Information and Engineering Systems*, volume 2774/2003 of *Lecture Notes in Computer Science*, chapter Human Factors that Affected the Benchmarking of NAFIS: A Case Study, pages 1235–1244. Springer Berlin / Heidelberg, 2003.
- [59] Panarat Thepgumpanat. Thai tsunami forensic centre produces first IDs. *Reuters*, <http://www.alertnet.org/>, 18 Jan. 2005.
- [60] H. Wang, J. Kearney, and K. Atkinson. Arc-length parameterized spline curves for real-time simulation. In *Proc. 5th International Conference on Curves and Surfaces*, pages 387–396, San Malo, France, June 2002.
- [61] J. Weickert. *Anisotropic Diffusion in Image Processing*. B.G. Teubner, 1998.
- [62] T. F. Wu, C. J. Lin, and R. C. Weng. Probability estimates for multi-class classification by pairwise coupling. In S. Thrun, L. Saul, and B. Scholkopf, editors, *Proc. Advances in Neural Information Processing Systems (NIPS)*, volume 16, Cambridge, MA, 2003. MIT Press.
- [63] Chenyang Xu and Jerry L. Prince. Snakes, shapes, and gradient vector flow. *IEEE Trans. Image Processing*, 7(3):359–369, March 1998.
- [64] Yongjian Yu and S.T. Acton. Speckle reducing anisotropic diffusion. *IEEE Trans. Image Processing*, 11(11):1260–1270, 2002.
- [65] Dengsheng Zhang and Guojun Lum. Review of shape representation and description techniques. *Pattern Recognition*, 37(1):1–19, 2004.